Compartmentalized dendritic plasticity in the retrosplenial cortex integrates memories across time

*Megha Sehgal[1,4], Daniel Almeida Filho[1,5], George Kastellakis[2], Sungsoo Kim[3], Jinsu Lee[3], Yang Shen[1], Shan Huang[1], Ayal Lavi[1], Giselle Fernandes[1], Sunaina Soans Martin[1], Irene Davila Mejia[1], Asli Pekcan[1], Melody Shana Wu[1], Won Do Heo[3], *Panayiota Poirazi[2], Joshua T. Trachtenberg[1], *Alcino J. Silva[1]

[1]Departments of Neurobiology, Psychiatry and Psychology & Integrative Center for Learning and Memory, UCLA, Los Angeles, CA.

[2]Institute of Molecular Biology and Biotechnology (IMBB), Foundation for Research and Technology, Hellas (FORTH), Vassilika Vouton, PO Box 1385, GR 70013 Heraklion, Crete, Greece.

[3]Department of Biological Sciences, Korea Advanced Institute of Science and Technology, Daejeon, Republic of Korea.

[4]Department of Psychology, The Ohio State University, Columbus, Ohio

[5]Current Address: SENAI Institute of Innovation in Advanced Health Systems, University Center SENAI CIMATEC, Salvador, Bahia, Brazil

*Corresponding authors. Email: silvaa@mednet.ucla.edu, poirazi@imbb.forth.gr, sehgal.74@osu.edu

SUMMARY

Events occurring close in time are often linked in memory, providing an episodic timeline and a framework for those memories. Recent studies suggest that memories acquired close in time are encoded by overlapping neuronal ensembles, but the role of dendritic plasticity mechanisms in linking memories is unknown. Using activity-dependent labeling and manipulation approaches, longitudinal one- and two-photon imaging of somatic and dendritic compartments, and computational modeling, we show that memory linking is not only dependent on ensemble overlap in the retrosplenial cortex, but also on branch-specific dendritic allocation mechanisms. The same dendritic segments are preferentially activated by two linked memories, and spine clusters added after each of the two linked memories are allocated to the same dendritic segments. Our results demonstrate a causal mechanistic role for dendritic plasticity in memory integration and reveal a novel set of rules that govern how linked and independent memories are allocated to dendritic compartments.

INTRODUCTION

Within the brain, pyramidal neurons use their elaborate dendritic structures to perform computations previously thought impossible for a single cell[1,2]. The molecular and cellular physiology that supports these complex computations within a single cell and how these computations influence ensemble activation, and thus animal behavior, are poorly understood. Active dendritic processes sculpt the flow of information from the synapse to the neuronal soma[3]. *Ex vivo* and *in vitro* studies demonstrate that focal synaptic activity on dendritic segments results in compartmentalized dendritic plasticity, which in turn regulates the integration and propagation of local dendritic signals to the soma, as well as impacts future induction of synaptic plasticity on these dendritic segments[4–8]. Although such localized plasticity within dendritic branches is likely to influence many neural processes, it is unclear whether and how this plasticity modulates memory.

Memory formation is a dynamic process, where single memories are stored, updated, and integrated within the framework of other pre-existing memories to drive adaptive behavior[9–11]. Recent studies in rodents have revealed that the overlap between the neuronal ensembles encoding different memories can link them, such that the recall of one leads to the recall of the other[12–14]. A similar process in humans is believed to mediate inferential reasoning[15,16] and other forms of memory organization. Transient increases in neuronal excitability drive ensemble overlap[12,14], but the neuronal locus as well as specific form of cellular plasticity underlying these changes is unknown.

Memory formation and retrieval are mediated by dendritic and synaptic processes[17,18]. Specifically, learning is mediated by input-specific synaptic plasticity[19–21]. In addition, the currents underlying learning-related changes in intrinsic excitability are dendritic in origin[22]. Yet, our understanding of the localized dendritic plasticity mechanisms that regulate the encoding and integration of memories is limited. Since experience-dependent dendritic plasticity is branch-specific[4–6,8], and potentiation of dendritic spines can affect future plasticity at nearby spines on

69 the same dendritic branch[6,23], we hypothesized that two memories acquired close in time would
70 be allocated to an overlapping population of dendritic branches, and that this mechanism drives
71 linking of distinct memories. To test this hypothesis, we investigated the role of dendritic allocation
72 mechanisms in contextual memory linking within the retrosplenial cortex (RSC), a brain region
73 important for spatial and contextual memory processing[24,25]. We longitudinally tracked and
74 manipulated RSC somas, dendrites, and spines as mice encoded distinct contexts to demonstrate
75 that linked contextual memories are encoded within overlapping dendritic branches within the
76 RSC.

77 **RESULTS**

78 **Overlap in RSC ensembles representing linked memories**

79 The overlap between neuronal ensembles encoding two memories (neuronal co-
80 allocation) is critical for linking these memories[12–14]. However, it is unclear if such neuronal overlap
81 is observed within the RSC neuronal ensembles, a brain region critical for encoding contextual
82 memories. Thus, we first investigated whether RSC neuronal ensembles representing memories
83 of two contexts explored close in time (i.e., linked memories)[12] also display a higher overlap than
84 two ensembles representing memories further apart (i.e., independent memories). We used a
85 customized head-mounted miniature microscope (see Methods for details) to image GCaMP6f-
86 mediated calcium dynamics in RSC neurons (Figures 1a-d and S1, 4599 putative RSC neurons,
87 132.9 ± 11.6 neurons per session,) while mice explored different contexts. We found a greater
88 overlap between the RSC neuronal ensembles activated during encoding of two contexts
89 explored on the same day (5 hours apart), than between the neuronal ensembles activated during
90 encoding of two contexts explored one week apart (Figures 1e and S1). Notably, the increased
91 overlap between neuronal ensembles for memories acquired 5 hours vs. one week apart was not
92 due to differences in ensemble size (Figure S1), or the criteria used for neuronal cross-registration
93 across days (Supplementary Table 1). Importantly, to establish the stability of our longitudinal
94 imaging, mice underwent exposure to the same or different contexts 7 days or 5 hours apart. We

discovered that there is substantial representational drift in the neuronal ensemble representing the same context 7 days apart (Figure S1e). These data are consistent with similar representational drift observed in various brain regions[26–33]. However, the neuronal ensemble representing two contexts seven days apart is significantly more stable when these contexts are the same vs. two distinct contexts (Figure S1f). Therefore, greater overlap between the RSC neuronal ensembles representing two contexts explored on the same day, than between the neuronal ensembles representing two contexts explored one week apart is unlikely to be due to representational drift alone or problems with longitudinal imaging itself. These data indicate that RSC neurons represent temporally proximate contextual memories using overlapping neuronal populations. These results provide strong evidence that the co-allocation of temporally proximate memories to overlapping neuronal ensembles may be a universal mechanism for memory linking.

We reasoned that if, similar to other memory linking paradigms[12,14], transient increases in intrinsic excitability in RSC drive neuronal ensemble overlap of linked memories, then the firing rate of RSC neurons should be similar for contexts explored close in time. We found that RSC neurons maintained a similar frequency of calcium transients for contexts explored within 5 hours compared to contexts explored 7 days apart (Figures 1f and S2). Consistent with the role of intrinsic excitability in memory linking, we found that the highly active cells (especially the top 10% of most active neurons) in a context are more likely to be reactivated in a different context 5h later compared to 7d later (Figure S3). Since RSC neurons encode distinct contexts using a firing rate code[25], it is likely that neuronal firing dynamics within the RSC also impact the ability to decode context identity. Indeed, a Naïve Bayes (NB) classifier performed better at distinguishing sessions recorded a week apart relative to those recorded within the same day (Figures 1g and S2). Finally, we investigated the coactivity patterns of RSC neurons during these context explorations. Theoretical as well as experimental models suggest that groups of neurons with synchronized activity encode task-relevant information in the hippocampus, cortical, and subcortical regions[34–41]. However, the significance of such coactivity patterns during memory formation within the RSC

121 is unclear. Therefore, we calculated the pairwise correlation (PWC) for each pair of RSC neurons
122 within each session (PWC map) and found that these correlations are generally stable across
123 imaging sessions (Figure S5). However, the across-session stability of these PWC maps (co-
124 activity stability) is higher when contexts are explored on the same day compared to one week
125 apart (Figure 1h, i), indicating that RSC neurons maintain patterns of coactivity when contexts are
126 explored within the same day. Such synchronous firing may be key for the linking of contextual
127 memories within the RSC. Together, these data indicate that overlapping RSC ensembles are
128 activated when contextual memories are acquired close in time and that the dynamic activity of
129 these overlapping ensembles may play a critical role in linking different contextual memories.

130 Although overlap in the underlying neuronal ensemble can serve to link these memories
131 (our current findings as well as [12–14]), these memories can still remain distinct[12,13]. To address how
132 temporally proximate memories can be distinguished while being behaviorally linked, we
133 calculated the functional connectivity difference (Euclidean distance (ED)) between correlation
134 maps of neuronal activity from different sessions of the same animals when different and the
135 same context were explored across 7d or 5h intervals (Figure S4a). Since the reactivation of
136 neurons is biased towards the cells that were most active in the previous session, especially the
137 top 10% firing rate (FR) cells, we assessed the importance of these groups of cells for computing
138 the ED between correlation maps. We found that the exclusion of 10% of the most active cells
139 from the correlation maps significantly increased the ED between correlation maps when mice
140 explored distinct contexts 5h apart (Figure S4b, c). Similarly defined high FR cells did not affect
141 the ED between correlation maps when the same or distinct contexts were explored 7d apart or
142 the same context was explored 5h apart. The outsized contribution of high FR cells to
143 representational similarity during exploration of two distinct contexts (vs the same context) 5h
144 apart is consistent with their higher probability of reactivation (Figure S3). Overall, these data
145 indicate that high FR cells within the RSC drive overlap as well as representational similarity at
146 an ensemble level between distinct memories that are linked. On the contrary, representation of

147 the same context is driven more equitably by high and low FR cells. Therefore, memory linking
148 may be driven by highly active cells, while less active cells encode different contextual features
149 that are relevant to sustain the independence between contextual experiences[40].

150 **Overlap in RSC neuronal ensembles links memories close in time**

151 To investigate the causal role of RSC neuronal co-allocation in linking contextual
152 memories, we used the TetTag system[42] to tag and manipulate the RSC neuronal ensembles
153 activated during context exposures (Figure 2a, b). The TetTag system can capture neuronal
154 ensembles in an activity-dependent manner, such that neurons with high firing rates during the
155 behavioral epochs are selectively labeled[43]. Following a 10-minute context exposure, we found
156 that 4.7 ± 0.42% of RSC neurons were labeled with ChR2-mCherry after 24 hours. In comparison,
157 8.5 ± 0.53% of RSC neurons were cFos-immunoreactive 90 minutes after a 10-minute context
158 exposure. We confirmed that optogenetic reactivation of the RSC ensemble underlying a single
159 contextual fear memory (~ 6.05 ± 0.53% of RSC neurons) induces fear expression in an otherwise
160 neutral and novel context (Figures 2c and S6 a-c)[24]. Notably, fear expression following
161 optogenetic reactivation within the RSC is distinct from similar results within the hippocampus [44]
162 in that fear expression was sustained throughout the post-stimulation period and not just the Light-
163 On epochs. These results are consistent with previously published findings[24] and from this point
164 onwards, freezing data during optogenetic reactivation are presented as a comparison between
165 the baseline and post-stimulation period. Overall, our data confirm the critical role of RSC and
166 associated brain circuits in processing contextual information[24,45–47].

167 When two contextual memories are acquired close in time, and one is paired with a fearful
168 stimulus, the mice also consider the second neutral but 'linked' context as fearful (i.e., the two
169 memories are linked)[12]. We asked whether the reactivation of RSC neurons engaged during
170 exploration of the 'linked' context after contextual memory linking was sufficient to elicit freezing
171 in mice (Figure 2d). Indeed, optogenetic reactivation of the 'linked' context's neuronal ensemble

172 in RSC alone was sufficient to trigger freezing in mice exploring a novel context (Figures 2d and
173 S7). We confirmed that such fear expression did not result from the labeling of RSC neurons
174 outside of the tagging window (e.g. during exposure to Context B) as doxycycline administration
175 was sufficient to prevent tagging of additional neurons following exposure to another context, as
176 well as following the injection of pentylenetetrazole (PTZ; Figure S7a). Additionally, the
177 differences in optogenetic reactivation of fear between the TetTag mice and the control group did
178 not stem from differences in contextual learning or linking of contextual memories. We tested the
179 same mice in three different contexts on three consecutive days: the 'linked' context, another
180 novel context, and the 'shock' context to assess their levels of memory linking, memory
181 generalization, and conditioned responses, respectively. Both groups of mice displayed high
182 levels of freezing in 'linked' (Context A) as well as 'shock' (Context B) contexts in comparison to
183 freezing in the novel context (Figure S7). Thus, both groups of mice learned the context-shock
184 association and linked the fearful context to the previously explored context ('linked' context), but
185 only mice where the 'linked' context ensemble was reactivated using the TetTag system displayed
186 fear in a novel context. First, these data indicate that reactivating the memory of a 'linked', but
187 otherwise neutral context, was sufficient to elicit a conditioned response, a result that supports
188 our hypothesis that the recall of one linked memory results in the recall of the other. Second,
189 these findings also demonstrate that manipulation of neuronal ensembles just within the RSC can
190 drive contextual memory linking.

191 While two contexts explored within a day are linked, contexts explored 2 or 7 days apart
192 are not allocated to overlapping neuronal ensembles, and therefore are not linked[12,48]. We asked
193 if we could link two distant contextual memories (acquired 2 days apart) by artificially biasing the
194 involvement of a specific RSC neuronal ensemble in the encoding of both memories. With the
195 TetTag system[42], we tagged the RSC neuronal ensemble activated during a context exploration
196 (Context A) and reactivated this ensemble the next day, one day before exposure to another
197 context (Context B, Figure 2e). We reasoned that this would optogenetically reactivate the first

198 memory, maintain the increase in neuronal excitability, and therefore force the recruitment of this
199 same ensemble[49] during the exploration of another context a day later. We allowed 24 hours for
200 expression and then reactivated the RSC ensemble to allow sufficient expression of
201 Channelrhodopsin post-tagging[43]. While two contexts explored 2 days apart are normally not
202 linked, this optogenetic reactivation of the first contextual memory was sufficient to bridge this 2-
203 day gap and drive the linking of two otherwise independent contextual memories (Figure 2e). We
204 further confirmed the role of neuronal ensemble overlap in the RSC using a chemogenetic
205 (Lentivirus DREADD[12]) system. We biased neuronal co-allocation of two distinct contextual
206 memories by enhancing the neuronal excitability in a sparse population of RSC neurons before
207 each context exploration (2 days apart, Figure S9). Like the optogenetic manipulation, artificially
208 biasing co-allocation of two distant contextual memories to overlapping RSC ensembles using
209 chemogenetics drives the linking of the two memories, such that the mice showed comparable
210 freezing in both contexts (Context A and B). Additionally, we demonstrate that optogenetically
211 activating a small but random population of RSC neurons between two context exposures (similar
212 to Figure 2d) was not sufficient to link two independent contextual memories (Figure S8).
213 Together, these data demonstrate that neuronal ensemble overlap in RSC is critical to link the
214 memories of two distinct contexts.

215 **Overlap in dendritic ensembles encoding linked memories**

216 Ours and previous results demonstrate that the allocation of contextual memories to
217 overlapping neuronal ensembles is critical for linking contextual memories[12,48]. However, the
218 intracellular processes that mediate neuronal overlap are poorly understood. Specifically, whether
219 dendritic plasticity mechanisms contribute to neuronal overlap is unclear. Within the overlapping
220 ensembles, linked memories are thought to be encoded by distinct synaptic changes
221 (heterosynaptic) that allow the memories to maintain their distinct identities[50]. There are at least
222 three dendritic hypotheses that could account for contextual memory linking. First, linked
223 memories may be allocated to different dendritic branches within the encoding neurons (dis-

224 allocation). Second, it is possible that linked memories are randomly allocated to the dendritic
225 branches within the encoding neurons. Third, since experience-dependent dendritic plasticity is
226 highly localized and can affect future plasticity at nearby spines on the same dendritic segment
227 under certain conditions[6,23], it is also conceivable that, following the first context exposure,
228 localized changes in dendritic plasticity temporarily bias the activation of the same dendritic
229 segments during a subsequent context exposure[51]. In the latter scenario, distinct synaptic
230 changes on the same dendritic branches could drive the co-activation, and therefore the linking
231 of the two memories. We propose that localized dendritic plasticity is a key mechanism driving
232 neuronal ensemble overlap, since this plasticity could affect the propagation of synaptic inputs on
233 specific dendritic segments to the soma. To distinguish between these different hypotheses, we
234 used two-photon microscopy to investigate the functional and structural dynamics of the apical
235 dendrites of layer V RSC neurons (Figures 3-5). Specifically, we targeted the apical dendrites of
236 layer V RSC neurons because we have previously demonstrated that dendritic plasticity in the
237 form of spine turnover and clustered spine addition on dendritic hotspots within these
238 compartments facilitates single contextual memory formation[19]. We reasoned that the important
239 role of these dendritic compartments in single contextual memory formation makes them an
240 excellent candidate for co-allocation of dendritic plasticity following memory linking.

241 First, we performed longitudinal calcium imaging of the somas as well as apical dendrites
242 of layer V RSC neurons (see Methods for details, Video 1, Figure 3a-b), while mice explored
243 distinct contexts in a head-fixed setting (Figure S10). Consistent with our results with RSC
244 neuronal activation in freely moving mice (Figure 1), head-fixed mice also represent two contexts
245 experienced close in time by recruiting overlapping RSC ensembles (Figure S11). These data
246 reveal the similarities in the neuronal encoding of temporally-proximate memories in head-fixed
247 and freely moving mice indicating the generalizability of our findings across two imaging
248 modalities. We next assessed the degree of overlap among RSC dendritic branches when
249 contexts are explored close in time. We imaged apical dendrites (in layer 1 of the RSC, ~ 30 μm

250 from the pia mater) following GCaMP expression of layer V RSC neurons (see Methods for
251 additional details). We found that the same dendritic ROIs were preferentially reactivated as mice
252 explored two distinct contexts within the same day, but not a week apart (Figures 3e-g, j and
253 S12a). Consistent with the role of NMDA receptor activation in memory linking[12] as well as
254 clustered spine formation in the RSC[19], reactivation of dendritic segments required NMDA
255 receptor activation during the first context exposure (Figure S13).

256 The extent and prevalence of independent dendritic and somatic events during calcium
257 imaging, the causality or direction of their interdependence, and the factors that affect these are
258 poorly established[52–55]. For our experiments, we sought to minimize the effect of backpropagating
259 action potentials and global dendritic transients by imaging RSC apical tuft dendrites, as apical
260 tuft branches display a degree of independence from one another and somatic calcium events[55].
261 To account for highly correlated calcium transients across ROIs driving our observed effects, we
262 performed a hierarchical clustering analysis to group segmented ROIs into single dendritic units
263 when their calcium dynamics are highly correlated (Figure 3e, see Methods for analysis details).
264 We found similar proportions of clustered ROIs among reactivated and overall segmented ROI
265 populations (Reactivated ROIs: 0.85 ± 0.02; overall ROI population: 0.86 ± 0.02; p = 0.3).
266 Clustering segmented ROIs in this way (to account for global dendritic transients or
267 backpropagating action potentials contaminating our results) did not change our observed effects
268 (Figures 3f-g and S12a). The clustered ROIs within reactivated segments maintained high within-
269 cluster correlated activity across sessions, demonstrating the robustness of our clustering
270 algorithm as well as the longitudinal coupling of these ROIs (Figure S12c). It is still possible that
271 there is a one-to-one correspondence between our reactivated neurons and dendritic segments
272 (all clustered ROIs), but we believe this is unlikely given the low levels of clustering (mean cutoff
273 value = 0.13 ± 0.01, 1.15 ± 0.03 ROIs per cluster, Figure S12b) and the large difference between
274 neuronal and dendritic overlap in our head-fixed experiments (Figure 3g and S11). It is possible
275 but unlikely that the differences in neuronal and dendritic overlap are due to a lower signal-to-

276 noise ratio (SNR) during dendritic imaging. Neuronal overlap using one-photon calcium imaging
277 (Figure 1) where SNR is usually markedly lower than two-photon imaging was more similar to
278 neuronal overlap in two-photon imaging conditions (Figure S11) and different than the degree of
279 dendritic overlap. Importantly, these results did not rely on using any particular clustering criteria
280 as clustering cutoffs that consistently resulted in clustered ROIs within shuffled distributions with
281 randomized activity also yielded low cluster sizes in the experimental dataset (Clustering cutoff =
282 0.3, 1.39 ± .06 ROIs per cluster, see Methods) as well as similar overlap results (p <0.001).

283 Next, we analyzed calcium transient frequencies within the reactivated dendrites during
284 two contexts explored 5 hours apart and found that these were highly correlated (Figure 3h). We
285 did not observe a significant correlation between calcium transient frequencies in reactivated
286 dendrites when contexts were explored 7 days apart (Figure 3h). To confirm that this analysis
287 was not biased by differences in the number of reactivated dendrites for two context exposures 7
288 days or 5 hours apart, we repeatedly (500X) subsampled 30 reactivated ROIs (see Methods) from
289 each condition to generate a probability distribution of correlation coefficients (Figure 3i). This
290 subsampling analysis confirmed that calcium transient frequencies are more correlated when
291 contexts are explored close in time. These data indicate that the synaptic drive and the local
292 excitability mechanisms driving dendritic activity are maintained during the encoding of linked
293 memories.

294 Finally, we asked if dendritic overlap was different when animals explored the same or
295 different contexts at 7 days or 5 hours apart (Figure 3j). Similar to our data demonstrating neuronal
296 overlap (Figure S1), we found that dendritic ROIs were more likely to be reactivated closer in time
297 (5h vs 7d) whether animals experienced the same or different contexts (Figure 3j). In addition to
298 this effect of time, we confirmed that dendritic representations are more similar for the same
299 context vs different contexts irrespective of time. Our data here (Figure 3) are consistent with the
300 hypothesis that local dendritic mechanisms govern the allocation of two contextual memories

301 encoded close in time to the same dendritic segments[51]. Next, we used structural imaging of RSC
302 apical dendrites to confirm and extend these findings.

303 **Linked memories bias spine remodeling to overlapping dendritic segments**

304 Given that overlapping dendritic segments are activated when encoding contexts that are
305 experienced close in time, we next investigated whether learning-related spine dynamics were
306 also evident on the same dendritic segments when contextual memories are acquired close in
307 time. Within the RSC, formation of a contextual memory is accompanied by structural plasticity at
308 apical dendritic branches of layer V RSC neurons, such that behavioral performance is positively
309 correlated with clustered spine addition on small stretches (~5μm) of a dendritic segment[19]. These
310 data are consistent with the clustered plasticity hypothesis, and indicated that experience-
311 dependent spine remodeling is spatially restricted in a branch-specific manner[5,6,19]. We used *in*
312 *vivo* two-photon microscopy to image spines on the RSC apical dendrites of Thy1-YFP-H mice
313 following multiple context exposures (Figure 4a-d). As structural imaging involved mice being
314 imaged under anesthesia, we confirmed that mice were still able to link the memories for distinct
315 contexts under these conditions (i.e., ~40mins of anesthesia following context exposure: ~ length
316 of the spine imaging session, Figure S14). We quantified the spines added or lost following each
317 context exposure and found that relative to spine dynamics during a baseline period, novel context
318 exposure does not change overall spine addition, spine loss, or spine turnover (Figure S15a, b).
319 However, following context exposure, new spines were added in clusters (i.e., within 5μm of each
320 other); and a shuffling analysis showed that the number of these clustered spines was significantly
321 above chance levels (p = 0.009; Figure S15c). In contrast, clustered spine addition in the control
322 group - that went through all the same imaging procedures, but that was never exposed to a novel
323 context - was at chance levels (p = 0.14; Figure S15c). Finally, spine formation or clustering was
324 not correlated with pre-learning turnover (HC, ρ = 0.1 and 0.09 respectively; Context exposure
325 group, ρ = 0.07 and 0.02; all p values = ns). We found that new spine formation following learning

326 was correlated with spine density in control conditions (HC, $\rho = 0.43$, $p = 0.007$) but not following
327 a context exposure ($\rho = 0.23$, ns). Hence, consistent with previous findings[19], novel context
328 exploration results in clustered plasticity in RSC dendrites.

329 Since our results showed reactivation of the same dendrites during context exposures
330 close in time, we next investigated the possibility that spines added following these context
331 exposures also tend to be added to the same dendritic segments (Figure 4e-h). We found a
332 positive correlation between the number of spines added to the same dendritic segments following
333 two context exposures experienced 5 hours apart (Figure 4e). In contrast, the number of spines
334 added to the same dendritic segments following context exposures one week apart were not
335 correlated (Figure 4e). Spine addition was also not correlated in the control group that
336 experienced the same imaging procedures without context exposures, at either the 5 hours or 7
337 days time intervals (Figure 4g). Next, we shuffled the number of new spines added to a dendritic
338 segment following imaging sessions 5 hours or 7 days apart to generate a shuffled distribution.
339 This procedure was repeated (10,000X) to generate a probability distribution of correlation
340 coefficient values from this shuffled data. Our observed correlation coefficient between the
341 number of spines added to a dendritic segment following two context exposures 5 hours apart (ρ
342 $= 0.37$) was unlikely to be observed in this shuffled distribution ($p = 0.006$). In contrast, the number
343 of spines added to a dendritic segment when two distinct contexts were explored 7 days as well
344 as under home cage conditions are not correlated (also see Figure 4e, g) and not statistically
345 different from correlation coefficients observed following the shuffling procedure (AB, 7d apart, p
346 $= 0.3$; HC, 5h apart, $p = 0.2$; HC, 7d apart, $p = 0.1$).

347 We also calculated the Mutual Information (see Methods) contained in the number of
348 spines added following two context explorations 5 hours apart and found that spine addition
349 following the encoding of one context is predictive of the number of spines added following the
350 encoding of a linked context (Figure 4f). This was not true for other imaging conditions (i.e., when

351 contexts are explored 7 days apart; Figure 4f) or in the home cage controls (Figure 4h).
352 Furthermore, the number of spines lost was not correlated whether the imaging sessions were
353 conducted 7 days or 5 hours apart in both the control and experimental groups (Figure S16).
354 Finally, we compared the distribution of newly added spines across groups. The correlation
355 coefficient generated by distributions of newly added spines following two context exposures 5
356 hours apart was statistically different than the correlation values generated in other conditions
357 (Fisher transformation; Experimental 5h vs HC 5h, $Z = 1.8$; $p = 0.03$; Experimental 5h vs
358 Experimental 7d, $Z = 1.67$; $p = 0.047$; HC 7d vs HC 5h, $Z = -0.42$; $p = 0.33$). To control for the
359 differences in the number of dendritic branches imaged under different conditions, we
360 subsampled 40 dendritic branches from each condition (10,000X) to obtain a distribution of
361 Spearman Correlations and Mutual Information for each condition. We found that mean
362 Spearman Correlation, as well as Mutual Information values, are higher when mice explore two
363 novel contexts 5h apart compared to all the other conditions (Figure 5e, f; $p < 0.001$). These data
364 indicate that spine addition is biased to the same RSC dendritic segments when contextual
365 memories are linked (acquired 5 hours apart), but not when these memories are independent
366 (acquired 7 days apart).

367 Next, we analyzed spine dynamics looking for co-allocation of clustered spines (i.e.,
368 whether dendritic segments that gained clustered spines during a context exposure were also the
369 ones that gained clustered spines during a previous context exposure). We found that the
370 probability of the same dendritic segments gaining spine clusters following exposures to two
371 contexts was at chance levels when these contexts were explored 7 days apart ($p = 0.4$, Figure
372 5a). Importantly, spine clusters were more likely to be added to the same dendritic segments
373 when contexts were explored within the same day (5 hours apart; $p = 0.03$, Figure 5a). In contrast,
374 the addition of clustered spines in the control group was random: the probability of the same
375 dendritic segments gaining spine clusters during two imaging sessions was at chance levels
376 whether the imaging sessions were 5 hours or 7 days apart ($p = 0.28$ and 0.5 respectively; Figure

377 5c). Using a similar analysis as for Figures 5e and f, we found that the probability that clustered
378 spines were added to a dendritic branch already containing clustered spines was higher for an
379 imaging session when two contexts were explored 5h apart in comparison to an imaging session
380 at the same time interval under HC condition (Figure 5g, $p < 0.0001$). Thus, synaptic plasticity in
381 the form of clustered spine addition following the encoding of linked memories is biased to
382 overlapping dendritic segments.

383 Finally, we asked whether new spines added following exposure to two linked contexts
384 were added close to one another, or if they cluster with each other. While 43.3% of newly formed
385 spines following the last context exposure were clustered with the spines added following the
386 context exposure 5 hours before (average distance between nearest neighbors = 7.7 ± 1.0 μm),
387 only 19.6% of the new spines were clustered with new spines from the context exposure a week
388 before (average distance between nearest neighbors = 17 ± 2.3 μm; Figure 5b). In control mice
389 that did not receive context exposures, newly formed spines following the last imaging session
390 clustered with new spines from the previous imaging session at similar rates whether the last
391 session imaging was 5h or 7d before (5h: 32.4%, average distance between nearest neighbors =
392 10.7 ± 1 μm; 7d: 32.0%, average distance between nearest neighbors = 10.7 ± 1.3 μm, Figure
393 5d). Importantly, the cumulative frequency distribution as well as the average distance between
394 nearest neighboring spines are statistically different between the experimental and HC group
395 even when the imaging sessions were performed 5 hours apart (KS test, $p < 0.005$ and Mann
396 Whitney, $p < 0.05$ respectively). Thus, new spines and spine clusters are added to overlapping
397 dendritic segments following the formation of linked memories, and these newly formed spines
398 cluster with each other. It is likely that such synaptic clustering can facilitate non-linear summation
399 of dendritic inputs[56] , which would result in more robust propagation of inputs to the soma resulting
400 in increased somatic firing[1,57–60]. Indeed, clustered spines are more effective at influencing
401 neuronal spiking and, thus, the tuning properties of a neuron[56,61,62]. We demonstrate that following

402 the encoding of two linked memories, spine clusters are added to the same dendritic branches.
403 The addition of new spines in clusters to these dendritic branches could facilitate future ensemble
404 activation. Together, the structural, as well as functional imaging data from RSC dendrites,
405 indicate that the same dendritic branches are recruited to encode contextual memories formed
406 close in time (i.e., linked memories).

407 **Optogenetic reactivation of a tagged dendritic ensemble links two independent**
408 **memories**

409 Next, we tested whether such dendritic co-allocation is sufficient for linking contextual
410 memories. To investigate the behavioral significance of RSC dendritic co-allocation, we modified
411 an optogenetic tool for tagging and manipulating previously activated dendritic segments: We
412 leveraged the activity-dependent labeling of the cFos-tTA system, and combined it with the
413 dendritic targeting element (DTE) of Arc mRNA, which is selectively targeted and locally
414 translated in activated dendritic segments following learning (Figure 6a,b)[63,64]. This novel
415 approach allowed us to manipulate dendritic activity by expressing a light-sensitive ion channel
416 (Channelrhodopsin) in recently activated dendritic segments[18,65,66] of RSC neurons that underlie
417 the contextual memory trace. Since our tagging strategy was designed to mimic the well-
418 documented activity-dependent increase of Arc mRNA expression in recently activated
419 dendrites[67–70], we first verified whether Arc mRNA is co-localized to the tagged dendritic
420 segments. Following DTE-based labeling, mRNA encoding the fluorescent tag 5h after exposure
421 to a novel context is more likely to colocalize near Arc mRNA in dendritic compartments (Figure
422 S17a) indicating that our strategy can target activated dendrites. Next, we confirmed that dendritic
423 segments labeled using a DTE-based method were also more likely to be reactivated upon re-
424 exposure to the original tagging stimuli, i.e. exposure to the original context. Several lines of
425 evidence have established that synaptic activity results in rapid phosphorylation (2-7 mins) of
426 Cofilin protein in the synapse [71,72]. We found that PSD-95 puncta on dendritic segments labeled
427 using the DTE-based tagging method displayed an increase in phosphorylated form of Cofilin

428 protein in comparison to PSD-95 puncta that were not present on labeled dendrites (Figure S17b).
429 These data are consistent with previous reports[18,65,66] and support that the DTE-based labeling
430 allowed us to tag dendrites in an activity-dependent manner.

431 Next, we assessed whether activation of dendritic segments tagged in this manner results
432 in somatic activation. While optogenetic stimulation of RSC neurons from TTA-ChR2 mice
433 resulted in somatic responses in the form of action potentials, the same stimulation only elicits
434 transient small amplitude depolarizations in the TTA-ChR2-DTE mice (Figure 6c-e). Moreover,
435 we also tagged and reactivated RSC dendrites activated during contextual memory formation in
436 a novel context (Figure S6d, e). Unlike our somatic manipulations, tagging and activation of
437 dendritic compartments alone were not sufficient to elicit fear expression in a novel context.
438 Together these data indicate that Channelrhodopsin-mediated dendritic activation using the TTA-
439 ChR2-DTE system has limited effects on the depolarization of somas and therefore fails to elicit
440 an acute behavioral response. Hence, combining the cFos-tTA system with DTE allowed us to
441 study the role of previously active dendrites (while limiting somatic involvement) in memory
442 linking.

443 Next, we asked whether artificially biasing dendritic allocation, similar to our neuronal
444 manipulations (Figures 2e and S9), is sufficient to link two contextual memories, which would
445 otherwise be independent. We tagged active dendrites during the first context exploration
446 (Context A) and reactivated these dendrites the next day while the mice were in their home cage.
447 One day after this reactivation (i.e., two days after the exploration of Context A), we exposed the
448 mice to another novel context (Context B). As we have shown above, two contexts explored 2
449 days apart are normally not linked (Figure 2e and S9)[12]. However, similar to the reactivation of
450 Context A neurons (Figure 2e), the reactivation of dendrites first activated in Context A is sufficient
451 to link Context A and Context B (the shock context): freezing in the 'linked context' (Context A)
452 was higher than freezing in a 'novel' context and similar to freezing in the shock context (Context
453 B). Hence, the reactivation of dendrites tagged during the exploration of one context is sufficient

454 to link that context to another independent context (Figure 6f). These results demonstrate a causal
455 role for RSC dendritic mechanisms in the allocation as well as linking of contextual memories and
456 reveal a novel set of rules that govern how linked, and independent memories are allocated to
457 various dendritic compartments.

458 **Biophysical dendritic modeling: dendritic plasticity mechanisms are necessary for**
459 **neuronal overlap and co-recall of memories**

460 Our data thus far suggests that synergism between somatic and dendritic mechanisms
461 sculpts memory allocation within the RSC to regulate the linking of memories. To explore whether
462 linking of memories that are acquired close in time is even possible in the absence of dendritic
463 mechanisms, we adapted a network model of memory allocation[19,51] and used it to investigate
464 how two independent memories can first become linked in a brain region. The model incorporates
465 somatic as well as dendritic allocation mechanisms that rely on intrinsic excitability modulation
466 (see Methods, Figure 7a, b), as suggested by prior studies[4,8,73]. As with our experimental data,
467 the network model shows that neuronal (Figure 7c), as well as dendritic overlap (Figure 7d), is
468 higher when two memories are acquired close in time (5 hours vs 2 or 7 days apart). Moreover,
469 high dendritic overlap is also characterized by increased synapse clustering (Figure 7e), in line
470 with our spine imaging experiments. Importantly, our model predicts that when linked memories
471 are recalled (i.e., memories acquired 5 hours apart), they maintain higher neuronal overlap
472 indicating co-recall and thus stable linking of these memories (Figure 7f). To dissect the relative
473 contributions of somatic vs. dendritic mechanisms in memory linking, we asked how these
474 neuronal and dendritic overlap measures change in the absence of dendritic allocation and
475 plasticity mechanisms (see Methods). Remarkably, both neuronal and dendritic overlap during
476 encoding is reduced when the model lacks dendritic mechanisms (Figure 7c-e, orange). More
477 importantly, the lack of dendritic mechanisms in the model abolished co-recall or linking of
478 memories, suggesting that dendritic mechanisms are crucial for stable memory linking (Figure 7f,

479 orange: neuronal overlap during recall is the same whether memories are acquired 5 hours, 2
480 days or 7 days apart).

481 To assess the importance of converging synaptic input onto the same dendritic
482 compartments for memory linking, we modeled synaptic inputs representing the two contexts (A
483 and B) on separate (exclusively non-overlapping) dendritic branches. The model predicts
484 impaired neuronal overlap (during encoding and recall) when two memories encoded 5 hours
485 apart recruit non-overlapping dendritic populations, suggesting that to effectively link separate
486 inputs within a neuron, these inputs need to overlap onto the same dendritic compartments
487 (Figure 7g). Together, our data indicate that dendritic allocation mechanisms may be necessary
488 (Figure 7) and sufficient (Figure 6) for linking memories acquired close in time.

489 **DISCUSSION**

490 Our findings demonstrate that localized dendritic mechanisms play a causal role in
491 mediating neuronal ensemble overlap and thus, linking of contextual memories. We demonstrate
492 that in addition to neuronal ensemble overlap, local dendritic rules further sculpt the allocation of
493 memories to dendritic segments, such that temporally proximate (i.e., linked) memories are likely
494 to be allocated to the same dendritic segments, while temporally distant (i.e., independent)
495 memories are not. We leveraged activity-dependent targeting of dendritic segments to
496 demonstrate that biasing memory allocation to the same dendritic segments is sufficient to link
497 these memories. Accordingly, computational modeling supports the key role of dendritic
498 mechanisms in memory linking. Altogether, the findings presented here demonstrate that
499 localized dendritic mechanisms are critical for linking memories. Furthermore, since RSC is one
500 of the first brain regions to demonstrate Alzheimer's-related dysfunction[74,75], and memory linking
501 is affected early during aging[12], our findings have clinical implications for understanding age-
502 related cognitive decline and associated pathological conditions.

503 **RSC neuronal ensemble activation during encoding of linked memories**

504 Within the RSC, neuronal ensemble activation encodes contextual and spatial
505 information[24,25,55,76,77]. We asked whether RSC representations of two contextual memories
506 acquired close in time (5h apart), such that they are behaviorally linked, are more similar than
507 those of two memories acquired a week apart (independent memories). We discovered that linked
508 memories activated an overlapping neuronal ensemble in the RSC (Figure 1e). Furthermore, the
509 inferred activity and co-activity dynamics of these RSC ensembles were also similar for linked,
510 but not independent memories (Figure 1g-i). Accordingly, a classifier showed lower accuracy for
511 decoding distinct contexts seen closer in time (i.e., linked contexts) compared to contexts seen
512 further apart in time (i.e., independent contexts). Our data are consistent with the important role
513 of RSC neural dynamics in contextual memory encoding and demonstrate that the neuronal
514 representations of two linked contexts encoded close in time are more similar than the neuronal
515 representations of independent contexts. In addition, these data indicate that linked memories are
516 encoded by overlapping neuronal ensembles in multiple brain regions, including hippocampal
517 CA1[12,48] and RSC (Figure 1).

518 **RSC neuronal mechanisms underlie the linking of contextual memories**

519 Several studies have demonstrated that plasticity within the RSC is necessary for
520 contextual fear expression[76,78], and RSC-associated brain circuits have been described that
521 underlie the encoding of single contextual fear memories[45–47]. Consistent with previous findings[24],
522 we demonstrate that optogenetic reactivation of RSC ensembles (as captured by the TetTag
523 system) is sufficient for contextual fear expression (Figure 2c). While similar experiments in the
524 hippocampus lead to fear expression specifically during the stimulation (Light-On epochs), we
525 found that RSC ensemble reactivation results in a sustained increase in freezing during the post-
526 stimulation period. These differences could be a result of experimental conditions (context size
527 and similarity etc.)[79] which can affect the nature of memory expression upon optogenetic
528 stimulation. It is just as likely that RSC ensemble reactivation which by itself is sufficient to elicit

529 fear expression in the absence of hippocampal activity elicits a distinct pattern of activation in
530 downstream target regions resulting in a sustained fear expression[24].

531 Importantly, we show that optogenetic reactivation of the RSC ensemble underlying a
532 linked neutral memory is sufficient to induce fear expression associated with a second fearful
533 memory (Figure 2d). Thus, the activation of a neural ensemble underlying one of the linked
534 memories is sufficient for the co-recall of another linked memory. Moreover, these effects on
535 contextually linked memories can be mediated by RSC ensembles alone. These data
536 demonstrate the critical role of the RSC in mediating the expression of linked contextual
537 memories.

538 Linking of contextual memories is robust when these memories are acquired within the
539 same day, but with intervals of two or more days, these memories are behaviorally independent
540 of one another (Figures 2e and S9)[48]. Here, we demonstrate that optogenetic or chemogenetic
541 manipulation of RSC ensemble overlap alone is sufficient to link two otherwise independent
542 memories (Figure 2e and S9). These data are consistent with amygdala-dependent linking of
543 aversive memories, where the retrieval of a previously encoded memory resets the time window
544 for linking a new memory[14]. Similarly, persistent reactivation of neural ensembles underlying two
545 aversive amygdala-dependent memories by co-recall links them behaviorally[13]. It is likely that
546 optogenetic activation of RSC ensembles underlying the first memory in the home cage (Figure
547 2c) results in recall of this memory, which is likely to re-engage the same plasticity mechanisms
548 that were important for encoding the original contextual memory, thereby extending the window
549 for memory linking. Using a similar but mechanistically different strategy, we chemogenetically
550 increased the excitability of the same sparse RSC ensemble prior to two contextual memory
551 episodes (Figure S9). Similar strategies have been used to bias memory allocation to the
552 underlying ensemble[12,14,49]. Forcing neuronal overlap within RSC ensembles in this way was
553 sufficient to link two independent contextual memories (Figure S9). In addition, we show that
554 transiently manipulating the activity of RSC neurons before a single context exposure does not

555 affect memory linking (Figure S9). Finally, we found that activating a sparse but randomly labeled
556 neuronal ensemble in a similar manner did not result in memory linking (Figure S8) demonstrating
557 that effects are specific to the ensembles representing a novel context. Together, our data
558 demonstrate that neuronal overlap within the RSC ensemble alone is sufficient to link distinct
559 contextual memories (Figures 2 and S9), and that this is a key mechanism for linking contextual
560 memories under various behavioral conditions.

561 We find that neuronal overlap in the RSC, similar to overlap in the CA1 ensembles, can
562 affect the linking of contextual memories. Activity within the hippocampus as well as the RSC is
563 important for contextual as well as spatial tasks[24,25,44,78,80–82]. For example, activity and plasticity
564 within CA1 as well as RSC ensembles during contextual fear memory formation affects retrieval
565 of contextual fear memories[78,83]. Similarly, the reactivation of RSC[24], CA1[17], or dentate gyrus[44]
566 ensembles tagged during context fear memory formation is sufficient to induce fear expression in
567 a novel neutral context. While the precise role and the interaction of hippocampal and retrosplenial
568 sub-regions in contextual memory processing is not well understood, optogenetically reactivation
569 of tagged RSC ensembles can result in fear expression even when hippocampal activity is
570 inhibited[24]. These data indicate that both hippocampus and RSC support contextual memory
571 formation and RSC ensembles can support fear expression independently. Subiculum to RSC
572 projections arising from vGlut1 and vGlut2-expressing pyramidal neurons play a differential role
573 in recent and remote contextual memory formation[46]. These data and RSC's well-established
574 projections to the important nodes in the fear circuit[84] support the hypothesis that RSC may be
575 downstream of the hippocampus in the contextual fear memory circuit and plays an important role
576 in information processing within this circuit. RSC activity is especially critical in more complicated
577 associative memory paradigms[85,86], tasks where discrimination between similar stimuli is
578 required[87] as well as generalization[88] and remote memory recall[46]. The precise contribution of
579 hippocampal and RSC processing to contextual memory formation, as well as the linking of

580 contextual memories, is unknown but important to develop a clearer understanding of these
581 phenomena and will be an exciting new area of research.

582 **Localized dendritic plasticity mechanisms mediate the encoding of temporally**
583 **proximate memories**

584 Experience-dependent localized dendritic plasticity has been assessed in *ex vivo*
585 settings[4,6–8,23,89]. However, it was unclear whether new learning induces compartmentalized
586 dendritic plasticity. Moreover, the function of such localized dendritic plasticity in memory
587 processes is unknown. We show that linked contextual memories result in the activation of
588 overlapping dendritic branches within RSC apical dendrites (Figure 3). The inferred firing rate, a
589 measure in part dependent on the excitability of dendritic segments, was more correlated between
590 segments reactivated following the encoding of linked, but not independent memories. In addition,
591 we demonstrated that following the formation of linked memories, structural synaptic plasticity
592 (addition of single spines as well as spine clusters) is also biased to overlapping dendritic
593 segments (Figures 4 and 5). Although our dendritic calcium imaging results (Figure 3) did not
594 conclusively rule out a neuron-wide pan-dendritic reactivation, we believe this possibility is
595 unlikely given low-level dendritic overlap and the wealth of evidence that learning-related plasticity
596 is input-specific and only observable on some but not all dendritic/synaptic loci within a
597 neuron[21,90–92]. Our finding that linked contextual memories are co-allocated to overlapping
598 dendritic branches is consistent with the hypothesis that experience-dependent localized dendritic
599 plasticity is a metaplasticity mechanism that influences future plasticity on these dendritic
600 branches. Indeed, our computational model predicts that a localized increase in dendritic
601 excitability, and the associated facilitation of structural plasticity on these dendritic segments, are
602 necessary for neuronal overlap during recall (i.e., a measure of co-recall in our biophysical model,
603 Figure 7).

604 We targeted apical dendrites from layer V RSC neurons as we have previously shown that
605 these dendritic compartments undergo clustered plasticity (i.e., spine addition) following

606 contextual memory formation. Such clustered spine addition is correlated with improved learning,
607 and spines added in clusters are more stable[19]. Manipulations that increase clustered spine
608 addition on these dendritic branches also facilitate contextual memory performance[19]. Apical
609 dendrites from layer V RSC neurons receive projections from various thalamic nuclei[45,93] including
610 anterodorsal and anteroventral subdivisions of the anterior thalamic nuclei (ATN)[45,47] which
611 regulate contextual memory encoding and specificity, respectively[47]. Apical dendrites from layer
612 V RSC neurons also receive long-range projections from a sparse population of GABAergic CA1
613 neurons that co-regulate RSC activity along with ATN inputs[45]. It is currently unclear how these
614 various inputs to RSC dendrites interact to facilitate clustered synaptic plasticity as well as the
615 linking of contextual memories. Since, the inactivation of hippocampal as well as thalamic inputs
616 to the RSC impairs fear expression[45–47], these inputs likely also regulate the linking of contextual
617 information within the RSC.

618 In addition to the circuit mechanisms that underlie memory linking, the intracellular
619 mechanisms that mediate clustered plasticity and reactivation of the same dendritic
620 compartments are also unknown, but biophysical computational models (Figure 7) should provide
621 testable hypotheses for future investigations. Ex vivo investigations of localized dendritic plasticity
622 have revealed several underlying mechanisms. These include the plasticity of dendritic spikes[8,56],
623 changes in ion channel function[4], signaling pathways[7] as well as protein synthesis-dependent
624 mechanisms[6]. For example, an increase in local dendritic excitability could facilitate dendritic
625 depolarization, which in turn would promote the addition of spine clusters to the same dendritic
626 segment during memory linking.

627 To demonstrate that the dendritic overlap we discovered underlies the linking of contextual
628 memories within RSC ensembles, we modified the TetTag approach to tag and manipulate
629 specific dendritic segments within tagged RSC cells (Figures 6, S6 and S17). Our tagging and
630 manipulation approach involved the addition of a DTE sequence to Channelrhodopsin to restrict
631 Channelrhodopsin expression to recently active dendritic segments. DTE had previously been

632 used to restrict photoactivatable molecules to dendritic segments in an activity-dependent
633 manner[18,65,66].

634 Similar to the reactivation of RSC neuronal ensembles, the reactivation of RSC dendritic
635 ensembles alone allowed us to extend the temporal window during which contextual memories
636 are linked. Importantly, optogenetic activation with TTA-Chr2 (Figure 2e) results in the activation
637 of somas as well as all entire dendritic tree, whereas TTA-Chr2-DTE restricts activation to a
638 smaller subset of dendrites that were previously active (Figure 6f). These results demonstrate
639 that dendritic ensemble overlap plays a key role in memory linking.

640 In the current study we use an established behavioral paradigm to demonstrate that
641 neuronal and dendritic mechanisms in the RSC regulate the linking of two memories experienced
642 five hours apart. We assume that discrete memories that share common elements can be linked
643 and organized together across various dimensions [11] including temporal proximity (such as in our
644 current study), contextual similarity[94] and other common elements among memories[95]. Organizing
645 memories based on these common elements can facilitate various higher-order cognitive
646 processes such as inference, causal reasoning, etc. Therefore, given the obvious evolutionary
647 advantage of linking memories that share common elements to the organism's success, we
648 hypothesize that the mechanisms that allow memory organization are tightly regulated and
649 depend on the conserved features across brain regions. Changes in intrinsic neuronal and
650 dendritic excitability are likely to mediate the linking of memories across various brain regions and
651 various dimensions. Furthermore, such intrinsic processes are ideally positioned to use
652 neuromodulatory systems to determine which memories are linked and which remain independent
653 based on their salience[96].

654 Finally, within the dendritic arbor, inputs from distinct pathways are organized on distinct
655 dendritic domains [97]. This organization along with our current findings suggests that only inputs
656 impinging on the same dendritic compartments might be linked while other inputs remain
657 independent (Figure 7). Therefore, dendritic plasticity mechanisms may facilitate the linking of

658 similar memories that share similar modalities (i.e. two contextual memories) that share similar
659 inputs that synapse onto overlapping dendritic segments. On the other hand, memories encoded
660 by inputs synapsing onto non-overlapping dendritic domains do not benefit from dendritic plasticity
661 mechanisms and thus remain unlinked.

662 Understanding the roles of branch-specific plasticity mechanisms in differentially
663 modulating inputs within a neuron, and by extension, the larger neuronal circuit, is important to
664 understand information processing within a distributed circuit. Importantly, aberrant dendritic and
665 synaptic plasticity mechanisms are also a hallmark of many pathological states, making the
666 findings presented here clinically relevant[98,99].

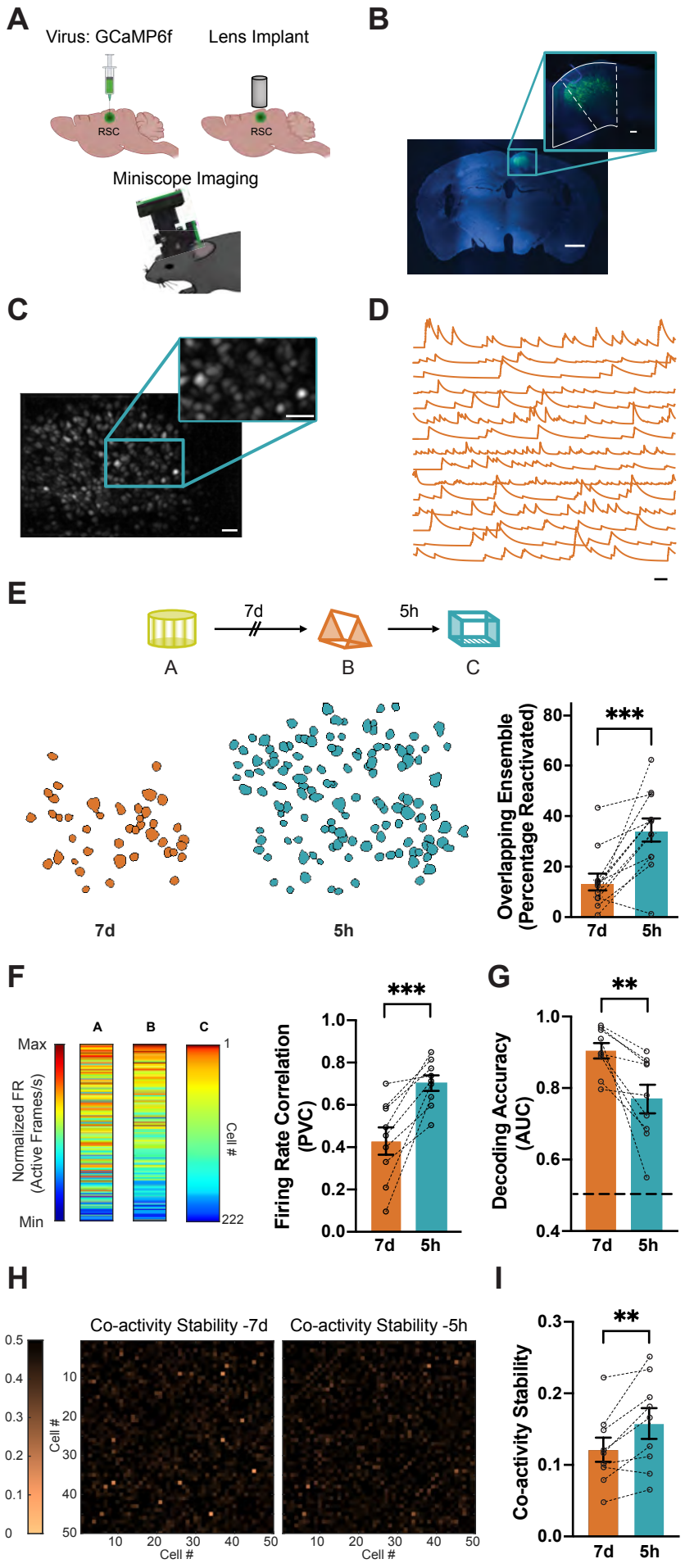
A
Virus: GCaMP6f
Lens Implant
RSC
RSC
Miniscope Imaging
B
C
D
E
7d
5h
A
B
C
7d
5h
Overlapping Ensemble (Percentage Reactivated)
***
7d
5h
F
Max
Min
Normalized FR (Active Frames/s)
A
B
C
1
222
Cell #
Firing Rate Correlation (PVC)
***
7d
5h
G
Decoding Accuracy (AUC)
**
7d
5h
H
Co-activity Stability -7d
Co-activity Stability -5h
Cell #
Cell #
I
Co-activity Stability
**
7d
5h

Figure 1

Figure 1. Overlapping RSC ensembles are recruited to encode contextual memories acquired close in time.

(a) Miniscope methodology: GCaMP6f virus was injected into the RSC, and a Miniscope was used to image calcium transients in RSC neurons across repeated imaging sessions.

(b) GCaMP6f expression within the RSC is limited to specific sub-layers of the RSC. Scale: 1mm; inset, 100 μm.

(c) Example of maximum intensity projection of processed calcium signals during context exploration. Scale: 50 μm.

(d) Representative calcium traces from 15 putative RSC neurons from one mouse. Scale: 30s.

(e) Overlapping RSC ensembles encode distinct memories acquired close in time. Top: Mice were imaged while exploring three novel contexts (A, B, and C) separated by 7 days or 5 hours. Bottom left: Overlapping neurons in RSC ensembles in a representative mouse when contexts were separated by 7 days (orange) and 5 hours (blue). Bottom right: RSC neuronal ensembles display greater overlap when contexts were separated by 5 hours (5h) vs. 7 days (7d; n = 12 mice per group, paired t-test, t = 4.8). The physical contexts presented were counterbalanced to minimize any effect of context similarity.

(f) Frequency of calcium transients in the RSC ensemble is more correlated when two contexts are explored close in time. Left: Frequency of calcium transients (active frames/s) for all RSC neurons from one mouse during each context exploration ranked based on their normalized frequency of calcium transients in context C. RSC neurons with a high frequency of calcium transients continue to fire at high rates when contexts are explored close in time (5 hours vs. 7 days apart). Right: Population Vector Correlation (PVC) for normalized firing rates is higher when contexts are explored close in time (i.e., 5 hours vs 7 days apart; n = 9 mice per group; paired t-test, t = 5.1).

(g) A Naïve Bayes (NB) classifier is better at distinguishing two contexts explored 7 days apart vs 5 hours apart. The AUC (area under the curve) for the binary NB classification, using neuronal activity between sessions, is higher for sessions recorded 7 days apart than sessions recorded 5 hours apart (n = 9 mice per group; paired t-test, t = 3.5). Chance level performance of the classifier (AUC = 0.5) is represented by a dashed line. Spike probabilities were binned at 10 seconds in non-overlapping intervals.

(h) Representative neuronal coactivity across sessions: The stability of neuronal coactivity across sessions is represented as the absolute difference in pairwise correlations between sessions (i.e. Pairwise correlation for Session 2 – Pairwise correlation for Session 1). Absolute difference in coactivity when contexts are explored 7 days (left panel) or 5 hours (right panel) for 50 cell pairs. Higher numbers (darker color) indicate more stable coactivity patterns.

(i) Neuronal coactivity is more stable when contexts are explored close in time**.** The coactivity of neuronal pairs is more stable in two contexts explored 5h vs 7d apart (see Methods for details, n = 9 mice per group; paired t-test, t = 3.4).

Data represent mean ± s.e.m. and each data point, * $p < 0.05$, ** $p < 0.01$, *** $p < 0.001$.

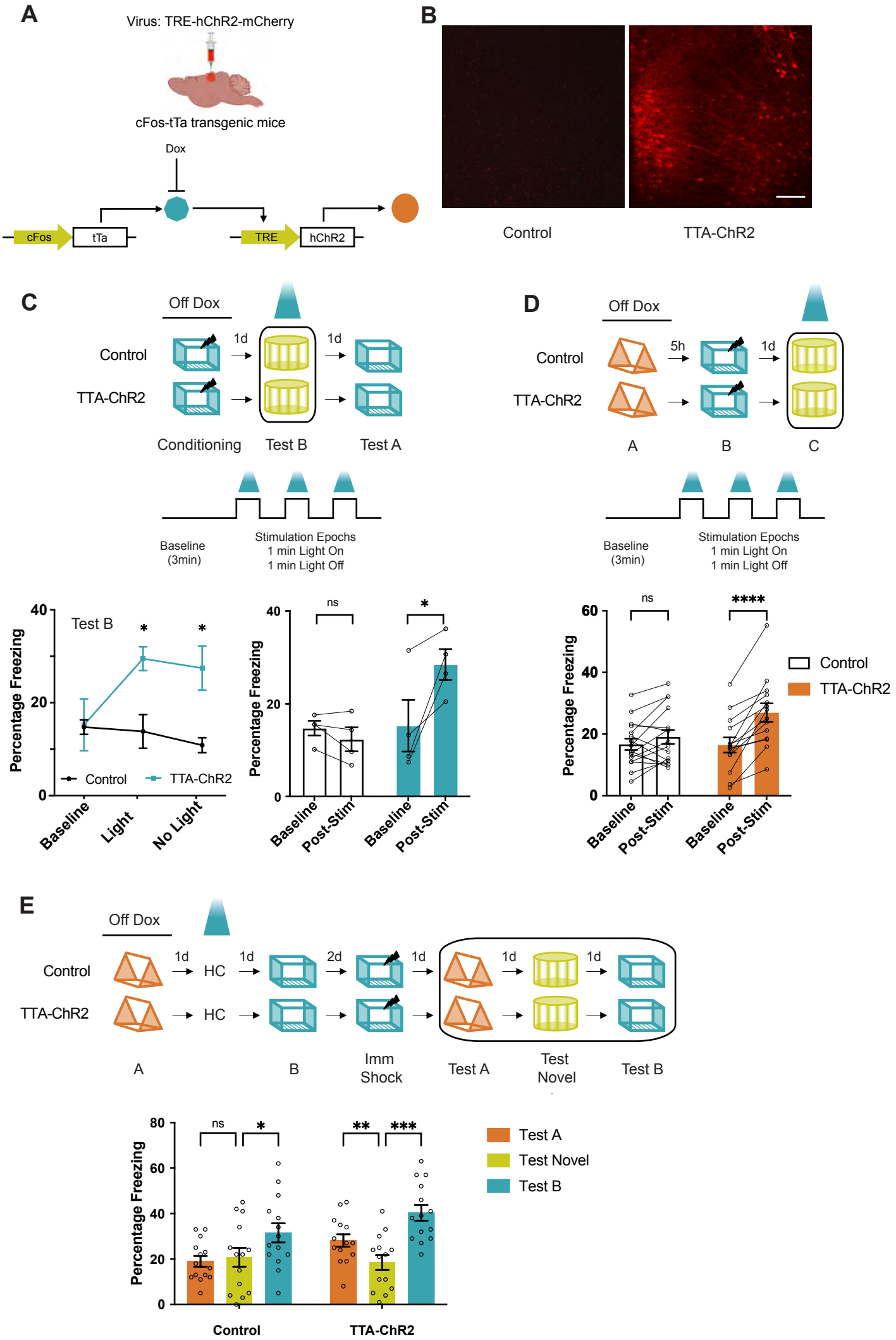
A
Virus: TRE-hChR2-mCherry
cFos-tTa transgenic mice
Dox
cFos
tTa
TRE
hChR2
B
Control
TTA-ChR2
C
Off Dox
Control
TTA-ChR2
1d
1d
Conditioning
Test B
Test A
Baseline (3min)
Stimulation Epochs
1 min Light On
1 min Light Off
D
Off Dox
Control
TTA-ChR2
5h
1d
A
B
C
Baseline (3min)
Stimulation Epochs
1 min Light On
1 min Light Off
Test B
Percentage Freezing
Control
TTA-ChR2
Baseline
Light
No Light
ns
*
Post-Stim
****
E
Off Dox
Control
TTA-ChR2
1d
HC
2d
A
B
Imm Shock
Test A
Test Novel
Test B
**
***
Test A
Test Novel
Test B

Figure 2

716 **Figure 2. Overlap in RSC neuronal ensembles is sufficient to link contextual memories.**
717
718 (a) Schematic of the TetTag system: cFos-tTa or wildtype littermate mice were injected with the
719 TRE-hChR2-mCherry virus. In the absence of doxycycline, the activation of the cFos promoter
720 allows the expression of Channelrhodopsin (hChR2).
721
722 (b) ChR2-mCherry expression in the RSC one day after fear learning in the experimental and
723 control groups. Scale: 100 µm.

724 (c) Optogenetic reactivation of an RSC ensemble underlying a fearful context is sufficient for fear
725 expression: Top: Experimental setup: cFos-tTa (TTA-Chr2) mice and their wildtype littermates
726 (Control) underwent bilateral viral injections (TRE-ChR2-mCherry) and optic cannula implants.
727 Mice were taken off doxycycline chow (three days before contextual fear conditioning in context
728 A: 2 footshocks, 2s, 0.7mA) to allow c-fos promoter driven tTA and Channelrhodopsin (ChR2)
729 expression. Following contextual fear conditioning, mice were tested in a novel context (Test B)
730 while the previously tagged neurons were activated. The following day mice were retested without
731 any optogenetic manipulation in the training context (Test A). Middle: Optogenetic stimulation
732 (473nm laser, 5 ms pulses, 5 Hz) was preceded by 3 mins of context acclimation, followed by
733 three 1-minute trials of light pulses, separated by a 1-minute period of light off. Bottom: During
734 Test B, TTA-Chr2 mice and control mice display similar freezing levels during the baseline period.
735 Upon reactivation of the RSC neuronal ensemble tagged during contextual fear conditioning, TTA-
736 Chr2 mice display more freezing compared to the control group during the post-baseline
737 stimulation as well as non-stimulation epochs (n = 4 mice per group; Two-way RM ANOVA, group
738 X time interaction, $F(2, 12) = 6.95$, $p < 0.01$, Uncorrected Fisher's LSD, $p < 0.05$).

739 (d) Optogenetic reactivation of an RSC ensemble underlying a linked memory is sufficient for fear
740 expression: Top: RSC ensemble activated during the exploration of the first context (context A)
741 was tagged. Five hours later, the second context (context B) was paired with a footshock. The
742 following day, mice were tested in a third novel context (context C) with optogenetic reactivation
743 of the tagged (Context A) RSC neuronal ensemble. Bottom: Reactivation of the RSC neuronal
744 ensemble tagged during the linked context exploration (context A) increases freezing in cFos-tTa
745 mice during the post-stimulation period, while the freezing in the control group remains unchanged
746 (n = 16 and 14 mice for Control and cFos-tTa groups; Two-way RM ANOVA, $F_{Interaction}(1, 28) =$
747 12.5, $p < 0.001$; Sidak's multiple comparisons test; Baseline freezing (Control vs. TTA-ChR2: $p =$
748 0.99); Post-Stim freezing (Control vs. TTA-ChR2: $p < 0.05$).
749
750 (e) Reactivation of the RSC ensemble underlying the first context memory (context A) extends
751 the temporal window for memory linking: Mice were allowed to explore 2 contexts (context A and
752 B) separated by 2 days (a time interval when memories are not linked). On the day between the
753 two context exposures, the RSC ensemble tagged during the first context visited (context A) was
754 reactivated optogenetically. While control mice do not link the 2 contexts, reactivation of the first
755 context ensemble leads to robust contextual memory linking: freezing in both previously explored
756 contexts (Context A: linked context and Context B: shock context) is higher than the freezing in a
757 novel context. The control group freeze similarly in context A and novel context, but the freezing
758 in context B (shock context) is higher than freezing in a novel context (n = 14 mice each for Control
759 and cFos-tTa groups; Two-way RM ANOVA, $F_{GroupXContext}(2, 52) = 3.3$, $p < 0.04$; Dunnett's multiple
760 comparisons test for contexts).
761
762 The physical contexts presented were counterbalanced to minimize any effect of context
763 similarity. Data represent mean ± s.e.m. and each data point, * $p < 0.05$, ** $p < 0.01$, *** $p < 0.001$.

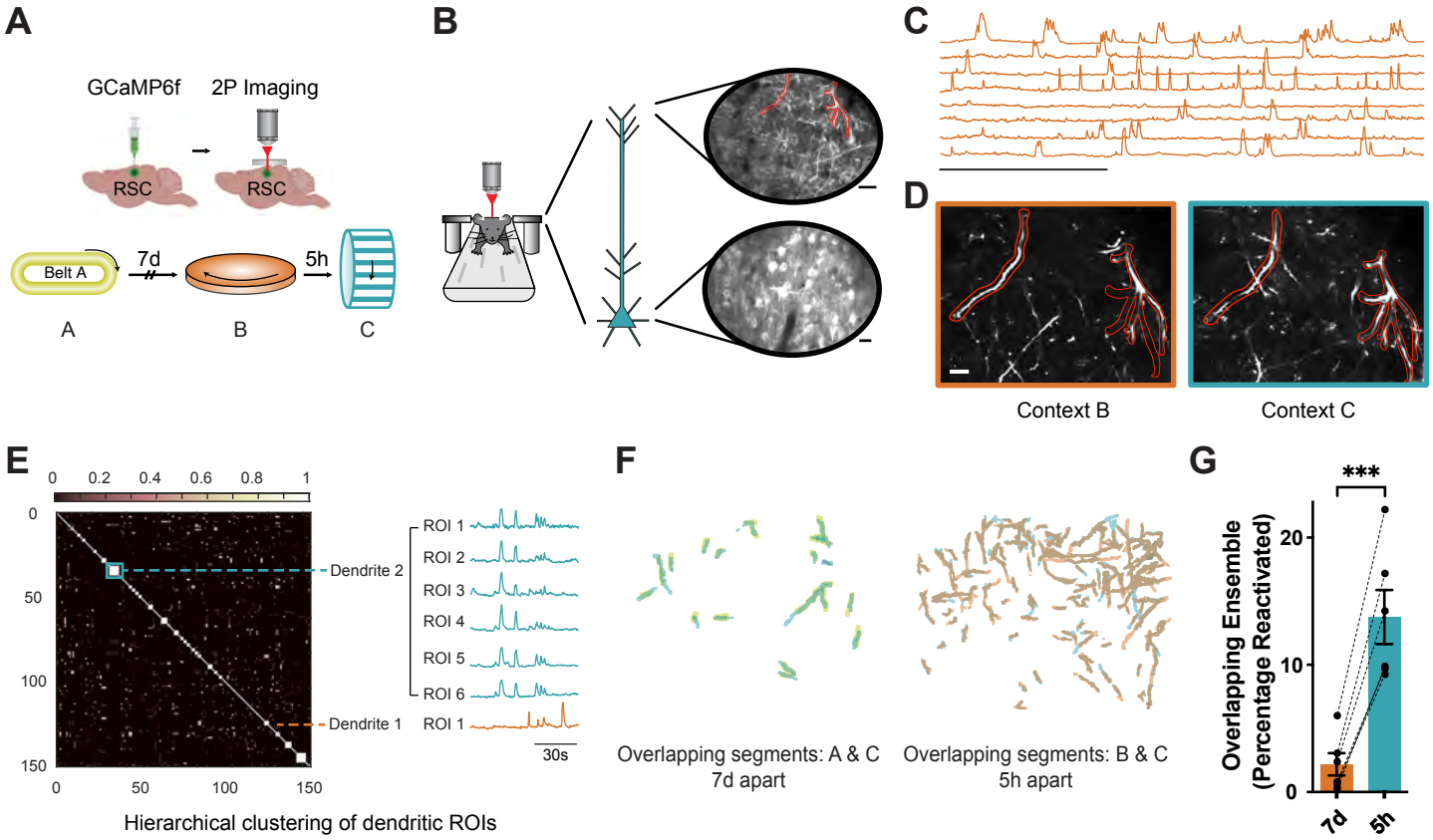
A
GCaMP6f
2P Imaging
RSC
RSC
Belt A
7d
5h
A
B
C
B
C
D
Context B
Context C
E
Dendrite 2
Dendrite 1
ROI 1
ROI 2
ROI 3
ROI 4
ROI 5
ROI 6
ROI 1
30s
Hierarchical clustering of dendritic ROIs
F
Overlapping segments: A & C
7d apart
Overlapping segments: B & C
5h apart
G
***
Overlapping Ensemble
(Percentage Reactivated)
7d
5h

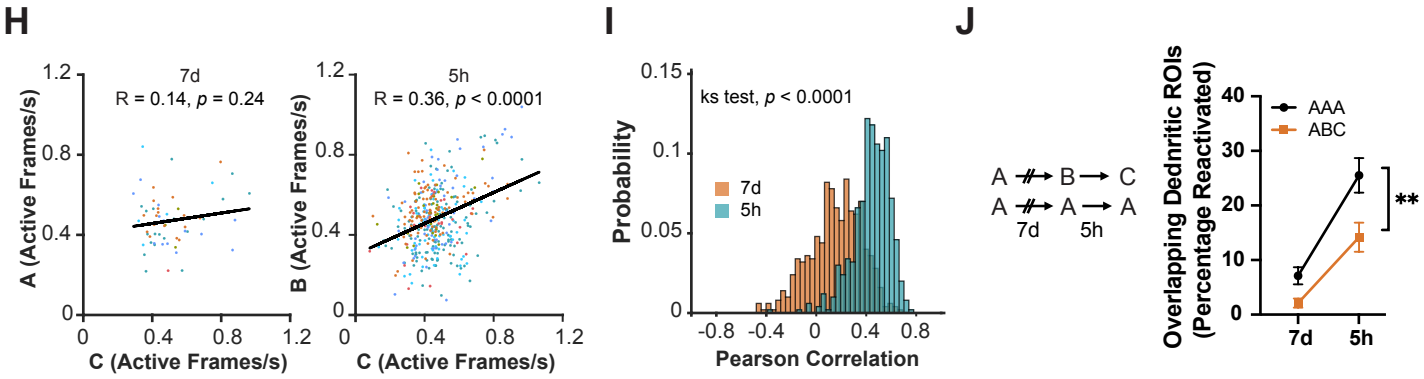
H
7d
R = 0.14, p = 0.24
5h
R = 0.36, p < 0.0001
A (Active Frames/s)
B (Active Frames/s)
C (Active Frames/s)
I
ks test, p < 0.0001
7d
5h
Probability
Pearson Correlation
J
A → B → C
A → A → A
7d
5h
AAA
ABC
**
Overlapping Dednritic ROIs
(Percentage Reactivated)

Figure 3

Figure 3. Overlapping dendritic segments encode memories of two contexts explored close in time.

(a) Experimental setup: A 3 mm square craniotomy was made over the RSC spanning the midline, and GCaMP6f was injected bilaterally into the RSC. During imaging sessions, mice were head-fixed and experienced three novel contexts either 7 days or 5 hours apart as calcium transients were imaged using a two-photon microscope. Contexts comprised distinct visual, auditory, olfactory, and tactile cues and were counterbalanced (Figure S10).

(b) RSC neurons and dendritic segments were tracked across 7 days. Top: Maximum intensity projection from one imaging session showing apical dendritic segments activated during the contextual experience. Two different dendritic segments are outlined in red. Scale: 20 μm. Bottom: Mean frame from one imaging session showing layer V RSC neurons. Scale: 10 μm.

(c) Representative calcium traces from 8 putative RSC dendritic segments. Scale: 2 min.

(d) Dendritic segments from (b) tracked across two imaging sessions 5 hours apart. Scale: 10 μm

(e) Hierarchical clustering of RSC dendritic ROIs: Sorted cosine similarity matrix of 150 ROI pairs from one animal. Blue box and line depict the correlated calcium activity of 6 ROIs clustered as a single dendrite. Orange: Single ROI which was not clustered with ROIs in blue or any other ROI.

(f) Overlapping dendritic segments reactivated when contexts are separated by 7 days (left) or 5 hours (right) from one mouse.

(g) The same dendritic segments are more likely to be activated when context exposures are 5 hours (5h) apart vs 7 days (7d) apart. (Paired t-test; $t = 9.2$; $p < 0.0005$; n=6 mice).

(h) Dendritic activity (active frames per second) is more correlated when dendrites are reactivated 5h vs 7d apart. Scatter plot of firing rate of all reactivated ROIs in context A (7d, 7 days apart) and context B (5h, 5 hours apart) as a function of firing rate in context C. Lines represent least-squares linear regression. Data from each mouse is represented in a different color.

(i) Data from (h) were subsampled (30 ROI pairs, 500x) to generate a probability distribution of Pearson correlations (K-S test, $p < 0.0001$).

(j) Dendritic overlap is greater when mice explore the same context vs distinct contexts (Two-way RM ANOVA, ABC vs AAA, $p < 0.05$; Sidak's post hoc test, ABC, AAA (5h vs 7d) $p < 0.001$). Data represent mean ± s.e.m. and each data point.

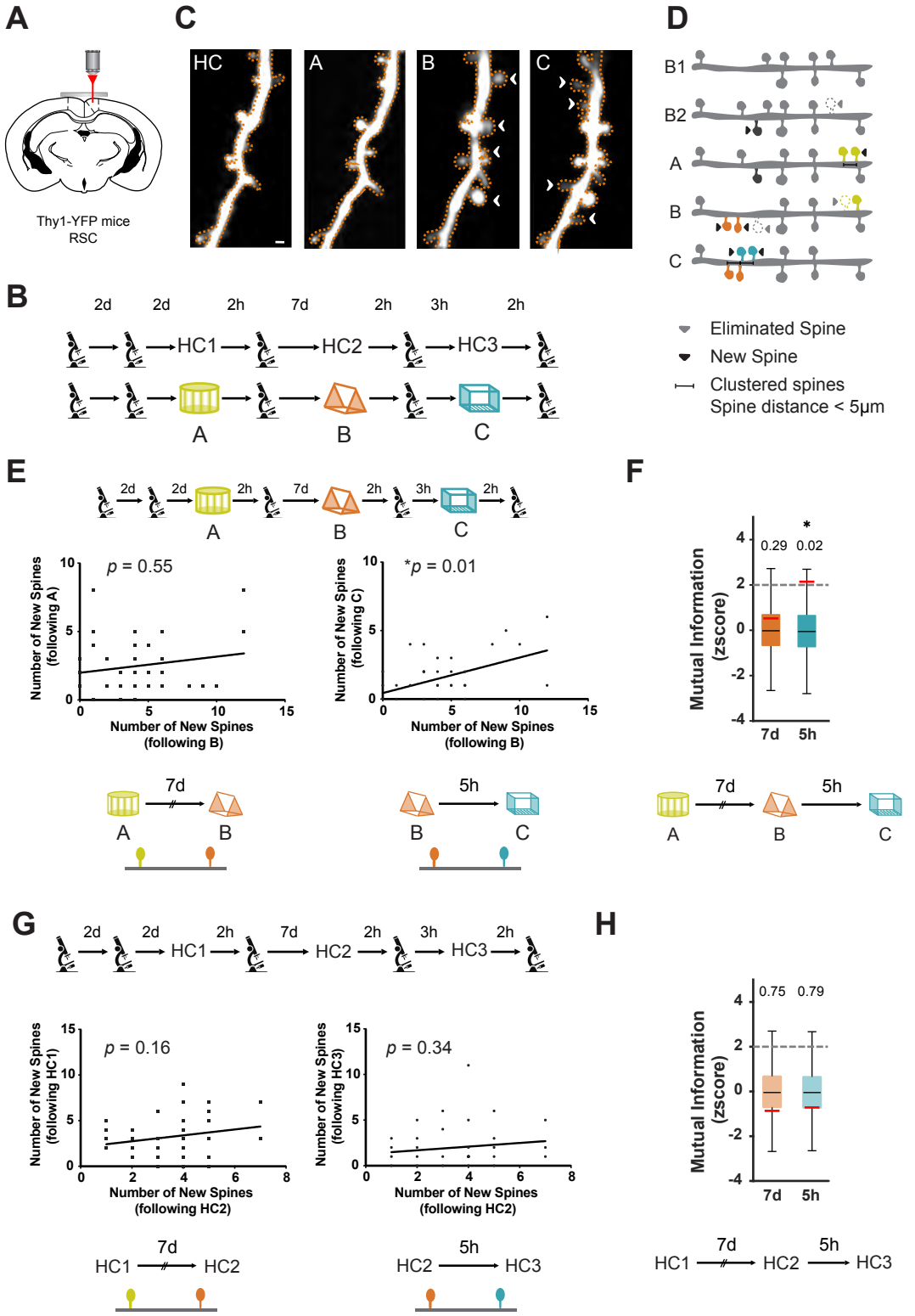
A
Thy1-YFP mice
RSC
C
HC
A
B
C
D
B1
B2
A
B
C
Eliminated Spine
New Spine
Clustered spines
Spine distance < 5μm
B
2d 2d 2h 7d 2h 3h 2h
HC1
HC2
HC3
A
B
C
E
p = 0.55
*p = 0.01
Number of New Spines (following A)
Number of New Spines (following C)
Number of New Spines (following B)
7d
5h
F
Mutual Information (zscore)
0.29 0.02
7d 5h
G
p = 0.16
p = 0.34
Number of New Spines (following HC1)
Number of New Spines (following HC3)
Number of New Spines (following HC2)
HC1 HC2 HC3
H
0.75 0.79
Mutual Information (zscore)
7d 5h

Figure 4

Figure 4. Spines are added to overlapping dendritic segments following memory linking.

(a) Experimental setup: A 3 mm square craniotomy was made over the RSC of Thy1-YFP mice. Apical RSC dendrites were imaged to measure context exposure and memory linking related spine dynamics.

(b) Mice received contextual exposure to three distinct contexts 7 days or 5 hours apart. Control mice were imaged at time-matched intervals without context exposure.

(c) Representative example of spine dynamics during longitudinal imaging showing clustering of new spines following linked memory formation. Gained spine: white arrowhead. HC: Last baseline imaging session; A, B and C: Exposure to contexts A, B and C respectively. Scale: 1 μm.

(d) Schematic of various spine dynamics (spine addition, elimination, and clustering) measured.

(e) New spines are likely to be added to the same dendritic segments when contexts are explored close in time. Left: Number of new spines added to a dendritic segment following Context A and B exposure 7 days apart are not correlated (ρ = 0.09, p = 0.55). Right: Number of new spines added to a dendritic segment following Context B and C exposure 5 hours apart are correlated (n = 6 mice, ρ = 0.37, p = 0.01). Spearman's correlation was used. Alpha level was adjusted to 0.025 to account for multiple comparisons.

(f) Mutual information between new spines added at 7 days or 5 hours apart is higher for spines added following context exposures 5 hours vs 7 days apart. Observed values (red line) were compared to the z-score of a chance distribution.

(g) For home cage (HC) controls, the numbers of new spines added to a dendritic segment are not correlated whether imaging sessions are separated by either 7 days (right, ρ = 0.22, p = 0.16) or 5 hours (left, ρ = 0.15, p = 0.34; n = 5 mice).

(h) Mutual information between new spines added at 7 days or 5 hours is unchanged in control mice. Observed values (red line) were compared to the z-score of a chance distribution.

The physical contexts presented were counterbalanced to minimize any effect of context similarity.

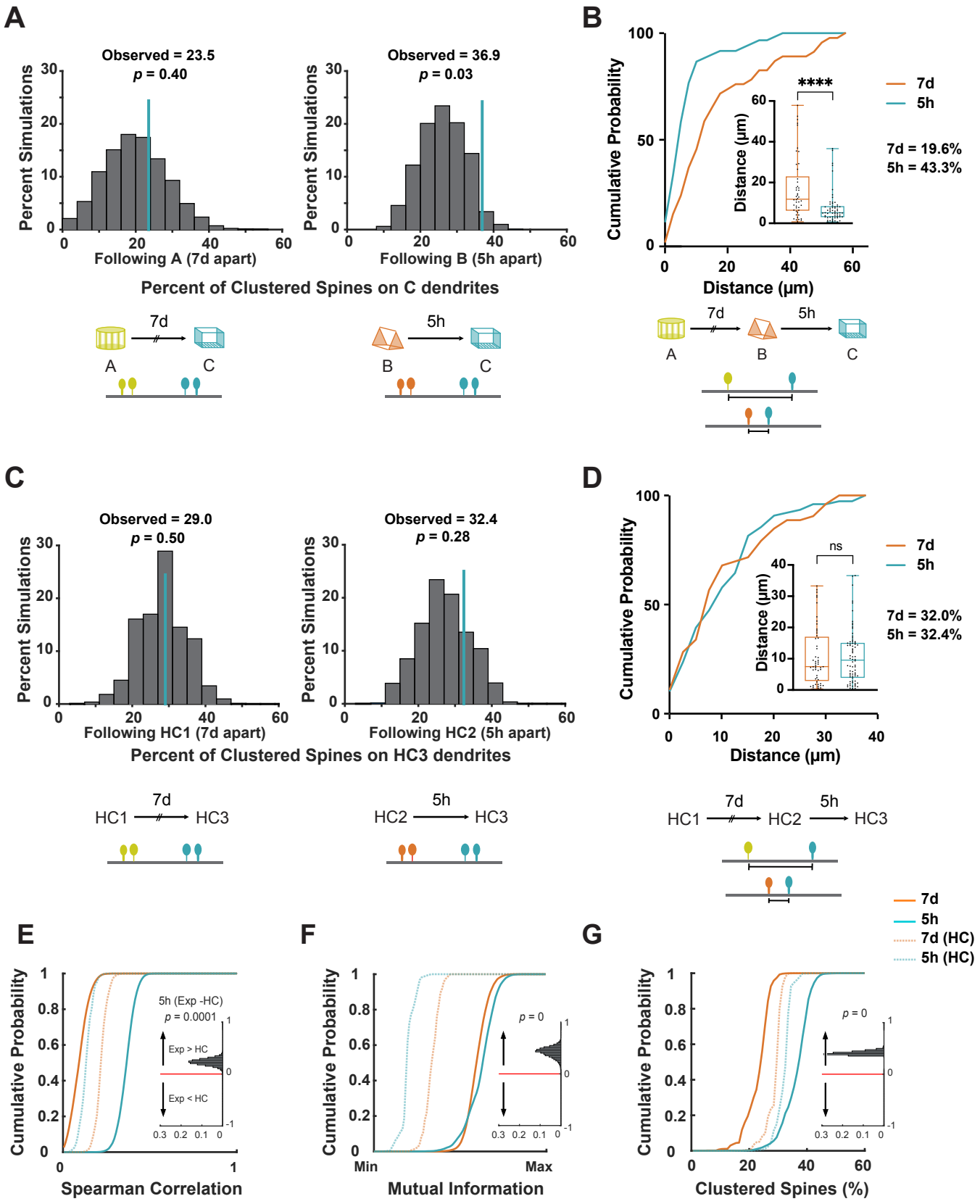
A
Observed = 23.5
p = 0.40
Percent Simulations
Following A (7d apart)
Observed = 36.9
p = 0.03
Following B (5h apart)
Percent of Clustered Spines on C dendrites
7d
5h
A
B
C
B
Cumulative Probability
Distance (µm)
****
7d
5h
7d = 19.6%
5h = 43.3%
C
Observed = 29.0
p = 0.50
Following HC1 (7d apart)
Observed = 32.4
p = 0.28
Following HC2 (5h apart)
Percent of Clustered Spines on HC3 dendrites
HC1
HC2
HC3
D
ns
7d = 32.0%
5h = 32.4%
E
5h (Exp -HC)
p = 0.0001
Exp > HC
Exp < HC
Spearman Correlation
F
p = 0
Min
Max
Mutual Information
G
7d (HC)
5h (HC)
Clustered Spines (%)

Figure 5

Figure 5. Overlapping dendritic segments gain spine clusters following memory linking.

(a) Co-allocation of clustered spines to dendritic segments: The probability that clustered spines are co-allocated to the same dendritic segment by chance following two imaging sessions was calculated by randomly distributing clustered spine positions following one imaging session. Left: The percentage of clustered spines co-allocated to the same dendritic segments following contexts A and C (explored 7 days apart) are at chance levels. Right: In contrast, the percentage of clustered spines co-allocated to the same dendritic segments following contexts B and C (explored 5 hours apart) is higher than expected by chance. n = 6 mice; 10000 permutations.

(b) New spines following context exposures 5 hours, but not 7 days, apart are formed close to one another (KS test, p <0.0001). Inset: Average distance between newly formed spines following exposure to contexts A and C (7d) or contexts B and C (5h). (Mann Whitney, p <0.0001)

(c) For home cage (HC) controls, the percentage of clustered spines that were added to segments also containing clustered spines in a previous imaging session (7 days or 5 hours prior) were at chance levels; n = 5 mice; 10000 permutations.

(d) New spines formed in home cage control mice do not co-cluster for imaging sessions 5 hours or 7 days apart (KS test). Inset: Average distance between newly formed spines in home cage controls 7-days or 5-hours apart. (Mann Whitney test).

(e) Cumulative distribution of Spearman's rho (ρ) values calculated by randomly subsampling 40 dendritic branches 10,000x for each condition. ρ values quantify the rank correlation between the number of new spines added to the same branch between two time points 5h or 7d apart. Inset demonstrates that the Spearman's rho (ρ) is higher for resampled experimental vs HC group at 5h (p < 0.001).

(f) Cumulative distribution of mutual information (MI) values calculated by randomly subsampling 40 dendritic branches 10,000x for each condition. MI values quantify the amount of information obtained about the new spines added to a branch by observing the number of new spines added to the same branch in a previous session 5h or 7d before. Inset demonstrates that the Mutual information is higher for resampled experimental vs HC group at 5h (p < 0.0001).

(g) Cumulative distribution of values of the percentage of clustered spines among 40 dendritic branches randomly subsampled 10,000x for each condition. The percentage of clustered spines values quantify, among all clustered spines added after a session, the percentage added to the same branches that received clustered spines in a previous session 5h or 7d before. Inset demonstrates that the probability of gaining a clustered spine on a segment already containing a clustered spine during a previous session is higher for resampled experimental vs HC group at 5h (p < 0.0001).

The physical contexts presented were counterbalanced to minimize any effect of context similarity.

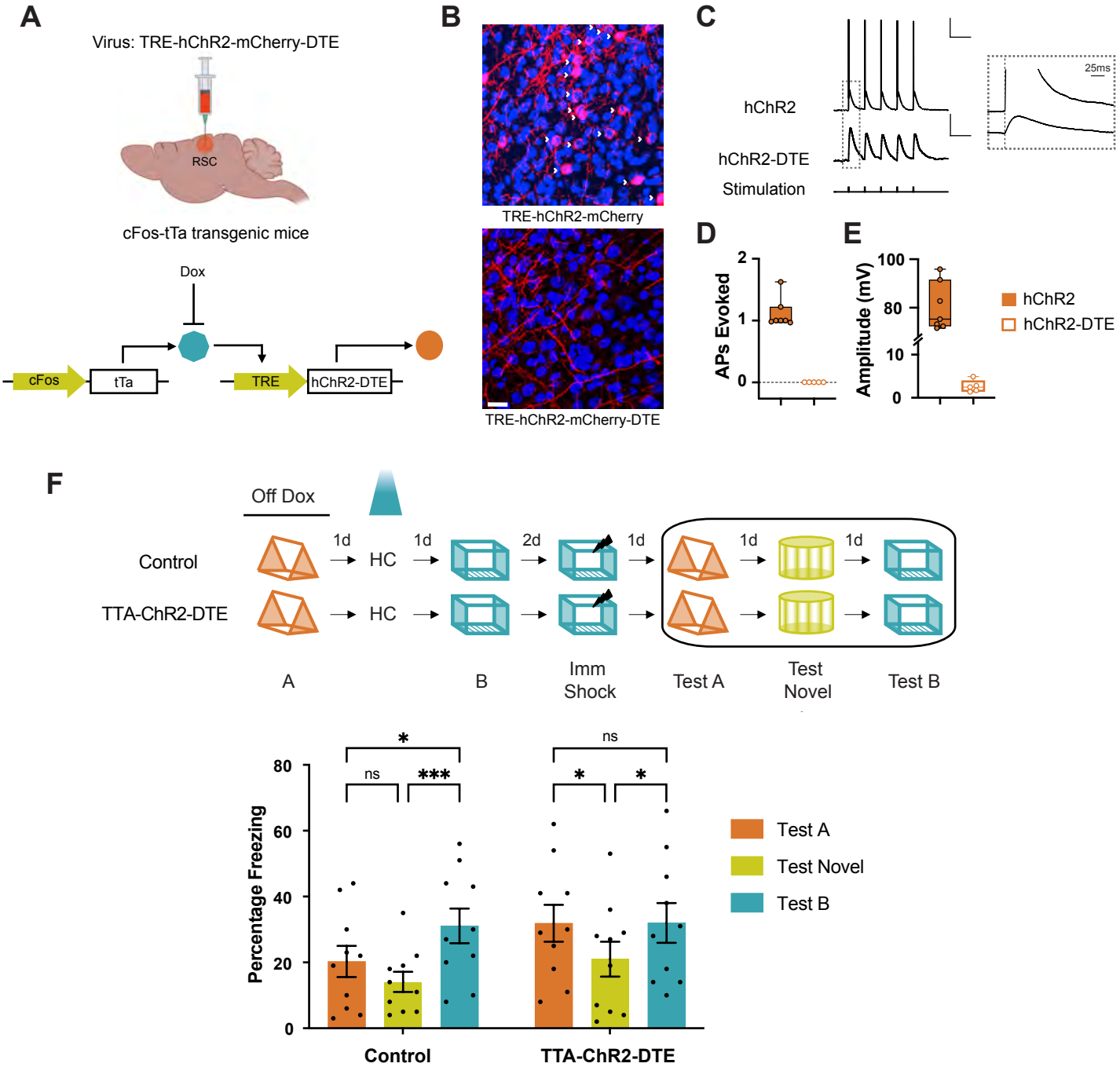
A
Virus: TRE-hChR2-mCherry-DTE
RSC
cFos-tTa transgenic mice
Dox
cFos
tTa
TRE
hChR2-DTE
B
TRE-hChR2-mCherry
TRE-hChR2-mCherry-DTE
C
hChR2
hChR2-DTE
Stimulation
25ms
D
APs Evoked
E
Amplitude (mV)
hChR2
hChR2-DTE
F
Off Dox
Control
TTA-ChR2-DTE
1d
HC
2d
Imm Shock
Test A
Test Novel
Test B
Percentage Freezing
ns
***
Control
TTA-ChR2-DTE

Figure 6

Figure 6. Optogenetic reactivation of RSC dendritic ensembles links contextual memories

(a) The TRE-hChr2-mCherry-DTE virus was designed to optogenetically reactivate previously activated dendritic segments. The key genetic elements include 1) TRE promoter and 2) Dendritic Targeting Element (DTE) at the 5' end: The DTE element targets mRNA to activated dendrites and has been used to target photoactivatable molecules to activated dendrites/spines (*8*). TRE-hChr2-mCherry-DTE virus was injected into cFos-tTa mice to express Channelrhodopsin in the recently activated dendritic segments of cFos-expressing neurons.

(b) Representative RSC images of cFos-tTa mice injected with TRE-hChR2-mCherry-DTE (left) and TRE-hChR2-mCherry (right) showing selective expression of Channelrhodopsin in dendritic segments in the presence of DTE. White arrowheads: somatic expression of hChR2 in the absence of DTE. Scale: 20 µm

(c) Whole-cell patch-clamp recordings from RSC neurons of cFos-tTa mice tagged using TRE-Chr2 or TRE-Chr2-DTE constructs. Representative waveforms showing optogenetic stimulation of RSC neurons from TTA-ChR2 and TTA-ChR2-DTE mice results in somatic responses in the form of action potentials and transient depolarizations respectively. Scale, 20mV (top), 1mV (bottom); 250ms. Inset: Magnified view of the first optogenetic stimulation showing response latencies of the stimulus onset. Scale, 25ms.

(d) Average number of action potentials elicited and (e) response amplitudes in TTA-ChR2 and TTA-ChR2-DTE mice. (Mann Whitney test, $p < 0.005$; TTA-ChR2: n = 7 cells, N =3 mice and TTA-ChR2-DTE: n = 5 cells, N =3 mice). Only neurons with detectable responses were plotted.

(f) Experimental setup: Top: Mice explored two contexts 2 days apart (a time interval when memories are not linked). The physical contexts presented were counterbalanced to minimize any effect of context similarity. On the day between the 2 context exposures, the dendrites activated during the first context exposure were reactivated optogenetically. Bottom: Reactivation of context A dendrites, on the day between the two context exposures (contexts A and B), results in high freezing in both the previously explored contexts (context A: linked context and context B: shock context) relative to freezing in a novel context. The control mice freeze similarly in context A and novel context, but the freezing in context B (shock context) is higher than freezing in context A or a novel context (n = 10 mice each for Control and cFos-tTa groups; Two-way RM ANOVA, $F_{time}(2, 36) = 14.11$, $P < 0.001$; Dunnett's multiple comparisons test). Data represent mean ± s.e.m. and each data point, * $p < 0.05$, ** $p < 0.01$, **** $p < 0.0001$.

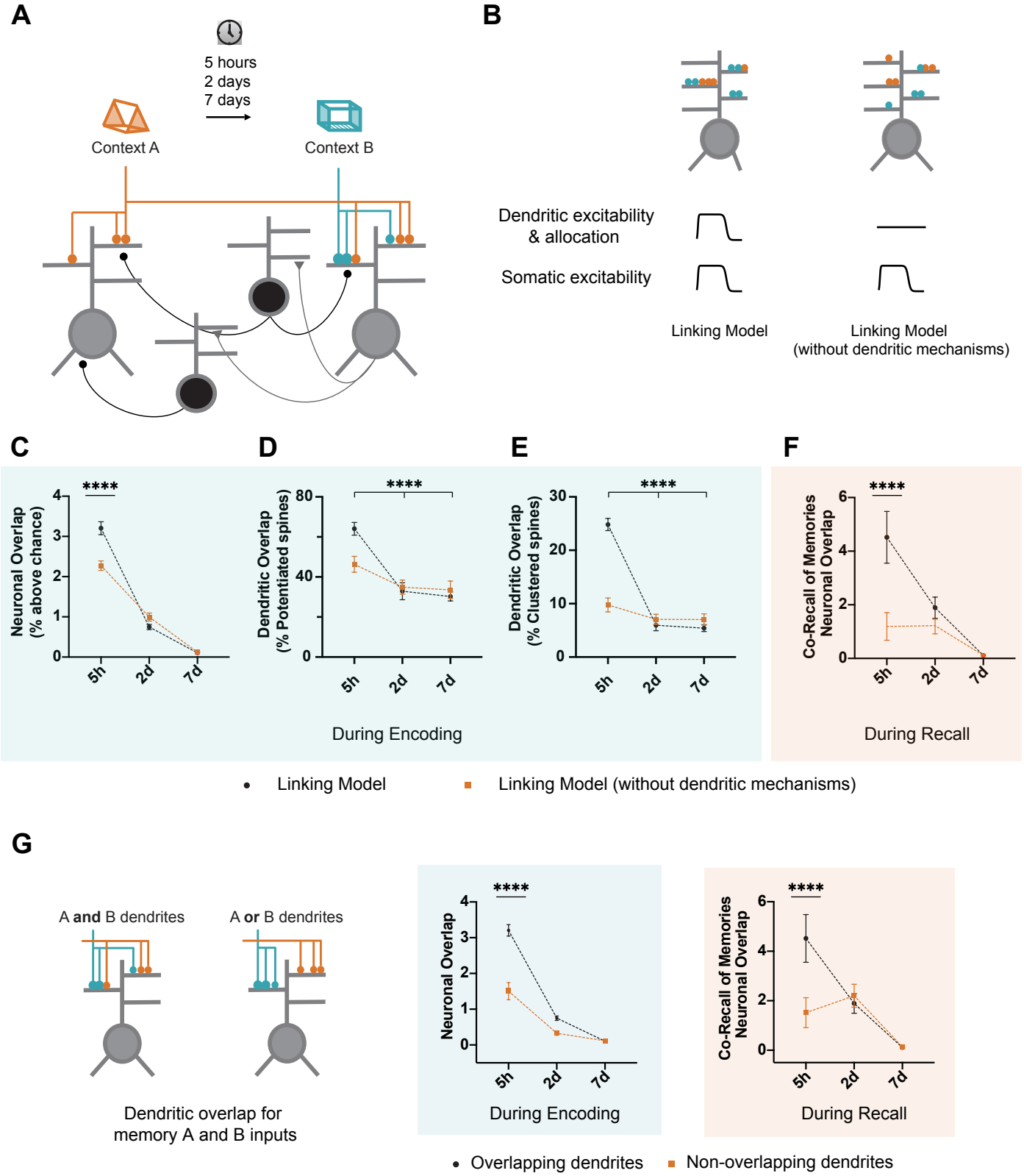
A
5 hours
2 days
7 days
Context A
Context B
B
Dendritic excitability & allocation
Somatic excitability
Linking Model
Linking Model (without dendritic mechanisms)
C
D
E
F
Neuronal Overlap (% above chance)
Dendritic Overlap (% Potentiated spines)
Dendritic Overlap (% Clustered spines)
Co-Recall of Memories Neuronal Overlap
****
5h
2d
7d
During Encoding
During Recall
Linking Model
Linking Model (without dendritic mechanisms)
G
A and B dendrites
A or B dendrites
Dendritic overlap for memory A and B inputs
Neuronal Overlap
Co-Recall of Memories Neuronal Overlap
During Encoding
During Recall
Overlapping dendrites
Non-overlapping dendrites

Figure 7

Figure 7. Dendritic mechanisms are necessary for linking memories acquired close in time in a spiking network model.

a) Schematic of the spiking network model. The network consists of 2-layer excitatory neurons (gray) with dendritic subunits, and subpopulations of dendrite-targeting and soma-targeting interneurons (black). See Methods for details.

b) Details of the learning-related plasticity mechanisms within the two network models: The linking model contains somatic and dendritic allocation mechanisms such that memory formation results in increases in somatic and dendritic excitability, and synapses are more likely to be potentiated in the presence of preexisting potentiated synapses on the same dendrite (see Methods). To assess the contribution of dendritic mechanisms to memory linking, learning-related changes in dendritic excitability and probability of synaptic potentiation are eliminated in the linking model without dendritic mechanisms.

c) Neuronal overlap during the encoding of two memories acquired 5 hours, 2 days or 7 days apart. When dendritic mechanisms (dendritic allocation mechanisms and increased dendritic excitability) are removed from the model, neuronal overlap during encoding is reduced when memories are acquired 5 hours (5h) apart. Neuronal overlap represents percentage above chance overlap.

d) Overlap between dendritic branches containing potentiated synapses following two memories acquired 5 hours, 2 days or 7 days apart. When dendritic mechanisms are removed from the model, overlap between dendritic branches with potentiated spines is reduced when memories are acquired 5 hours (5h) apart.

e) Overlap between dendritic branches containing newly added clustered spines following two memories acquired 5 hours, 2 days or 7 days apart. When dendritic mechanisms are removed from the model, overlap between dendritic branches with newly added clustered spines is reduced when memories are acquired 5 hours (5h) apart.

f) Co-recall of two memories as measured by neuronal overlap during recall. When dendritic mechanisms are removed from the model, co-recall of two memories (as measured by neuronal overlap during recall) is reduced when memories are acquired 5 hours (5h) apart. In addition, when dendritic mechanisms are removed from the model, neuronal overlap during recall is not different whether memories are acquired 5 hours, 2 days or 7 days apart indicating that dendritic mechanisms are necessary for linking of memories acquired close in time.

Two-way RM ANOVA. Dunnett's multiple comparisons for Figure 7c-e: linking model and linking model (without dendritic mechanisms): 5h vs 2d and 5h vs 7d, all p values < 0.0001. For Figure 7f, linking model: 5h vs 2d and 5h vs 7d, all p values < 0.0001 but for linking model (without dendritic mechanisms): 5h vs 2d and 5h vs 7d, all p values = non significant. Sidak's multiple comparisons for Figure 7c-e, overlaps at 5h for linking model vs linking model (without dendritic mechanisms): all p values < 0.0001. For simplicity only comparisons within the linking model without dendritic mechanisms are presented (5h vs 2d or 5h vs 7d, **** p < 0.0001).

(g) Dendritic overlap allows somatic overlap and co-recall of memories. Inputs representing context A and B impinge on overlapping or completely separate dendrites (dendritic overlap is eliminated). During encoding and recall, neuronal overlap is reduced between groups at 5h but not 2d and 7d time intervals (Sidak's posthoc, p < 0.0001). When memories are encoded by non-

968 overlapping dendrites, neuronal overlap is similar between 5h, 2d and 7d group (for overlapping
969 dendrites group, Dunnett's posthoc, $p < 0.0001$).
970
971 Neuronal overlap represents percentage above chance overlap (see Methods). Data represent
972 mean ± s.e.m. of 10 simulation trials.

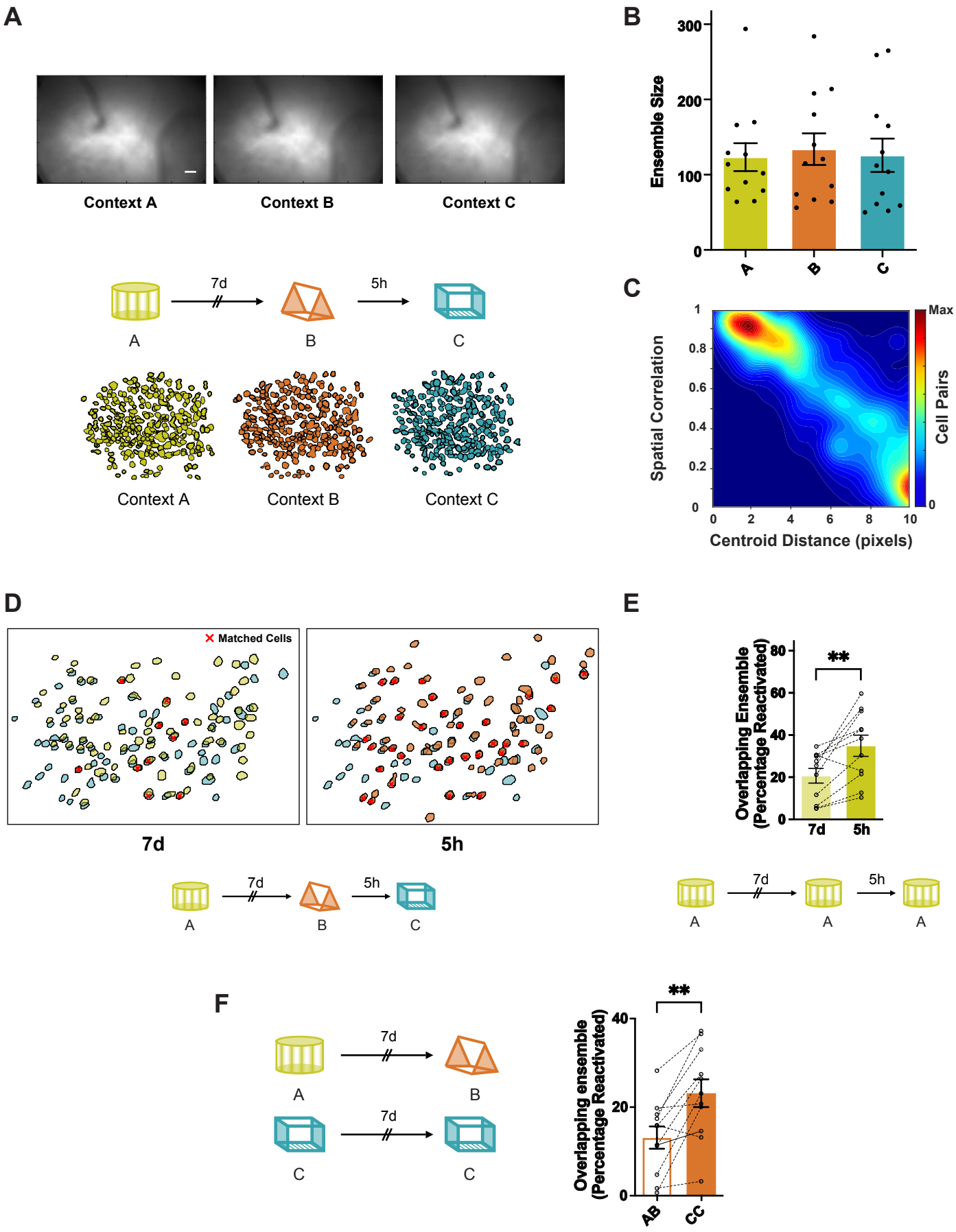
A
Context A
Context B
Context C
7d
5h
A
B
C
Context A
Context B
Context C
B
Ensemble Size
300
200
100
0
A
B
C
C
Spatial Correlation
Centroid Distance (pixels)
Max
Cell Pairs
D
Matched Cells
7d
5h
E
Overlapping Ensemble (Percentage Reactivated)
**
7d
5h
F
Overlapping ensemble (Percentage Reactivated)
**
AB
CC

Figure S1

Supplementary figures

Figure S1. Stability of imaging and neuronal registration across days.
(a) Top: Images of mean fluorescence from each session from a representative mouse. Scale: 50 µm. These images from each session were cross-registered with each other (see Methods for details). Bottom: Description of imaging paradigm and RSC ensemble segmented from a mouse.

(b) RSC ensemble size captured by Miniscope imaging remains stable across hours and days when different contexts are imaged (4599 putative RSC neurons, 132.9 ± 11.6 neurons per session, One-way repeated measures ANOVA, $F(1.08, 11.9) = 0.52$, $p = 0.5$, n = 12 mice per group). Please note that although the size of these ensembles remains unchanged, the neurons participating in these ensembles may change. Data represent mean ± s.e.m. and each data point.

(c) Spatial correlation and centroid distance were calculated for all cell pairs from all mice. Ensemble overlap using a range of criteria from spatial correlation ≥ 0.6 -0.95 and centroid distance ≤ 3-9 pixels is shown in Supplementary Table 1.

(d) Example cross-registration of neurons in a mouse from sessions 7 days and 5 hours apart. Red cross indicates matched cells. Cross-registration criteria: spatial correlation = 0.9 and centroid distance = 4 pixels.

(e) Representational drift over a week: Mice were exposed to the same context (AAA) five hours or seven days apart. RSC neuronal ensembles display greater overlap when mice experience the same context 5 hours vs 7 days apart. (n = 12 mice per group; paired t-test, $t = 3.7$, $p < 0.005$). Data represent mean ± s.e.m.

(f) Neuronal ensemble stability over a week: Mice were exposed to two different (AB) or the same context (CC) seven days apart. All context presentations were counterbalanced. RSC neuronal ensembles display greater overlap when mice experience the same context 7 days apart vs distinct contexts. (n = 11 mice per group, paired t-test, $t = 4.07$, $p < 0.01$). Data represent mean ± s.e.m. and each data point.

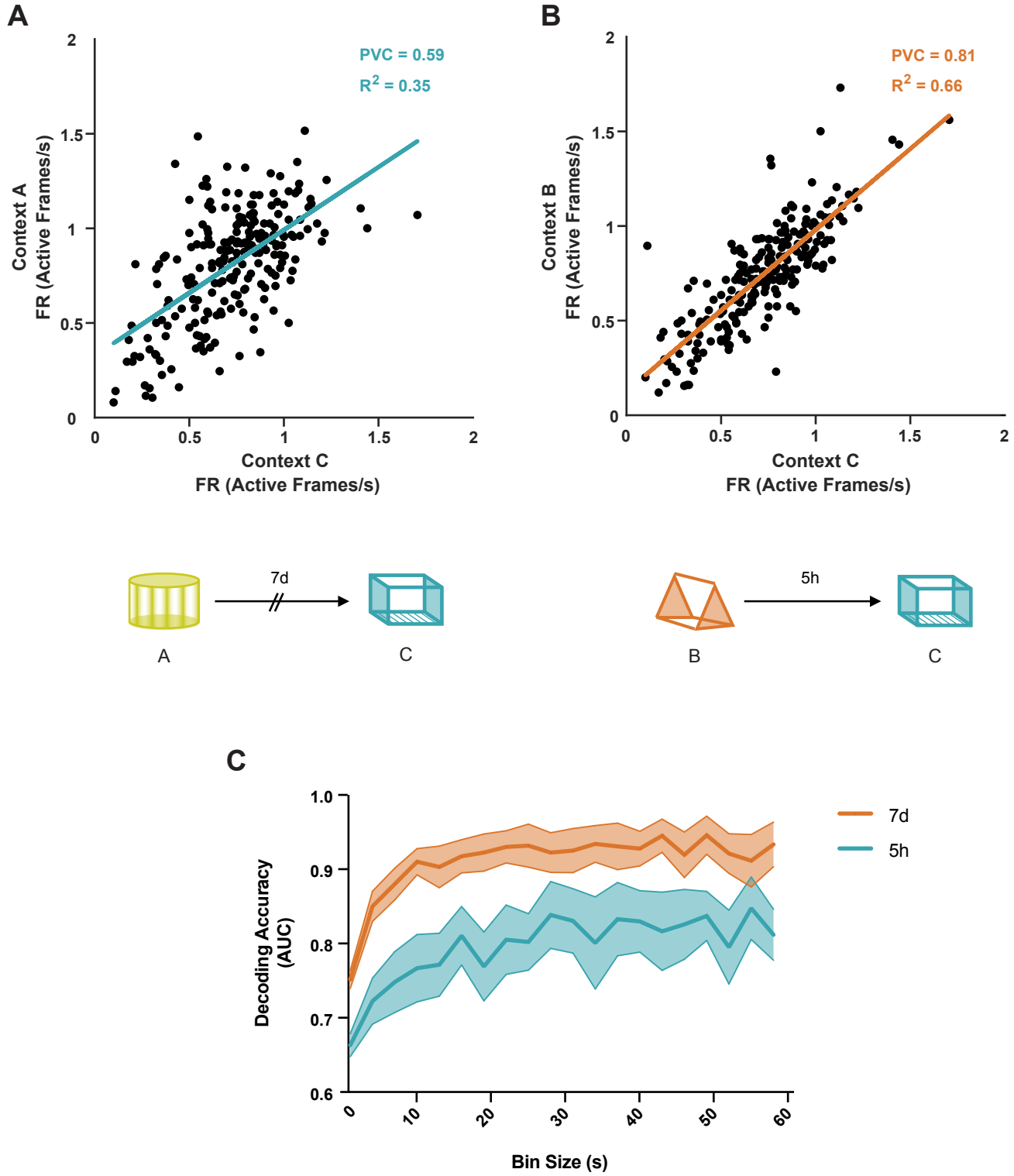
A
PVC = 0.59
R^2 = 0.35
Context A
FR (Active Frames/s)
Context C
FR (Active Frames/s)
B
PVC = 0.81
R^2 = 0.66
Context B
FR (Active Frames/s)
Context C
FR (Active Frames/s)
7d
A
C
5h
B
C
C
Decoding Accuracy
(AUC)
Bin Size (s)
7d
5h

Figure S2

Figure S2. Neuronal activity is more correlated when two contexts are explored closer in time.

(a, b) Scatter plot of the firing rate of all neurons from one mouse in context A (a, 7 days apart) and context B (b, 5 hours apart) as a function of firing rate in context C highlights that neuronal firing rate is maintained when two contexts are explored close in time. Lines represent least-squares linear regression.

(c) Naïve Bayes (NB) classifier is more accurate at distinguishing imaging sessions recorded 7 days vs 5 hours apart irrespective of bin size. AUC (area under the curve) for the binary NB classification between sessions recorded 7 days (7d) apart or 5 hours (5h) apart using neuronal activity indicates that neuronal activity can be used to distinguish between contexts explored 7 days apart more accurately than contexts explored 5 hours apart. Spike probabilities were binned for non-overlapping intervals ranging from 0.5 to 60 seconds (step size 0.5s; Two-way Repeated Measures ANOVA for AUC by bin size; $F_{Group}(1, 16) = 6.2$, $p < 0.05$, n = 9 mice per group). Data represent mean ± s.e.m. Chance Levels performance of the AUC = 0.5.

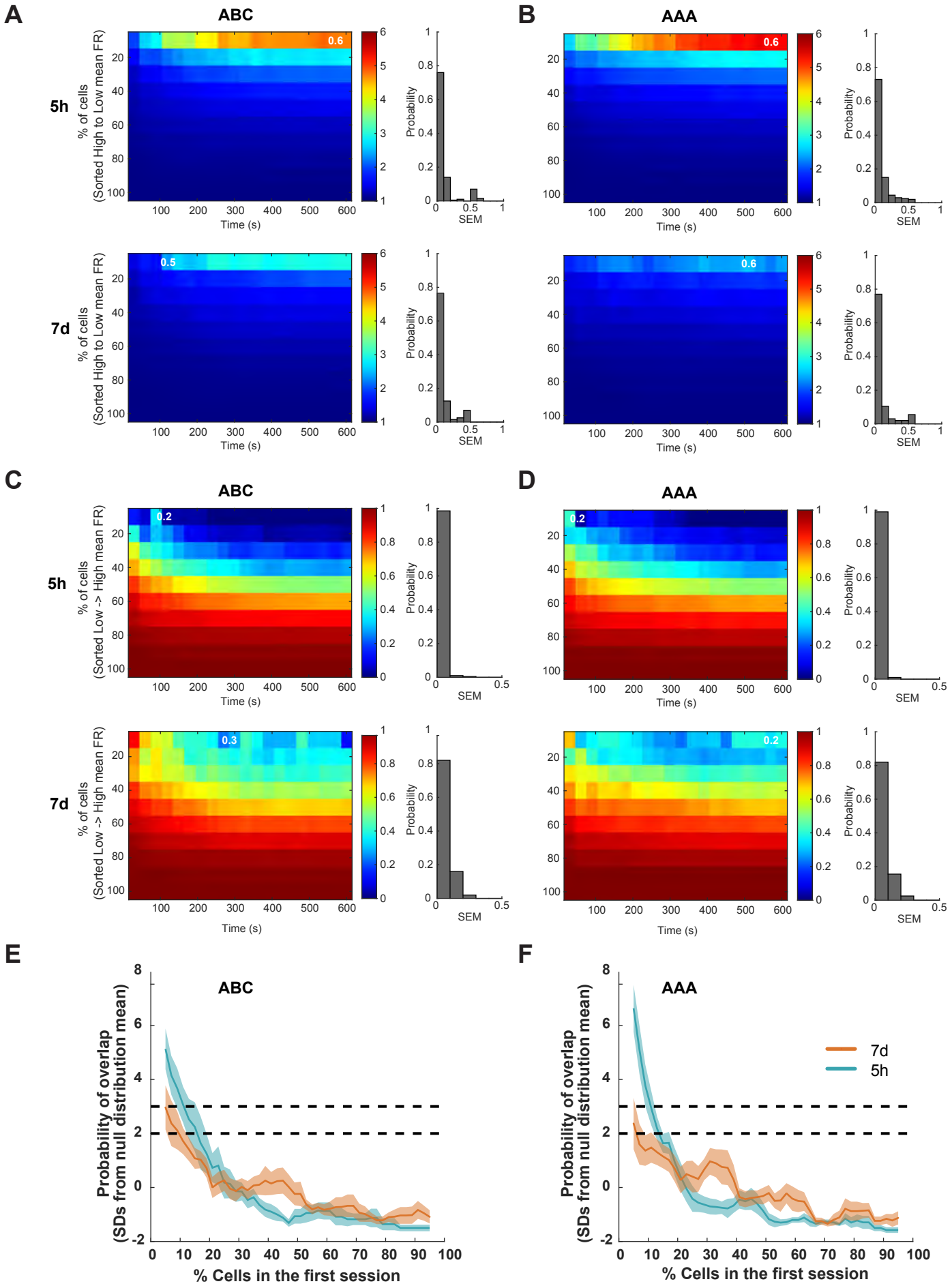
A
ABC
B
AAA
5h
7d
% of cells
(Sorted High to Low mean FR)
Time (s)
Probability
SEM
0.6
0.5
C
D
(Sorted Low -> High mean FR)
0.2
0.3
E
F
Probability of overlap
(SDs from null distribution mean)
% Cells in the first session
7d
5h

Figure S3

Figure S3. Neuronal activity is correlated with the probability of neuronal overlap.

(a) The top 10% high-activity cells in context B are very likely to be the top 10% high activity cells in context C 5h later. Probability of overlap between high activity cells in context A (7d) or context B (5h) and high activity cells in context C. Left: Probability of overlap between subsets of cells with different levels of activity during previous context exploration session (A or B) across time in C. Color bars refer to normalized probabilities (chance = 1). Cumulative values were used for x and y axis (e.g., for x-axis, 300s means 0–300 s; for y-axis, 40 refers to the neurons within the top 40% of high activity). Values represent average across mice. Right: the distribution of SEM across mice for the figures on the left. Numbers (in the probability of overlap figures) represent the maximum SEM from each plot.

(b) Similar to figure (a) but comparisons are performed between the same context experienced 5 hours or 7 days apart.

(c,d) Similar to figures (a) and (b) respectively but the probability of overlap between low activity cells in contexts experienced 7 days or 5 hours before and high activity cells in the third context is presented under ABC (c) and AAA (d) conditions.

(e) Cells were sorted from high to low activity in contexts A or B with a 10% sliding window and 2% steps. Plots show the probability of overlap between subsets of cells (10% ensemble size) from context A (7d) or B (5h) and the top 10% high FR cells from context C. The probability values were z-scored with respect to a null distribution created by randomly subsampling 10% of cells from contexts A or B 10,000x (i.e., results are represented as standard deviation (SD) from the mean of the null distribution). The 2SD and 3SD thresholds are labeled with a dashed line.

(f) Same comparison as (e) but for the AAA condition. (ABC: n = 9, AAA: n = 9 mice).

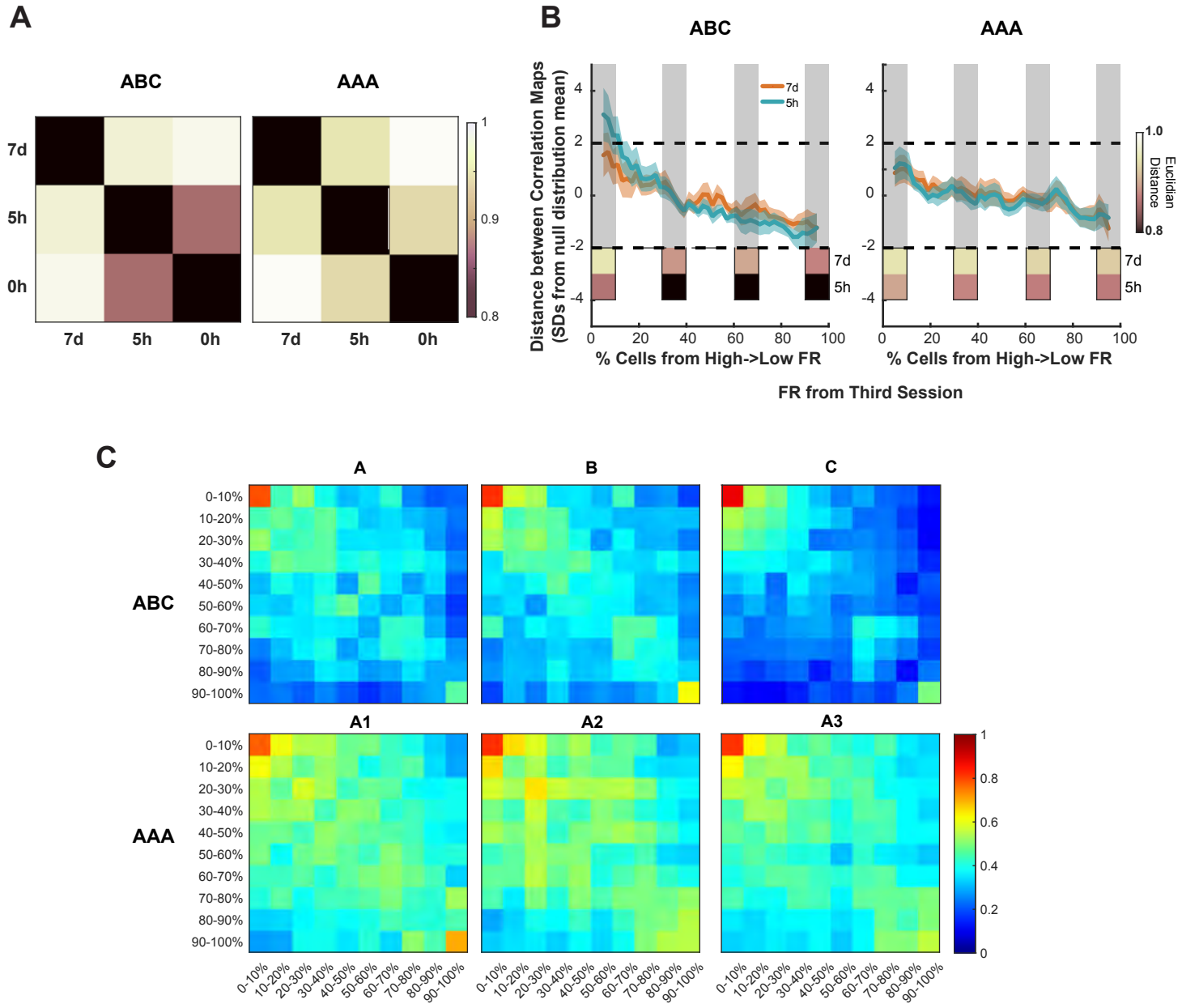
A
ABC
AAA
7d
5h
0h
1
0.9
0.8
B
ABC
AAA
Distance between Correlation Maps (SDs from null distribution mean)
% Cells from High->Low FR
FR from Third Session
Euclidian Distance
1.0
0.8
C
A
B
C
A1
A2
A3
ABC
AAA
0-10%
10-20%
20-30%
30-40%
40-50%
50-60%
60-70%
70-80%
80-90%
90-100%

Figure S4

Figure S4. High and low firing rate neurons make differential contributions to representational similarity to regulate memory linking and discrimination.

(a) Euclidean distance between correlation maps from different sessions. For each animal, the Euclidean distance was calculated for all possible combinations to create a Euclidean distance map. For each map, all the distances were normalized by the maximum distance. Normalized Euclidean distance maps were then averaged across animals to produce the plots (ABC, right, n = 9; AAA, left, n = 9). Note that the Euclidean distance between correlation maps in the 5h interval is lower than for the 7d interval for the ABC (right) or the AAA (left) contexts conditions.

(b) Cells were sorted from high to low activity in context C (x-axis) with a 10% sliding window and 2% steps. Correlation maps were calculated by excluding 10% of cells belonging to each of these sliding windows and the Euclidean distance (y-axis) between contexts explored 7d or 5h apart under ABC (right) or AAA (left) condition was calculated. The Euclidean distance values were normalized with respect to a null distribution created by randomly subsampling 10% of cells from context C 10,000x (i.e., results are represented as standard deviation (SD) from the mean of the null distribution). The 2SD threshold is labeled with a dashed line. Plots on the bottom of each image show the average Euclidean Distance across animals for the 7d and 5h intervals when the following groups of cells are excluded: 0-10%, 30-40%, 60-70%, and 90-100%. Note that the Euclidean distance for the 5h interval is always lower than for the 7d interval. For AAA condition, the exclusion of any batch of 10% cells does not significantly affect the Euclidean distance. However, for the 5h interval in ABC condition, the top 10% FR cells, when excluded, significantly change the Euclidean Distance. Therefore, the top 10% FR cells are critical for the similarity between correlation maps when different contexts are explored but the contribution of these top 10% FR cells is not significant when the same context is explored at the same time intervals.

(c) Plots show the average normalized correlation maps across animals during the exploration of contexts in ABC (top) or AAA (bottom) conditions. For each animal, cells were sorted from high to low firing rate (based on the last context exploration). The neuronal population was then split into 10% non-overlapping groups. Average Pearson correlation between groups was calculated. A correlation map of the average correlation between groups was constructed and normalized to the maximum value of average correlation for each animal. Plots show the average of these normalized correlation maps across all animals. For all conditions and sessions, the top FR cells have the highest correlation values. Importantly, for the AAA condition, all correlation maps are quite similar despite the session. However, for the ABC condition, the maps show larger differences and the similarity between correlation values between contexts B and C, which are 5h apart, seem to be higher for the high FR cells, as shown previously.

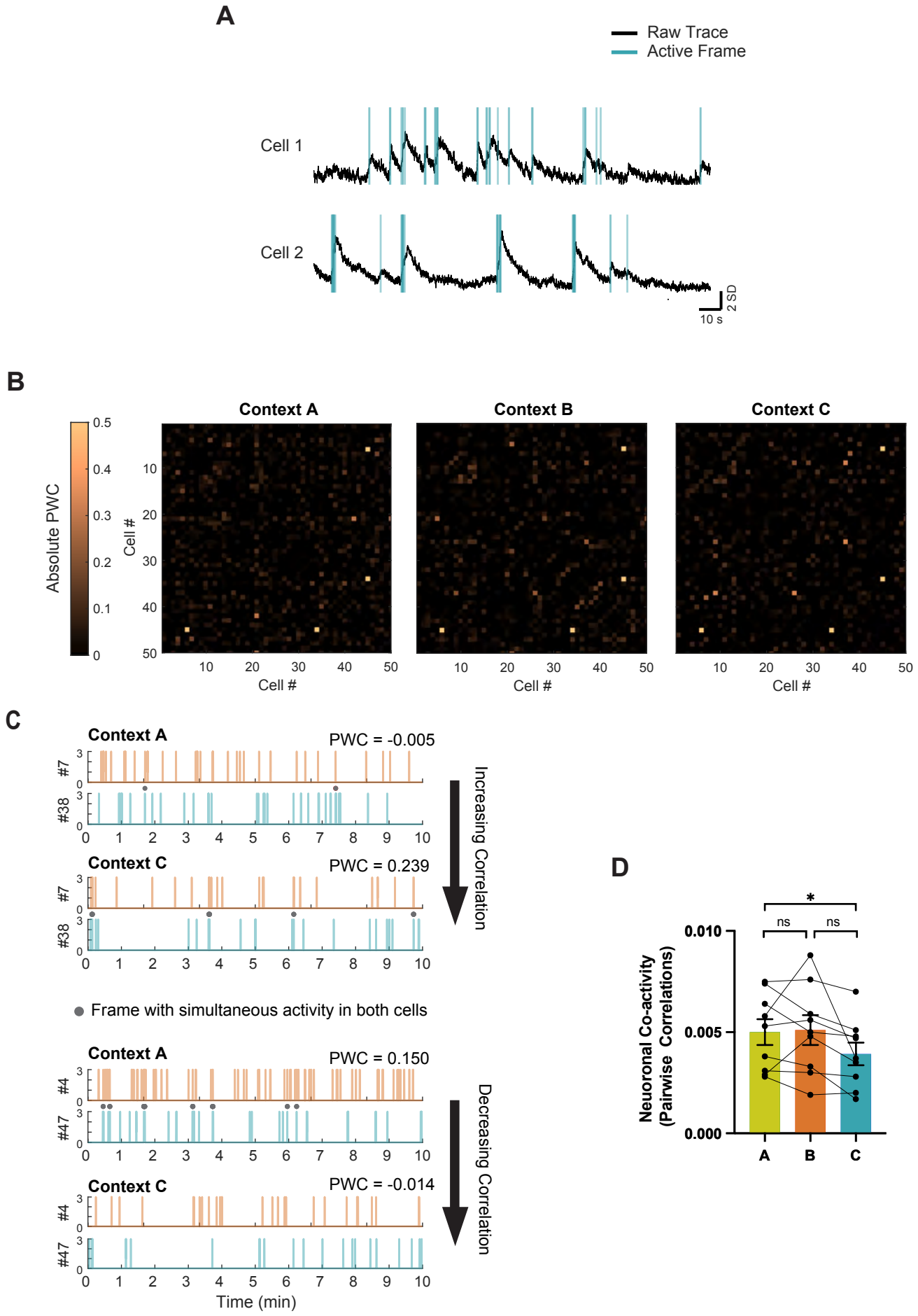
A
Raw Trace
Active Frame
Cell 1
Cell 2
2 SD
10 s
B
Context A
Context B
Context C
Absolute PWC
Cell #
C
Context A
PWC = -0.005
#7
#38
Context C
PWC = 0.239
Increasing Correlation
Frame with simultaneous activity in both cells
Context A
PWC = 0.150
#4
#47
Context C
PWC = -0.014
Decreasing Correlation
Time (min)
D
Neuoronal Co-activity (Pairwise Correlations)
ns
ns
*
A
B
C

Figure S5

1086 **Figure S5. Coactivity among RSC neurons during multiple contextual exposures**

1087 (a) Example of two co-active neurons: For each imaging session, deconvolved neuronal activity
1088 was binned into 100ms periods, and the Pairwise correlation (PWC: Pearson correlation of the
1089 number of active frames) for each neuron pair was calculated. Black: raw calcium trace and Blue:
1090 frames identified as active following deconvolution of the calcium trace.

1091 (b) Pairwise Correlation (PWC) map for each context for 50 cell pairs from one mouse. Absolute
1092 Pearson's correlation coefficients were plotted.

1093 (c) Top Panel: Example of a neuronal pair with increasing PWC between imaging sessions: Cell
1094 pair (7 and 38: arbitrary cell IDs) display more coactivity (number of simultaneous active frames)
1095 during Context C exploration than Context A exploration. Bottom Panel: Example of a neuronal
1096 pair with decreasing PWC between imaging sessions: Cell pair (4 and 47: arbitrary cell IDs)
1097 display less coactivity during Context C exploration than Context A exploration.

1098 (d) Average PWCs across the three context exposures display a small decrease (One-way
1099 repeated measure ANOVA; $F(1.6, 12.9) = 4.05$, $p = 0.05$; Tukey's post-hoc test, n = 9 mice per
1100 group). Data represent mean ± s.e.m. and each data point, * $p < 0.05$.

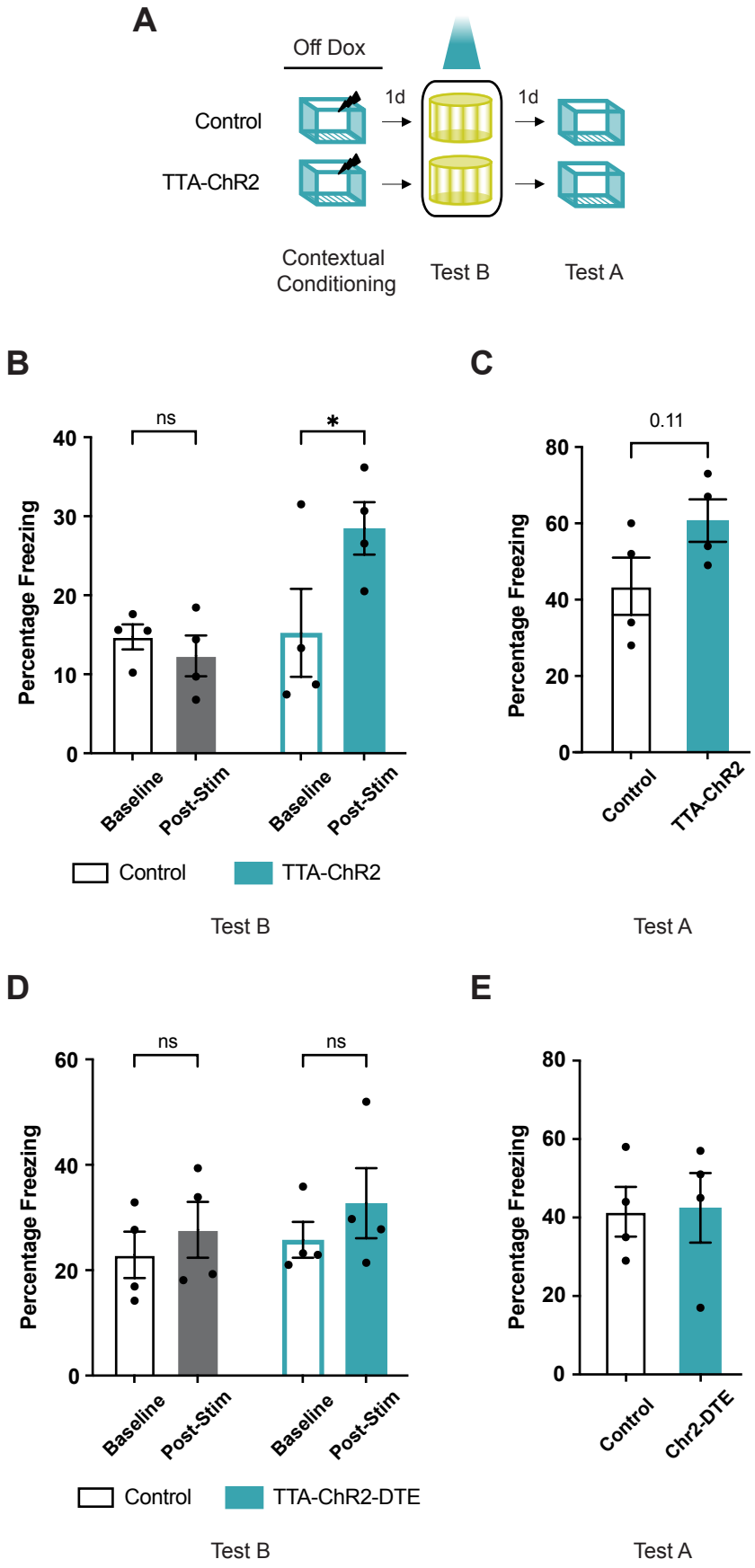
A
Off Dox
Control
TTA-ChR2
1d
1d
Contextual Conditioning
Test B
Test A
B
ns
*
Percentage Freezing
Baseline
Post-Stim
Baseline
Post-Stim
Control
TTA-ChR2
Test B
C
0.11
Percentage Freezing
Control
TTA-ChR2
Test A
D
ns
ns
Percentage Freezing
Baseline
Post-Stim
Baseline
Post-Stim
Control
TTA-ChR2-DTE
Test B
E
Percentage Freezing
Control
Chr2-DTE
Test A

Figure S6

1101 **Figure S6. RSC neuronal ensemble (and not dendritic ensemble reactivation) following**
1102 **contextual fear conditioning results in fear expression**

1103 **(**a) Experimental setup: cFos-tTa (TTA-Chr2) mice and their wildtype littermates (Control)
1104 underwent bilateral viral injections (TRE-ChR2-mCherry) and optic cannula implants. Mice were
1105 taken off doxycycline chow (three days before contextual fear conditioning in context A: 2
1106 footshocks, 2s, 0.7mA) to allow c-fos promoter-driven tTA and Channelrhodopsin (ChR2)
1107 expression. Following contextual fear conditioning, mice were tested in a novel context (Test B)
1108 while the previously tagged neurons were activated. The following day mice were retested without
1109 any optogenetic manipulation in the training context (Test A).

1110 (b) During Test B, freezing during the two post-stimulation conditions (with laser and without laser
1111 stimulation) was not different. Therefore, freezing during this period is presented together as post-
1112 stimulation freezing (Two-way RM ANOVA, group X time interaction, $F(1, 6) = 11.93$, $p < 0.01$,
1113 Sidak's post hoc tests).

1114 (c) During Test A, the TTA-Chr2 mice display comparable freezing to the control mice ($t=1.85$,
1115 $df=6$, $p = 0.11$).

1116 (d) Reactivation of previously activated dendrites is not sufficient for fear memory expression:
1117 Experimental set up is the same as (a), but animals were injected with TRE-hChR2-mCherry-DTE
1118 or TRE-mCherry-DTE virus in the RSC to reactivate dendritic segments active during contextual
1119 fear conditioning. Both groups display similar freezing during baseline and post-stimulation
1120 epochs while testing in a novel context (Two-way RM ANOVA, group X time interaction, $F(1, 6)$
1121 $= 0.26$, $p = 0.6$, Sidak's post hoc tests).

1122 (e) Both groups (injected with TRE-hChR2-mCherry-DTE or TRE-mCherry-DTE virus in the RSC)
1123 display similar freezing during test in Context A ($t=0.09$, $df=6$, $p = 0.9$).

1124 Data represent mean ± s.e.m. and each data point, * $p < 0.05$, ns = not significant.

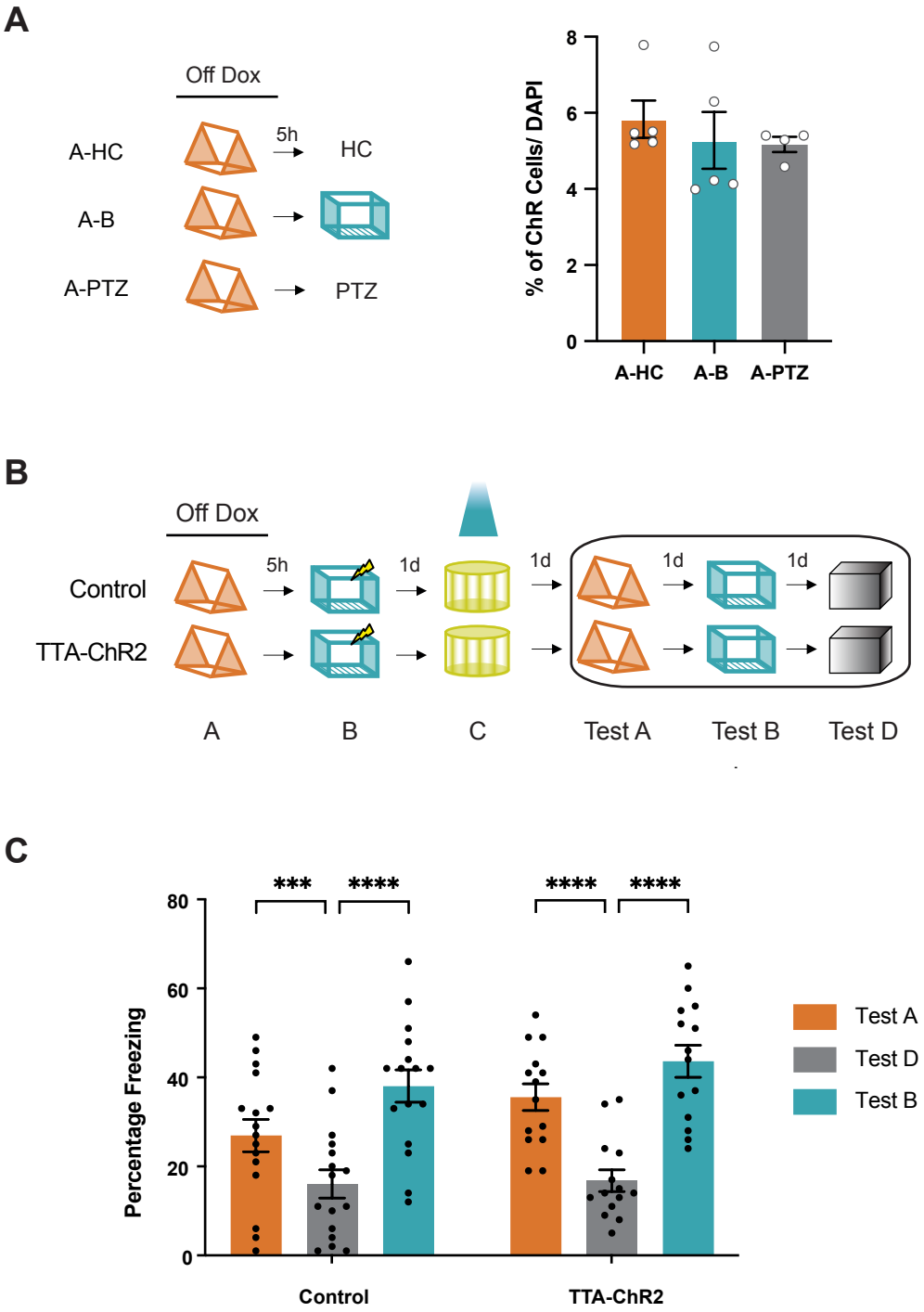
A
Off Dox
A-HC
A-B
A-PTZ
5h
HC
PTZ
% of ChR Cells/ DAPI
8
6
4
2
0
A-HC
A-B
A-PTZ
B
Off Dox
Control
TTA-ChR2
5h
1d
1d
1d
1d
A
B
C
Test A
Test B
Test D
C
***
****
****
****
80
60
40
20
0
Percentage Freezing
Control
TTA-ChR2
Test A
Test D
Test B

Figure S7

Figure S7. Fear expression due to reactivation of the linked memory ensemble is not driven by changes in the strength of memory linking or tagging of cells outside of the first behavioral episode.

(a) Five hours after context exposure, the tagging window is closed by doxycycline. RSC ensemble activated during the exploration of the first context (context A) was tagged. The tagging window was closed by placing the mice on a high concentration of doxycycline chow (200mg/kg) as well as a doxycycline injection (i.p., 50 µg/ gram of body weight) two hours post exposure to context A. Five hours following the context exposure mice were either left in home cage (A-HC), explored another context (A-B) or received an injection of pentylenetetrazole (PTZ, 30mg/kg, A-PTZ). Animals were perfused and brains collected 24 hours post-tagging (same timepoint as optogenetic activation for experiment in Figure 2d). No differences in Channelrhodopsin/mCherry expression were observed between groups (One-way ANOVA, $F(2, 11) = 0.4$, $p = 0.7$; Dunnett's multiple comparisons test, ns).

(b) Following optogenetic activation of the first memory ensemble (Figure 2d), mice were tested in the linked context (Context A), shock context (Context B), and in another novel context.

(c) Both groups of mice display robust memory linking, such that the freezing in both context A (linked) and context B (shock) is higher than freezing in a novel context (Two-way RM ANOVA, $F_{time}(1.9, 54) = 86.9$, $p < 0.0001$; Dunnett's multiple comparisons test).

Data represent mean ± s.e.m. and each data point, *** $p < 0.001$, **** $p < 0.0001$.

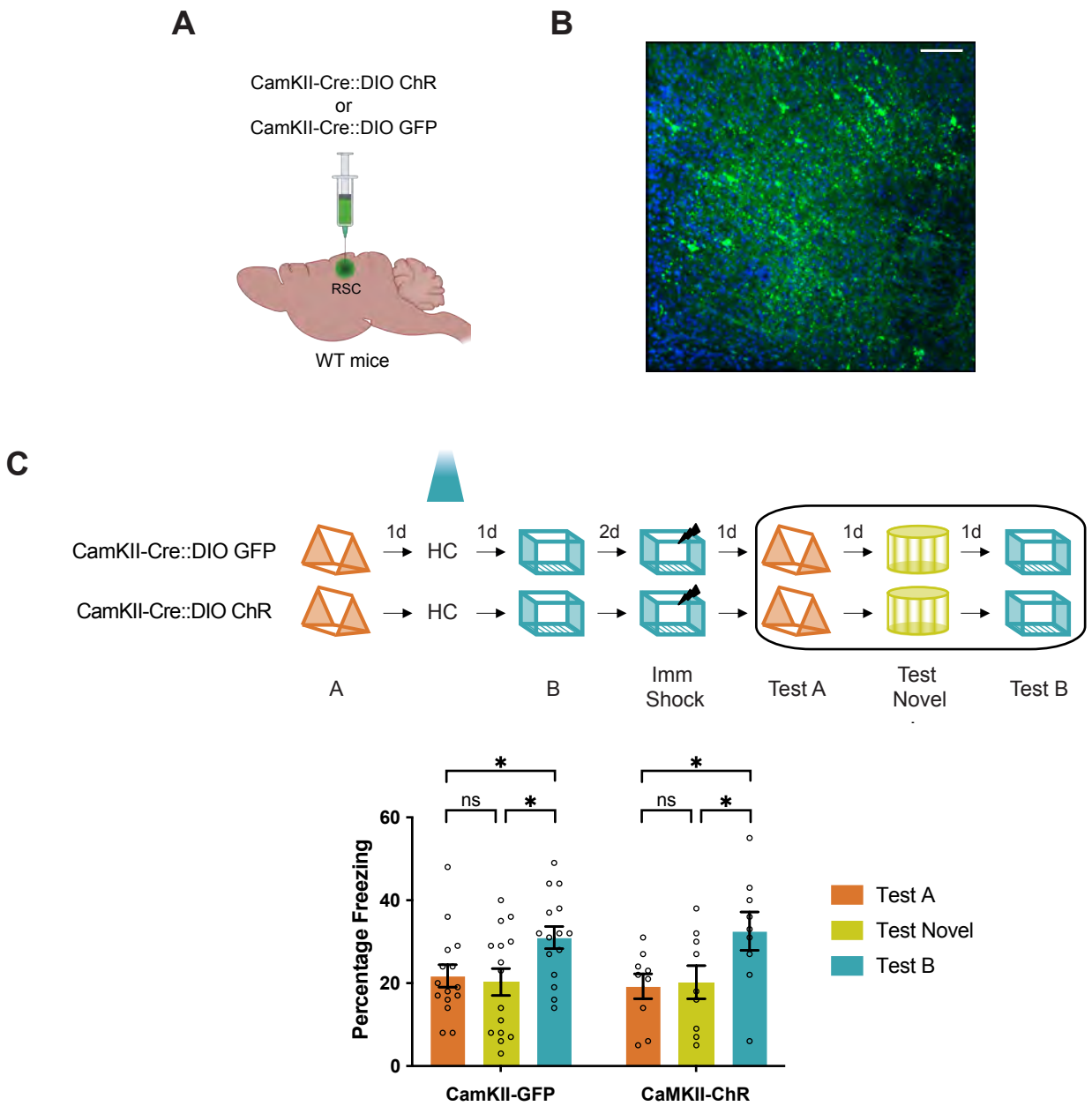
A
CamKII-Cre::DIO ChR
or
CamKII-Cre::DIO GFP
RSC
WT mice
B
C
CamKII-Cre::DIO GFP
CamKII-Cre::DIO ChR
1d
HC
2d
A
B
Imm
Shock
Test A
Test
Novel
Test B
Percentage Freezing
60
40
20
0
ns
*
CamKII-GFP
CaMKII-ChR
Test A
Test Novel
Test B

Figure S8

1147 **Figure S8. Optogenetic activation of a randomly labeled ensemble does not result in**
1148 **memory linking.**

1149 (a) Mice received a bilateral injection CamKII-Cre::DIO-ChR or CamKII-Cre::DIO-GFP to label a
1150 small subset of RSC ensemble.
1151
1152 (b) Representative image of WT mice injected with CamKII-Cre::DIO-ChR-GFP in the RSC.
1153 Scale: 20 μm
1154
1155 (c) Control (CamKII-Cre::DIO-GFP) as well as experimental (CamKII-Cre::DIO-ChR) mice display
1156 low levels of freezing in a novel as well as the previously explored neutral (Context A) context but
1157 freeze more in the training context (Context B). (Two-way RM ANOVA, F_{time} (1.9, 42.4) = 9.8, P <
1158 0.0005, Tukey's multiple comparisons test).
1159
1160 Data represent mean ± s.e.m. and each data point, * $p < 0.05$.
1161

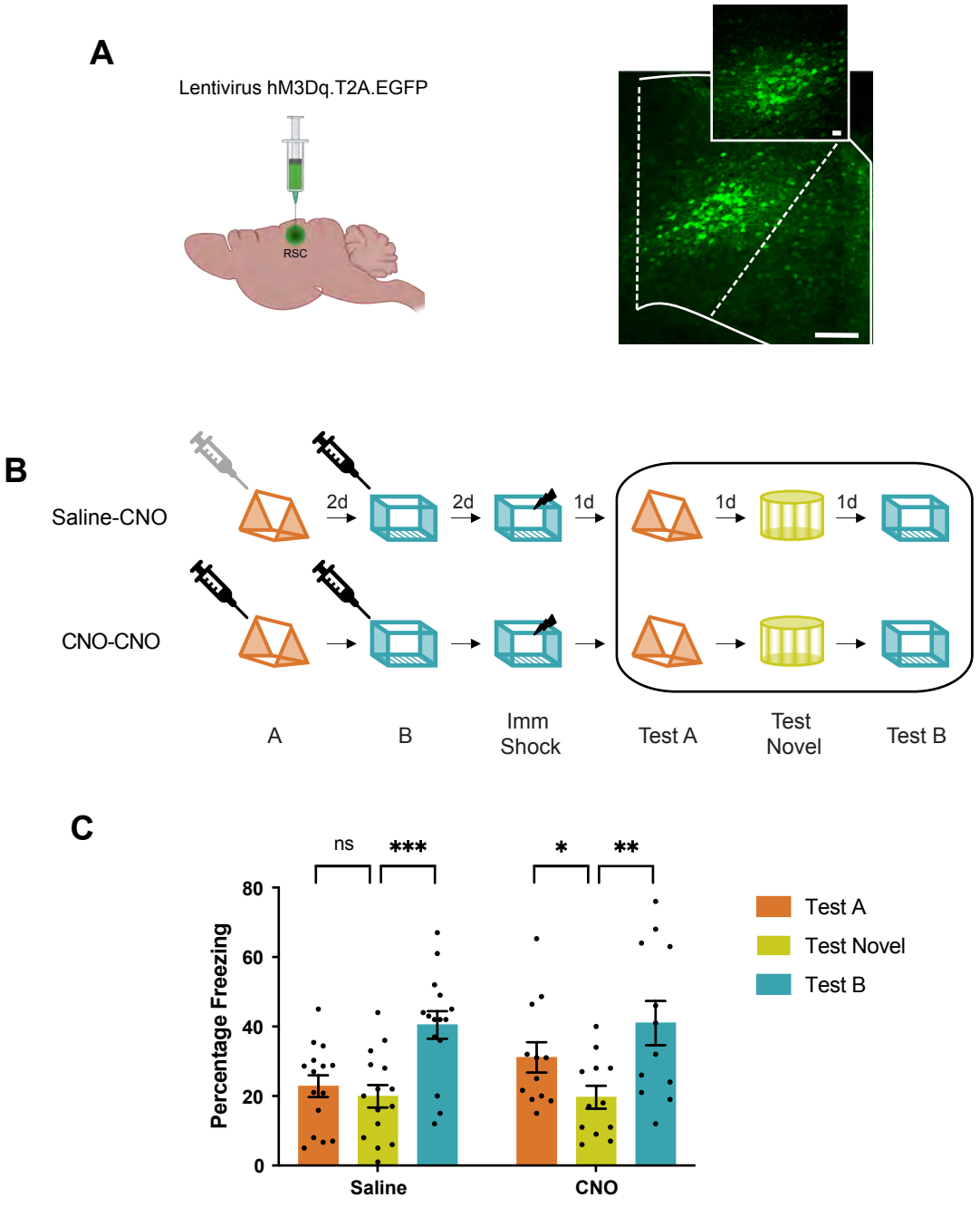
A
Lentivirus hM3Dq.T2A.EGFP
RSC
B
Saline-CNO
CNO-CNO
2d
2d
1d
1d
1d
A
B
Imm Shock
Test A
Test Novel
Test B
C
ns
***
*
**
Percentage Freezing
80
60
40
20
0
Saline
CNO
Test A
Test Novel
Test B

Figure S9

Figure S9. Chemogenetic manipulation of the neuronal ensemble overlap is sufficient to link two distinct contextual memories

(a) All mice received a bilateral injection of lentivirus DREADD hM3Dq-T2A-EGFP which infects a sparse population of RSC neurons. Representative images demonstrating hM3Dq-T2A-EGFP infection of RSC neurons from two mice on the left. Scale: 100 and 20 μm.

(b) All mice explored two different contexts 2 days apart and were subsequently shocked in one of these contexts. Neuronal excitability was increased in a small subset of RSC neurons by administering a CNO (0.5mg/kg) injection 45 mins before each context exploration. The control mice only received the CNO injection before the second context exploration.

(c) Control mice display low levels of freezing in a novel as well as the previously explored neutral (Context A) context but freeze more in the training context (Context B). In contrast, mice from the experimental group display memory linking: Both the previously explored contexts (Context A and B) elicit high freezing relative to the freezing in a novel context. (Two-way RM ANOVA, F_{time} (1.8, 44.9) = 28.45, P < 0.0001, Dunnett's multiple comparisons test).

The physical contexts presented were counterbalanced to minimize any effect of context similarity. Data represent mean ± s.e.m. and each data point, * $p < 0.05$, ** $p < 0.01$, *** $p < 0.001$.

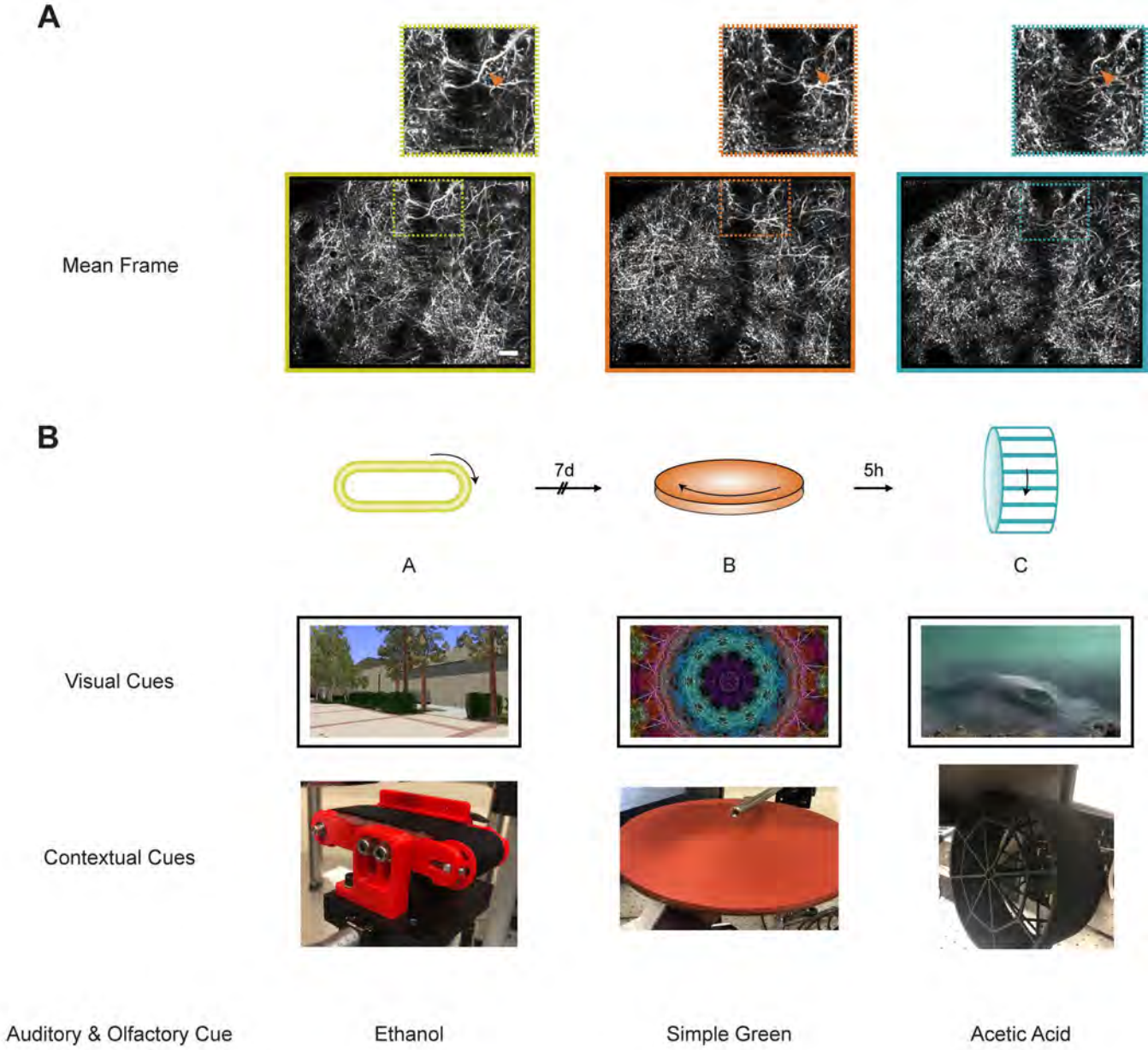
A
Mean Frame
B
7d
5h
A
B
C
Visual Cues
Contextual Cues
Auditory & Olfactory Cue
Ethanol
Simple Green
Acetic Acid

Figure S10

Figure S10. Experimental setup for functional dendritic co-allocation studies:

(a) Bottom: Example maximum projection images from three imaging sessions from a mouse. Scale: 20 μm. Top: Inset demonstrates boxed region from each image below magnified to depict the same dendritic segment across sessions.

(b) Schematics of 3 distinct contexts (different auditory, visual, and olfactory cues as well as running apparatus) used in the head-fixed experiments. Mice were exposed to 3 distinct contexts 7 days or 5 hours apart in a counterbalanced manner while RSC dendritic transients were imaged.

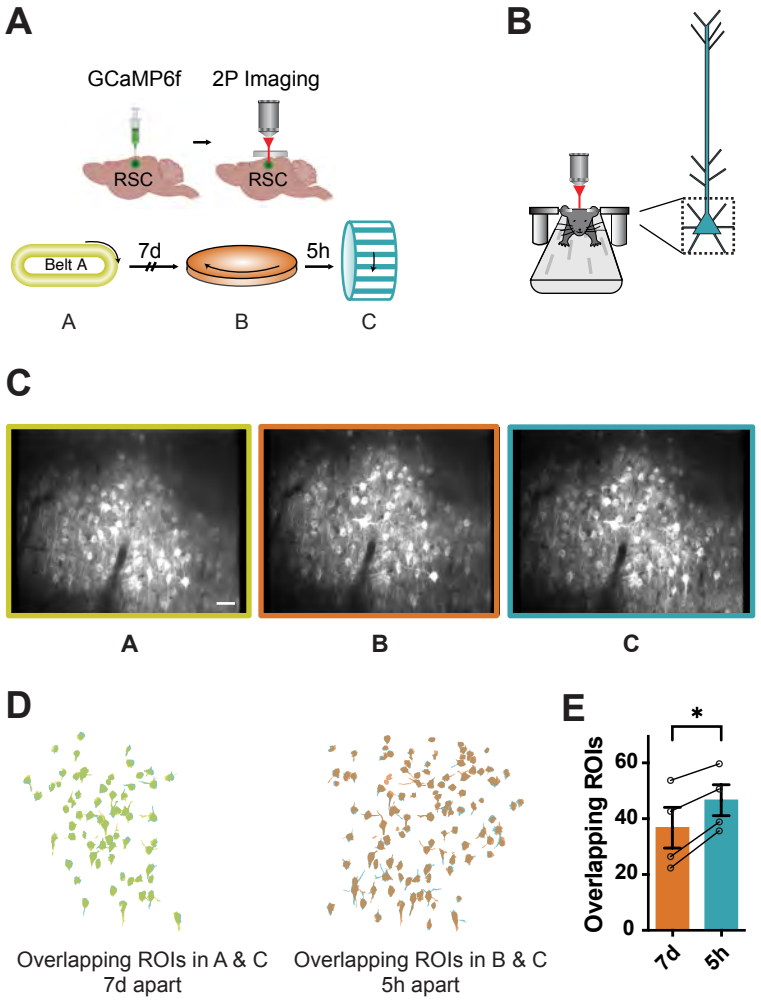
A
GCaMP6f
2P Imaging
RSC
RSC
Belt A
7d
5h
A
B
C
B
C
A
B
C
D
Overlapping ROIs in A & C
7d apart
Overlapping ROIs in B & C
5h apart
E
*
Overlapping ROIs
60
40
20
0
7d
5h

Figure S11

Figure S11. Overlapping neuronal ensemble encodes contexts experienced close in time in head-fixed mice.

(a, b) Experimental setup: Head-fixed mice experienced three distinct contexts either 7 days or 5 hours apart while calcium transients from layer V RSC neurons were imaged.

(c) Mean frames from three imaging sessions from a mouse. Scale: 40 μm.

(d) Overlapping neuronal ROIs reactivated when contexts are separated by 7 days (left) or 5 hours (right) from one mouse.

(e) The same neuronal ensemble is more likely to be activated in a head-fixed setting when context exposures are 5 hours (5h) apart vs 7 days (7d) apart. (Paired t-test; t = 5.6; p = 0.01; n=4 mice).

Data represent mean ± s.e.m. and each data point.

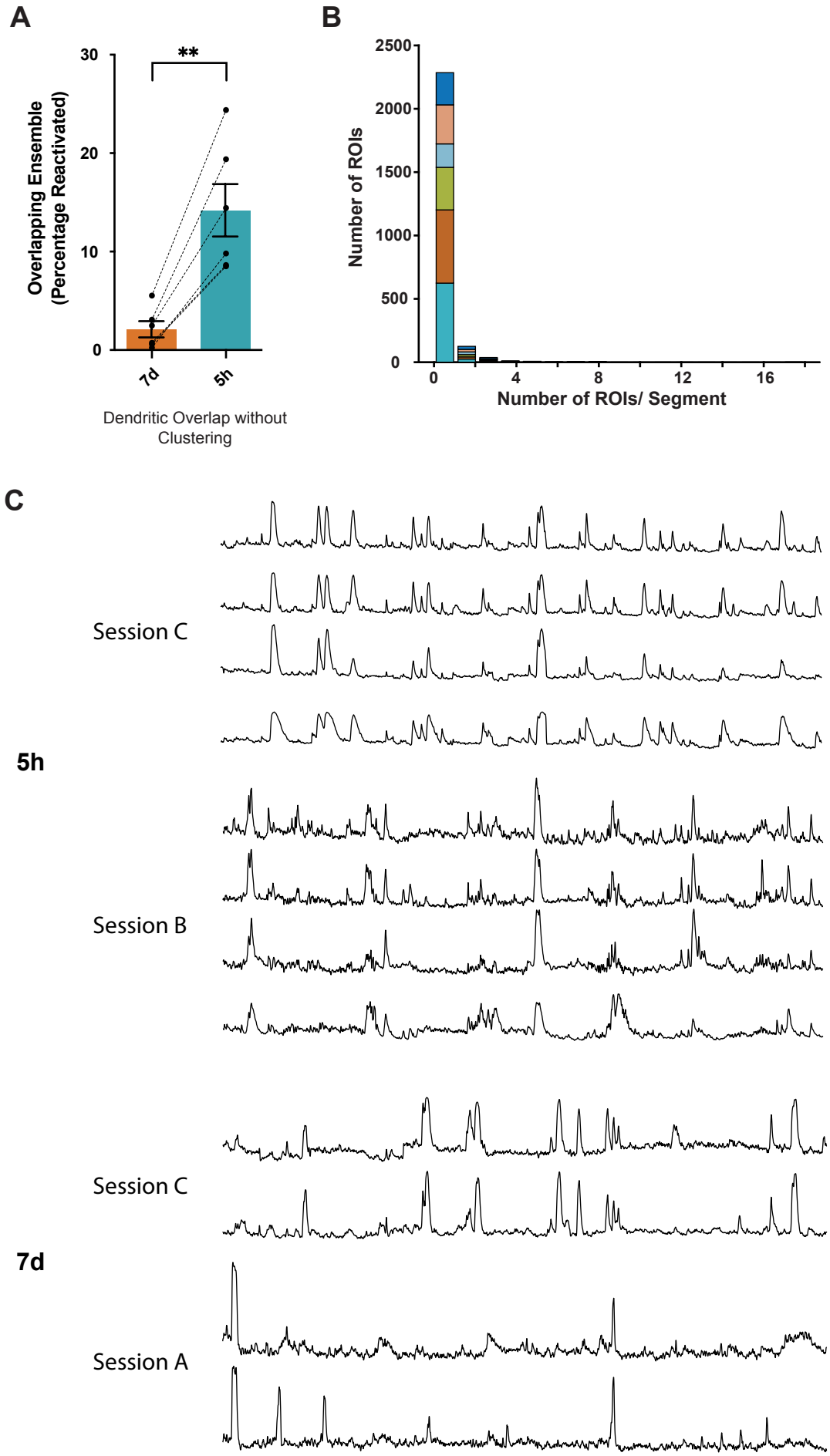
A
B
C
**
Overlapping Ensemble (Percentage Reactivated)
30
20
10
0
7d
5h
Dendritic Overlap without Clustering
Number of ROIs
2500
2000
1500
1000
500
0
0
4
8
12
16
Number of ROIs/ Segment
5h
Session C
Session B
7d
Session C
Session A

Figure S12

Figure S12. Differences in dendritic overlap are not driven by correlated activity within dendritic branches.

(a) Dendritic overlap is higher when context exposures are 5 hours (5h) apart vs 7 days (7d) apart when dendritic ROIs are not clustered together based on correlated activity. (Paired t-test; $t = 6.5$; $p < 0.01$; n=6 mice).

(b) Histogram of the number of ROIs per dendritic segment following clustering (1.15 ± .03 ROIs per cluster). Data from each mouse is depicted in a separate color.

(c) For the reactivated dendritic segments (i.e., the clustered ROIs within reactivated segments), ROIs clustered based on their activity in session C (reference session) display high within-cluster correlated activity across sessions. Traces represent z-score of calcium transients. Scale: 30s.

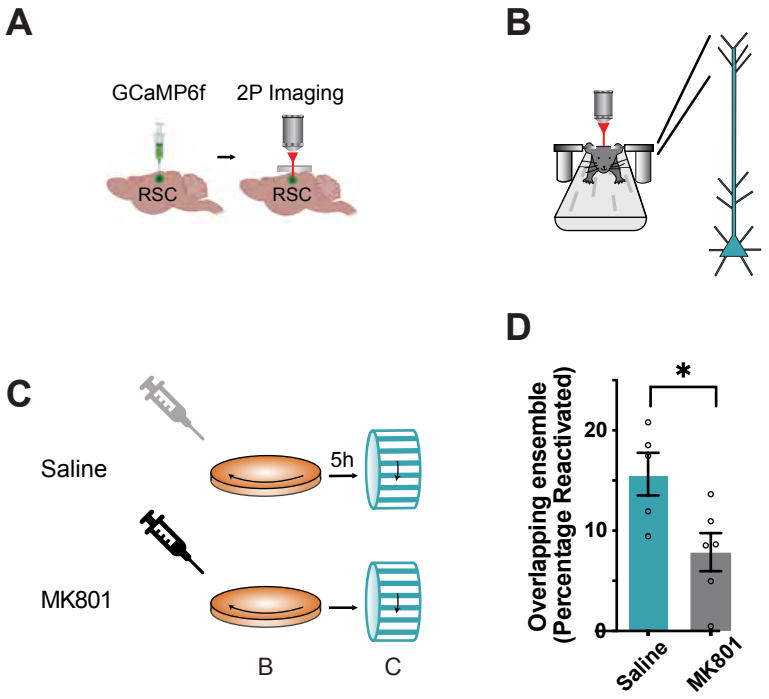
A
GCaMP6f
2P Imaging
RSC
RSC
B
C
Saline
5h
MK801
B
C
D
Overlapping ensemble
(Percentage Reactivated)
*
20
10
0
Saline
MK801

Figure S13

Figure S13. NMDA receptor activation is required for the reactivation of dendritic ensembles.

(a-c) Dendritic overlap was measured as described in Figure 3. Mice were administered NMDA receptor antagonist, MK801, 30 minutes prior to the first context exposure.

(d) NMDA receptor antagonist, MK801, impairs reactivation of dendritic ensembles following two context exposures 5 hours (5h) apart. (Paired t-test; $t = 9.2$; $p < 0.0005$; n=6 mice each).

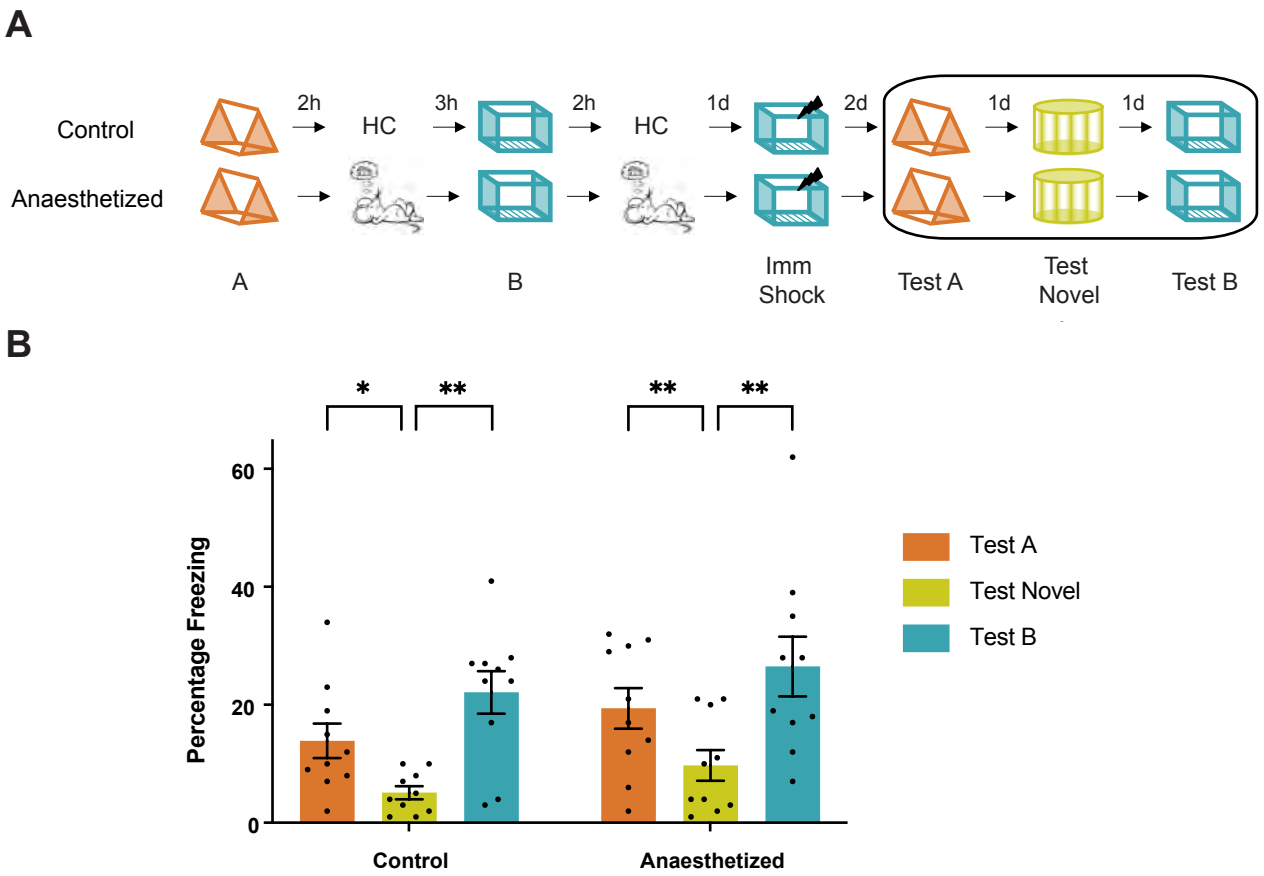
A
Control
Anaesthetized
2h
HC
3h
2h
HC
1d
2d
1d
1d
A
B
Imm
Shock
Test A
Test
Novel
Test B
B
*
**
**
**
Percentage Freezing
60
40
20
0
Control
Anaesthetized
Test A
Test Novel
Test B

Figure S14

Figure S14. Memories of contexts can still be linked under conditions used during structural imaging.

(a) Experimental setup: All mice were handled and habituated in a manner identical to the imaging experiments in Figure 4. Mice experienced two contexts (A and B) 5 hours apart. Two hours following each context exposure, mice were anesthetized for 40 minutes to mimic anesthesia during the imaging sessions to study spine dynamics.

(b) The anesthetized mice can link the shock context (context B) to a neutral context (context A) 5 hours apart. For both groups of mice, freezing in the linked (context A), as well as training context (context B), is higher than freezing in a novel context. Therefore, prolonged anesthesia on the day of memory linking does not disrupt memory linking. (Two-way RM ANOVA, $F_{context}$ (1.5, 36) = 27.8, P < 0.0001, Dunnett's multiple comparisons test).

Data represent mean± s.e.m. and each data point, * $p < 0.05$, ** $p < 0.01$.

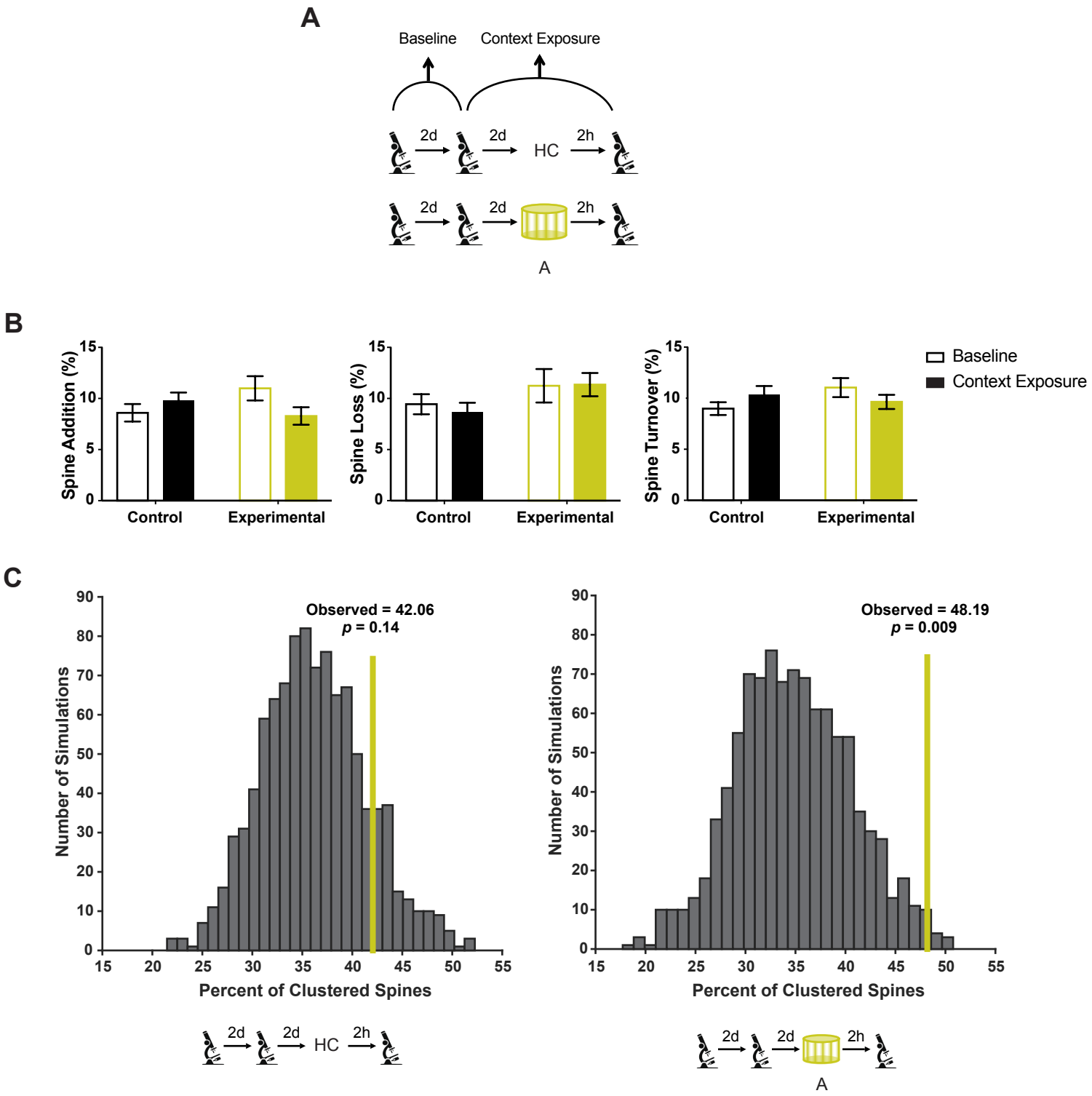
A
Baseline
Context Exposure
2d
2d
HC
2h
2d
2d
2h
A
B
Spine Addition (%)
Spine Loss (%)
Spine Turnover (%)
Control
Experimental
Baseline
Context Exposure
C
Observed = 42.06
p = 0.14
Observed = 48.19
p = 0.009
Number of Simulations
Percent of Clustered Spines
2d
2d
HC
2h
2d
2d
2h
A

Figure S15

1248 **Figure S15. Spine dynamics within the RSC following context exposure**
1249
1250 (a) Thy1-YFP mice were imaged every two days (baseline), and the same RSC dendrites were
1251 tracked to measure contextual exposure-related spine dynamics. Following two baseline imaging
1252 sessions, mice were left in the home cage or exposed to a novel context.
1253
1254 (b) Spine addition, spine loss, and spine turnover is not altered within the RSC apical dendrites
1255 following context exposure (Two-way RM ANOVA; Sidak's post hoc tests)
1256
1257 (c) Clustered spine addition following context exposure is greater than chance: The histogram
1258 shows percent clustering from 1000 simulations of randomized new spine positions, where the
1259 percent of new spines within 5 μm of each other was calculated. Yellow line: Percentage spine
1260 clustering observed from the data. The percentage of clustered spines is more than that expected
1261 by chance for the experimental group (Right, n=6; $p = 0.009$) whereas the percentage of clustered
1262 spines is at chance levels for the control group (Left, n=5; $p = 0.14$). Control: n=44 dendrites (5
1263 mice); Experimental: n=46 dendrites (6 mice).
1264
1265 Data represent mean ± s.e.m.
1266

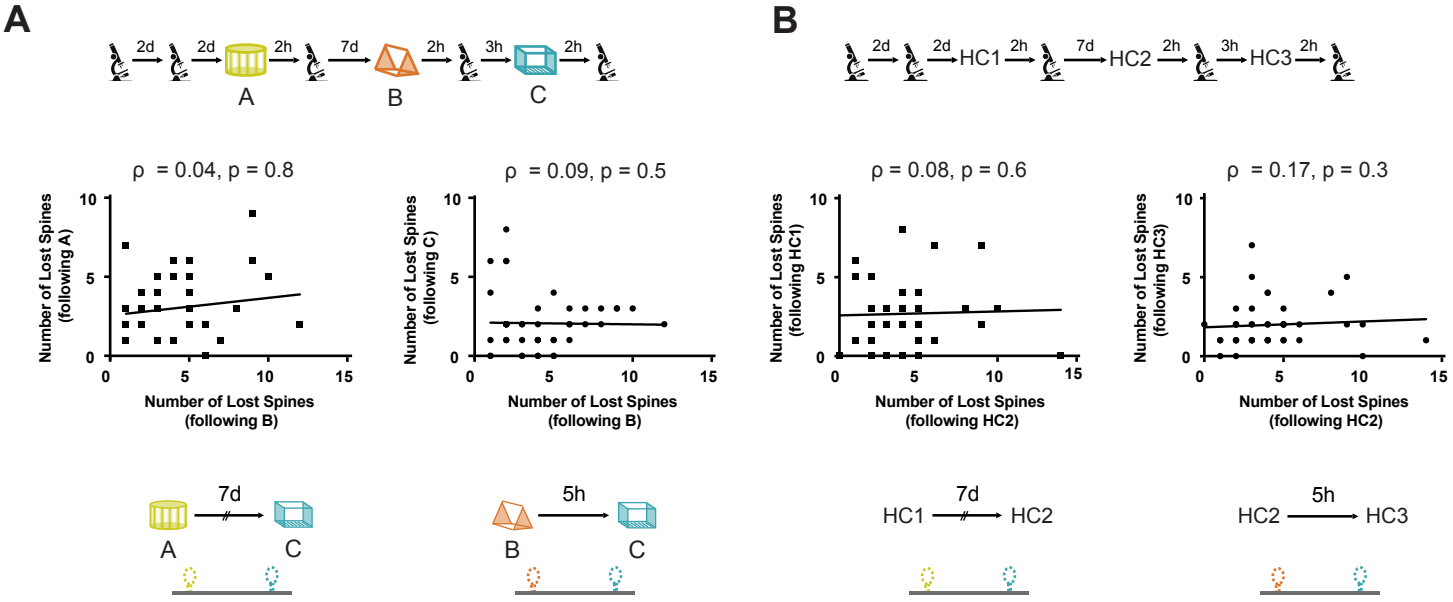
A
2d
2d
2h
7d
2h
3h
2h
A
B
C
ρ = 0.04, p = 0.8
Number of Lost Spines (following A)
Number of Lost Spines (following B)
ρ = 0.09, p = 0.5
Number of Lost Spines (following C)
Number of Lost Spines (following B)
7d
A
C
5h
B
C
B
2d
2d
HC1
2h
7d
HC2
2h
3h
HC3
2h
ρ = 0.08, p = 0.6
Number of Lost Spines (following HC1)
Number of Lost Spines (following HC2)
ρ = 0.17, p = 0.3
Number of Lost Spines (following HC3)
Number of Lost Spines (following HC2)
7d
HC1
HC2
5h
HC2
HC3

Figure S16

1267 **Figure S16. Spine loss during memory linking is not biased to the same dendritic segments**
1268
1269 (a) Left: Number of spines lost from a dendritic segment following Context A and B exposure (7
1270 days apart) are not correlated (ρ = 0.04, p = 0.8). Right: Number of spines lost from a dendritic
1271 segment following Context B and C (5 hours apart) exposure are not correlated (ρ = 0.09, p =
1272 0.5).
1273
1274 (b) For mice left in their home cages (HC), the number of spines lost from a dendritic segment are
1275 not correlated whether imaging sessions are separated by either 7 days (left, ρ = 0.08, p = 0.6)
1276 or 5 hours (right, ρ = 0.17, p = 0.3).
1277
1278 Spearman's correlation was used.

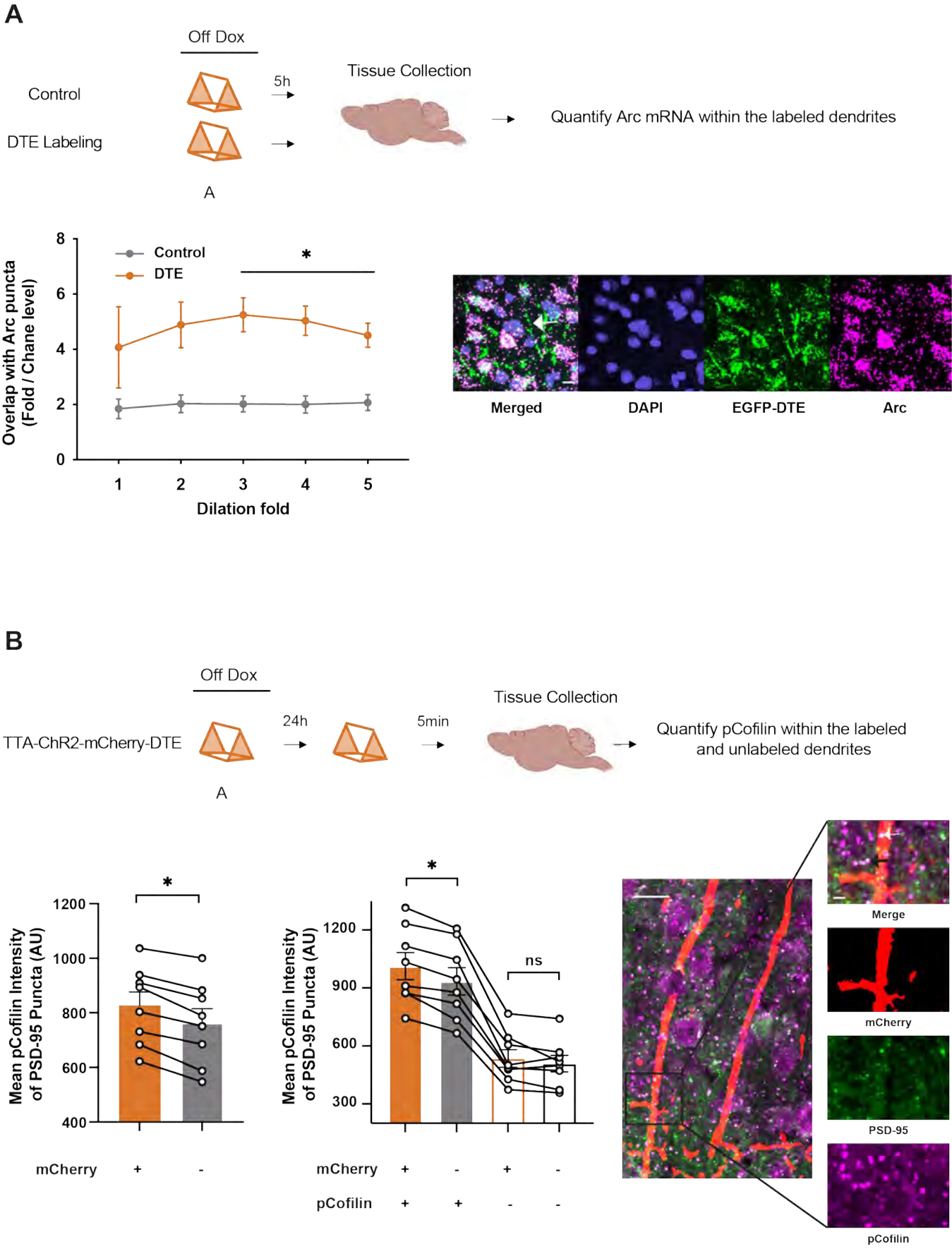
A
Off Dox
Control
DTE Labeling
5h
Tissue Collection
Quantify Arc mRNA within the labeled dendrites
A
Control
DTE
*
Overlap with Arc puncta (Fold / Chane level)
Dilation fold
Merged
DAPI
EGFP-DTE
Arc
B
Off Dox
TTA-ChR2-mCherry-DTE
24h
5min
Tissue Collection
Quantify pCofilin within the labeled and unlabeled dendrites
A
Mean pCofilin Intensity of PSD-95 Puncta (AU)
mCherry
pCofilin
ns
Merge
mCherry
PSD-95
pCofilin

Figure S17

Figure S17. DTE-mediated targeting labels recently activated dendritic segments.

(a) Dendritic segments labeled using DTE-mediated strategy are enriched in Arc mRNA. Top: Experimental Design; Mice in Control and DTE group were exposed to a novel context, brains were collected 5 hours later and processed for in situ hybridization to quantify mRNA for Arc and fluorescent reporter protein. Control group was designed to label a small but random subset of dendrites (CamKII-Cre::DIO-GFP in WT mice) and the DTE group used a low titer injection to label activated dendrites sparsely in an activity-dependent manner (cFos-tTa mice with TRE-Opsin-GFP-DTE).
Bottom: Regions of interest (ROI) were manually delineated to specifically isolate the fluorescent signal within dendrites (to exclude somatic regions). GFP and Arc signals within these ROIs were automatically segmented. A 1-5 fold dilation of the GFP signal was applied, and the volume of overlap between the dilated GFP signal and the Arc signal was quantified to determine the extent of their colocalization. Arc mRNA was enriched in labeled dendrites in the DTE vs Control group (Control: n = 3, DTE: n = 5; Two-way RM ANOVA, F_{Group} (1, 6) = 10.08, P < 0.05, Sidak's multiple comparisons test). Scale: 10 µm.

(b) Dendritic segments labeled using DTE-mediated strategy are preferentially reactivated upon re-exposure to the original labeling context. Experimental Design (Top): cFos-tTa mice injected with TRE-ChR2-mCherry-DTE virus underwent a novel context exposure and a re-exposure to the same context 24 hours later. Bottom Left: PSD-95 puncta on DTE labeled dendrites displayed more pCofilin labeling (n = 4 mice, 8 slices; Wilcoxon test, p < 0.05). Bottom Middle: Similarly, PSD-95 puncta that were classified as positively labeled for pCofilin (pCofilin+ PSD-95+) displayed higher fluorescence intensity when present on mCherry-labeled dendrites than neighboring pCofilin+ PSD-95+ puncta (Two-way RM ANOVA, F_{Group} (3, 21) = 137.7, P < 0.0001, Sidak's multiple comparisons test). Bottom right: Representative image depicting pCofilin-positive puncta (magenta) on PSD-95 (green) and mCherry-positive dendrite (red). White and black arrows represent pCofilin-positive, PSD-95-postive puncta on mCherry-positive dendrites and neighboring regions respectively. Scale: 10 µm, Inset Scale: 2 µm.

Data represent mean± s.e.m. and each data point, * $p < 0.05$.

Figure 2d
Context and fear encoding together (5h apart) to allow optogenetic manipulation 24h post-tagging

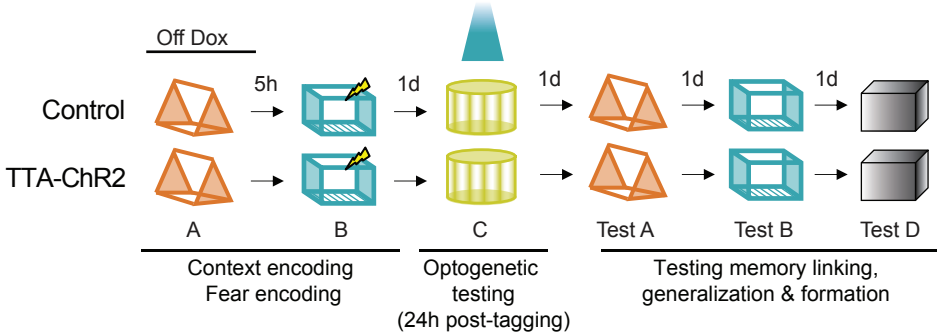

Figure 2e, 6f
Context and fear encoding are separated
Two contexts encodes (2d apart) to prevent linking under control conditions
Optogenetic manipulation 24h post-tagging

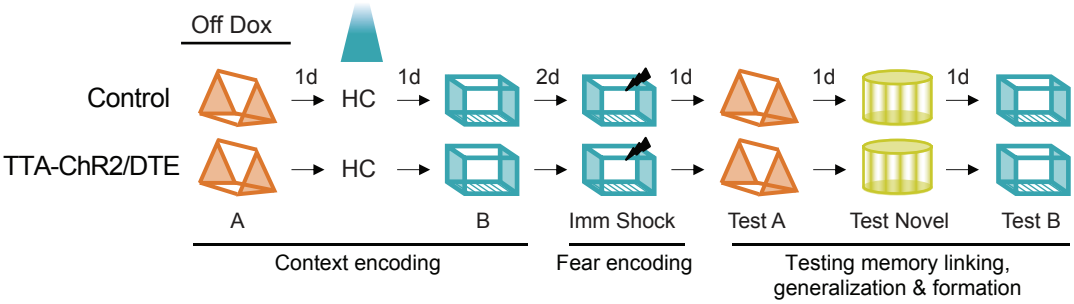

Figure S6
Context and fear encoding are separated
Two contexts encodes (2d apart) to prevent linking under control conditions
Chemogenetic activation 45mins pre-exposure

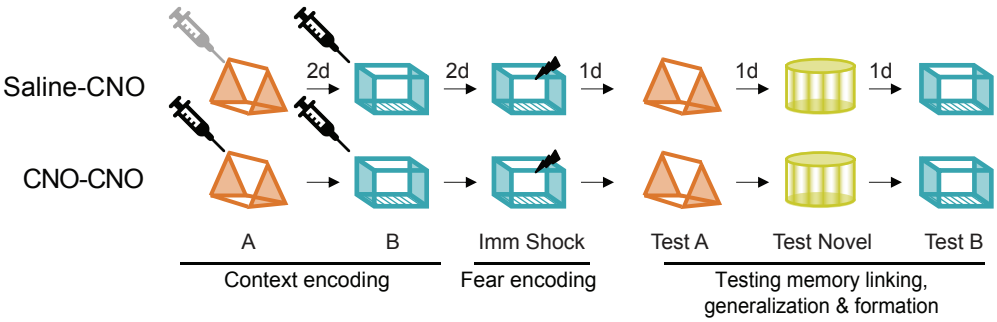

Figure S10
Context and fear encoding are separated
Two contexts are encoded (5h apart) to test the effect of anaesthesia on linking
45mins anaesthesia post-exposure

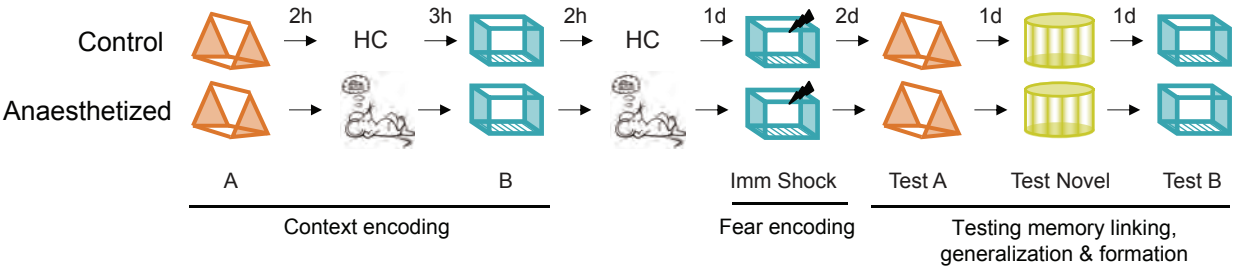

Figure S18

1310 **Figure S18. Rationale for behavioral experiments investigating memory linking.**

1311 **Supplementary Table 1**

Centroid Distance

SFP correlation	3	4	5	6	7	8	9
0.6	**7d**: 26.0 ± 4.8 **5h**: 50.6 ± 5.3 ***p*** = 0.0005	**7d**: 37.0 ± 5.4 **5h**: 59.7 ± 5.3 ***p*** = 0.002	**7d**: 46.8 ± 5.2 **5h**: 66.1 ± 4.1 ***p*** = 0.002	**7d**: 51.3 ± 5.0 **5h**: 70.2 ± 3.3 ***p*** = 0.0007	**7d:** 54.3 ± 4.6 **5h:** 72.6 ± 2.8 ***p*** = 0.0003	**7d:** 57.5 ± 4.3 **5h:** 74.5 ± 2.6 ***p*** = 0.0003	**7d:** 59.1 ± 4.2 **5h:** 75.3 ± 2.6 ***p*** = 0.0005
0.65	**7d**: 25.4 ± 4.6 **5h**: 50.1 ± 5.2 ***p*** = 0.0005	**7d**: 35.8 ± 5.3 **5h**: 58.8 ± 5.2 ***p*** = 0.001	**7d**: 44.7 ± 5.2 **5h**: 64.7 ± 4.1 ***p*** = 0.001	**7d**: 48.8 ± 5.0 **5h**: 68.6 ± 3.2 ***p*** = 0.0004	**7d:** 51.1 ± 4.7 **5h:** 70.5 ± 2.9 ***p*** = 0.0003	**7d:** 53.1 ± 4.5 **5h:** 72.0 ± 2.7 ***p*** = 0.0002	**7d:** 54.3 ± 4.5 **5h:** 72.6 ± 2.7 ***p*** = 0.0003
0.7	**7d**: 24.5 ± 4.5 **5h**: 49.3 ± 5.3 ***p*** = 0.0004	**7d**: 34.0 ± 5.1 **5h**: 57.9 ± 5.1 ***p*** = 0.0007	**7d**: 41.3 ± 5.1 **5h**: 63.3 ± 4.3 ***p*** = 0.0009	**7d**: 44.7 ± 4.9 **5h**: 66.4 ± 3.8 ***p*** = 0.0003	**7d:** 46.3 ± 4.7 **5h:** 67.9 ± 3.3 ***p*** = 0.0002	**7d:** 47.8 ± 4.7 **5h:** 69.1 ± 3.0 ***p*** = 0.0001	**7d:** 48.8 ± 4.6 **5h:** 69.5 ± 3.0 ***p*** = 0.0002
0.75	**7d**: 23.5± 4.3 **5h**: 47.4 ± 5.2 ***p*** = 0.0004	**7d**: 31.3 ± 4.9 **5h**: 55.5 ± 5.1 ***p*** = 0.0005	**7d**: 37.1 ± 5.0 **5h**: 59.8 ± 4.7 ***p*** = 0.0006	**7d**: 39.6 ± 4.8 **5h**: 62.3 ± 4.5 ***p*** = 0.0003	**7d:** 41.0 ± 4.7 **5h:** 63.6 ± 4.1 ***p*** = 0.0002	**7d:** 41.9 ± 4.7 **5h:** 64.6 ± 3.8 ***p*** = 0.0002	**7d:** 42.3 ± 4.7 **5h:** 64.9 ± 3.9 ***p*** = 0.0002
0.8	**7d**: 21.7 ± 4.1 **5h**: 45.0 ± 5.2 ***p*** = 0.0006	**7d**: 27.8 ± 4.7 **5h**: 52.1 ± 5.2 ***p*** = 0.0007	**7d**: 31.8 ± 4.8 **5h**: 55.8 ± 5.0 ***p*** = 0.0005	**7d**: 33.4 ± 4.7 **5h**: 57.7 ± 4.8 ***p*** = 0.0003	**7d:** 34.2 ± 4.7 **5h:** 58.3 ± 4.7 ***p*** = 0.0003	**7d:** 34.5 ± 4.7 **5h:** 58.8 ± 4.6 ***p*** = 0.0002	**7d:** 34.8 ± 4.7 **5h:** 58.9 ± 4.6 ***p*** = 0.0002
0.85	**7d**: 17.8 ± 4.0 **5h**: 39.9 ± 5.0 ***p*** = 0.0008	**7d**: 22.2 ± 4.6 **5h**: 44.8 ± 5.2 ***p*** = 0.001	**7d**: 24.2 ± 4.7 **5h**: 47.3 ± 5.0 ***p*** = 0.0009	**7d**: 24.9 ± 4.6 **5h**: 48.5 ± 4.9 ***p*** = 0.0006	**7d:** 25.3 ± 4.6 **5h:** 48.8 ± 4.8 ***p*** = 0.0006	**7d:** 25.5 ± 4.6 **5h:** 49.2 ± 4.8 ***p*** = 0.0005	**7d:** 25.7 ± 4.6 **5h:** 49.3 ± 4.7 ***p*** = 0.0005
0.9	**7d**: 11.9 ± 3.1 **5h**: 31.8 ± 4.5 ***p*** = 0.001	**7d**: 13.9 ± 3.3 **5h**: 34.5 ± 4.6 ***p*** = 0.0008	**7d**: 14.6 ± 3.4 **5h**: 35.7 ± 4.5 ***p*** = 0.0007	**7d**: 14.8 ± 3.4 **5h**: 36.2 ± 4.4 ***p*** = 0.0006	**7d:** 15.0 ± 3.4 **5d:** 36.4 ± 4.4 ***p*** = 0.0006	**7d:** 15.1 ± 3.4 **5h:** 36.6 ± 4.3 ***p*** = 0.0005	**7d:** 15.1 ± 3.4 **5h:** 36.7 ± 4.3 ***p*** = 0.0005
0.95	**7d**: 3.9 ± 1.1 **5h**: 15.3 ± 3.3 ***p*** = 0.003	**7d**: 4.2 ± 1.1 **5h**: 15.8 ± 3.5 ***p*** = 0.004	**7d**: 4.2 ± 1.1 **5h**: 16.1 ± 3.4 ***p*** = 0.003	**7d**: 4.3 ± 1.1 **5h**: 16.2 ± 3.4 ***p*** = 0.003	**7d:** 4.3 ± 1.1 **5d:** 16.2 ± 3.4 ***p*** = 0.003	**7d:** 4.3 ± 1.1 **5h:** 16.2 ± 3.4 ***p*** = 0.003	**7d:** 4.3 ± 1.1 **5h:** 16.4 ± 3.4 ***p*** = 0.003

1312

1313 **Supplementary Table 2**

Parameters of the computational model		
N_{pyr}	Number of excitatory neurons	400
N_{inh}	Number of inhibitory neurons	50 dendrite-targeting (DT) 50 soma-targeting (ST)
N_{dend}	Number of dendritic subunits per neuron	10 for excitatory 1 for interneurons
$N_{pyr\rightarrow ST}$	Synapses from excitatory neurons to soma-targeting(ST) interneurons	Count: 1000 Weight: 0.6
$N_{pyr\rightarrow DT}$	Synapses from excitatory neurons to dendrite-targeting (DT)	Count: 1000 Weight: 0.3
$N_{ST\rightarrow pyr}$	Synapses from ST interneurons to excitatory neurons	Count: 10000 Weight: 0.5
$N_{DT\rightarrow pyr}$	Synapses from DT interneurons to excitatory neurons	Count: 2000 Weight: 0.3
$N_{input\rightarrow pyr}$	Synapses from input afferents to pyramidal dendrites per encoded memory	Count: 23000 Initial Weight: 0.16 – 0.36
E_L	Leakage reversal potential	0 mV
g_E / g_I	Dendritic excitatory / inhibitory synaptic conductance	22nS / 20nS
g_{Ld} / g_L	Dendritic/somatic leak conductance	10nS / 8nS
g_{Inh}	Somatic inhibitory current scaling constant	600nS
τ_{Inh}	Somatic inhibitory current time constant	30msec
E_E / E_I	Excitatory /inhibitory synapse reversal potential	+70mV / -10mV
C	Membrane capacitance	200pF
τ_{dend}	Dendritic membrane time constant	Inhibitory: 20msec Excitatory: 25msec
V_d	Dendritic Depolarization	$-10mV < V_d < 70mV$
g_{ax}	Axial conductance	36nS
θ_{soma}	Voltage threshold for somatic spikes	18mV
τ_{adapt}	Adaptation time constant of excitatory neurons	200msec
β_{adapt}	Adaptation reset constant	Baseline excitability: 9 High excitability: 6.5
a_{adapt}	Adaptation coupling parameter	0.02
Θ_{PRP}	Calcium threshold for somatic Plasticity-Related Protein (PRP) synthesis	40.0
Θ_{dend}	Calcium threshold for dendritic excitability	2.0
Θ_{soma}	Calcium threshold for somatic excitability	40.0
τ_H	Time constant of homeostatic synaptic scaling	1440 hours

1314
1315

1316 **METHODS**

1317 ***Animals.*** All experimental protocols were approved by the Chancellor's Animal Research
1318 Committee of the University of California, Los Angeles, in accordance with NIH guidelines. cFos-
1319 tTa mice that express tetracycline transactivator (tTA) protein under the control of the c-fos (also
1320 known as Fos) promoter were maintained in a C57BL/6N background. Adult (3–8 months old)
1321 male and female Thy1-YFP-H mice (Jackson Laboratories, Stock No: 003782) were used for
1322 structural imaging experiments. C57BL/6N Tac mice were purchased from Taconic Farms
1323 (Germantown, NY) for all other experiments.

1324 ***Viral construct***. pAAV-Syn-GCaMP6f-WPRE-SV40 was a gift from Douglas Kim &
1325 GENIE Project (Addgene viral prep # 100837-AAV1; http://n2t.net/addgene:100837; RRID:
1326 Addgene 100837). The lentivirus hM3Dq-T2A-EGFP vector was derived as previously described
1327 in Cai et al., 2016 [12]. Finally, AAV1-TRE-hChR2-mCherry, AAV1-TRE-hChR2-mCherry-DTE and
1328 AAV1-TRE-mCherry-DTE were derived in our laboratory. Briefly, to construct a vector for TRE-
1329 driven hChR2 expression, a CamKIIa promoter from pAAV-CamKIIa-hChR2(H143R)-mCherry
1330 (Addgene #26975) was replaced with TRE promoter from pAAV-RAM-d2tTA::TRE-NLS-mKate2-
1331 WPRE (Addgene #84474) using MluI/AgeI digestion. The DTE sequence of Arc mRNA was PCR-
1332 amplified from cDNA of 14 weeks Spraque-Dawley rat using primers as previously described [18]
1333 and inserted into the pAAV-TRE-hChR2-mCherry vector using EcoRI/HindIII. The pAAV-TRE-
1334 hChR2-mCherry and pAAV-TRE-hChR2-mCherry-DTE were subjected to AgeI/BsrGI digestion
1335 for construction of mCherry vectors, respectively. The mCherry was digested by AgeI/BsrGI from
1336 pmCherry-N1. AAV production was conducted as previously described in detail [100] with
1337 modifications.

1338 ***Surgery.*** Mice were anesthetized with 1.5 to 2.0% isoflurane for surgical procedures and
1339 placed into a stereotactic frame (David Kopf Instruments, Tujunga, CA) on a heating pad. Artificial
1340 tears were applied to the eyes to prevent drying. Subcutaneous saline injections were
1341 administered throughout each surgical procedure to prevent dehydration. In addition, carprofen

1342 (5 mg kg−1) and dexamethasone (0.2 mg kg−1) were administered both during surgery and for
1343 2-7 days post-surgery. A midline incision was made down the scalp, and a craniotomy was
1344 performed with a dental drill. Water with amoxicillin was administered for two weeks.

1345 ***Miniscope experiments.*** *Surgeries.* Mice were unilaterally microinjected with 500 nl of
1346 AAV1-Syn-GCaMP6f-WPRE-SV40 virus at 20 -120 nl/min into the RSC using the stereotactic
1347 coordinates: −2.3 mm posterior to bregma, 0.5 mm lateral to the midline, and −0.8 mm ventral to
1348 the skull surface. Immediately afterward, the microendoscope (a gradient refractive index or GRIN
1349 lens) was implanted above the injection site. For this procedure, a 2.0 mm diameter circular
1350 craniotomy was centered above the virus injection site. The microendoscope (0.25 pitch, 0.50
1351 NA, 2.0 mm in diameter, and 4.79 mm in length, Grintech Gmbh) was slowly lowered with a
1352 stereotaxic arm above the craniotomy 450 μm ventral to the surface of the skull. Next, a skull
1353 screw was used to anchor the microendoscope to the skull. Both the microendoscope and skull
1354 screw were fixed with cyanoacrylate and dental cement. Kwik-Sil (World Precision Instruments)
1355 was used to cover the microendoscope. Three weeks later, a small aluminum baseplate was
1356 cemented onto the animal's head atop the previously placed dental cement. The microscope was
1357 placed on top of the baseplate and locked in a position such that the field of view contained cells
1358 and visible landmarks, such as blood vessels, and these appeared sharp and in focus. Finally, a
1359 plastic headcap was fit into the baseplate and secured with magnets. Independent experiments
1360 confirmed that GCaMP6f expression was limited to RSC neurons (Figure 1b).

1361 *Miniscope Behavior.* Customized UCLA Miniscopes V3 with a 20mm achromatic doublet
1362 lens and modified housing were used to allow imaging 300 μm below the surface of the GRIN
1363 lens allowing imaging of RSC neurons. Using head-mounted miniature microscopes (UCLA
1364 Miniscopes V3)(*4*, *38*), we imaged GCaMP6f-mediated calcium dynamics in RSC neurons of
1365 GRIN lens implanted mice that explored distinct contexts. Before imaging sessions, mice were
1366 handled and habituated to the experimental conditions, including carrying the Miniscope while it

1367 was tethered to the implanted GRIN lens. Mice were exposed to each context (with distinct visual,
1368 auditory, and olfactory cues) for 10 mins during which calcium transients were recorded (Figure
1369 1c for representative calcium transients). Context A was separated from Context B by 7 days, and
1370 Context B and Context C were separated by 5 hours (Figure 1e). The actual contexts used were
1371 counterbalanced and comprised of rectangular plastic containers (15 ± 1 by 11 ± 1 inches) that
1372 were covered with various visual cues.

1373 *Miniscope Analysis.* Calcium imaging data were registered to remove small movement
1374 artifacts using NormCorre [101]. This was followed by automated segmentation, demixing, and
1375 denoising of calcium signals using constrained non-negative matrix factorization for endoscopic
1376 data (CNMFe) [102]. We used a modified version of the Miniscope analysis package developed by
1377 Guillaume Etter (Sylvain Williams Lab, McGill University) for data analysis [103]. Recordings from
1378 multiple sessions of the same mouse were aligned using an amplitude-based registration
1379 algorithm used for within-session registration, except the algorithm was only applied to the mean
1380 frame from each session. Once regions of interest (ROIs- putative neurons) from two sessions
1381 were registered, ROIs across two sessions were matched to each other using a distance
1382 (between ROI centroids) and correlation (between ROIs spatial footprints - SFPs) measure. The
1383 neuronal ensemble overlap was calculated as the percentage of ROIs activated in both contexts
1384 divided by the average number of ROIs identified in each imaging session. Neurons were
1385 matched across days based on distance (< 4 pixels) and correlation (> 0.9) thresholds. These
1386 results (Figure 1e) were consistent and robust for a range of distance (3-9 pixels) and correlation
1387 (0.6-0.95) thresholds used to match segments across days (data not shown).

1388 In a parallel approach, we aligned and concatenated the imaging data from the three
1389 context exposures into a single video file (followed by motion correction and segmentation as
1390 described above) and analyzed the data such that we were able to detect and track the activity of
1391 ROIs across all different sessions as well as investigate their modulation during context
1392 exploration. The raw data from CNMFe extracted putative neurons was deconvolved into spike

probabilities using the foopsi thresholded method (OASIS toolbox). Finally, the spike probabilities from single frames were binarized between 1 (active) and 0 (inactive). For each neuron, the firing rate (number of active frames per second) for each session was estimated. Population Vector Correlations (PVCs) were calculated as the Pearson correlation between the average firing rate (per session) of each neuron across two imaging sessions (Figure S2).

Naïve Bayes (NB) Binary Classifier. The activity of each neuron during each 10 min session was resampled into various time bin sizes (0.5-60 second bins, step size 0.5s; Figure S2). Each resampled data with a specific bin size was used as trials from each session. The classifier was trained on 90% of the data and we used the information contained in the probability of activity from each neuron to test the remaining 10% data (10-fold cross-validation strategy) as belonging to the two given sessions. The area under the receiver operating characteristic curve (AUC) was calculated for the first context (A for 7d or B for 5h; Figure 1g) using the Wilcoxon-Mann-Whitney statistic. The quality of the classification is defined by AUC, which ranges from 0 to 1. AUC = ~0.5 means sorting at chance levels by the classifier.

Pairwise correlations (PWC) maps for each session were calculated by binning neuronal activity into 100ms bins to compute the Pearson correlation for each pair of neurons (Figure S5a,b). PWC stability was calculated as the Pearson correlation between PWC maps from different sessions, excluding the main diagonal (correlation between each neuron with itself) and cell pairs below the main diagonal (such that each cell pair was represented only once). Since artificially high correlations can arise due to sub-optimal demixing of calcium signals from nearby ROIs, we computed the PWC analysis while ignoring the PWCs from nearby cell pairs. We defined nearby cells as cell pairs where spatial footprints (SFP) had any overlap or where the centroid to centroid distance was shorter or equal to 20 pixels (~40 μm). To control for the different number of neurons detected for different mice, we calculated PWC stability between 2 sessions by randomly subsampling a group of 10 cells, computing the PWC map for each of the sessions using these cells, and computing the Pearson correlation between the two PWC maps. This

1419 process was repeated 1000 times and the final PWC stability was defined as the average of these
1420 1000 values. The absolute PWC per imaging session and PWC stability across sessions follows
1421 the same trend whether the analyses were done with or without nearby cells or with subsampling
1422 of 50 cells instead of 10 cells (t=3.61, p = 0.006). For brevity, we only present analyses that
1423 excluded the nearby neurons.

1424 ***Optogenetic experiments.*** Adult male and female (3-8 months) cFos-tTa transgenic and
1425 their wild-type littermates maintained on doxycycline chow (for 1 month or more) were bilaterally
1426 microinjected with 500 nl of AAV1-TRE-hChR2-mCherry, AAV1-TRE-hChR2-mCherry-DTE,
1427 AAV1-TRE-mCherry-DTE virus at 20-50 nl min^{-1} into the RSC using the stereotactic coordinates:
1428 −2.3 mm posterior to bregma, 0.5 mm lateral to the midline, and −0.8 mm ventral to the skull
1429 surface. For Figure S8, wild-type mice were injected with a cocktail of CamKII-Cre (Addgene
1430 105558-AAV, diluted $1:10^3$) with DIO-hChR2 (Addgene 35509-AAV9 – Experimental) or DIO-GFP
1431 (Control). Following viral injections, bilateral optogenetic cannulae (Doric Lenses Inc.;
1432 DFC_200/240-0.22_0.5mm_GS1.0_FLT) were implanted over the injection site at −0.45 mm
1433 ventral to the skull surface.

1434 ***Chemogenetic experiments.*** Adult (3-5 months old) C57Bl/6NTac male mice were
1435 bilaterally microinjected with 1000 nl of lentivirus hM3Dq.T2A.EGFP at 20-100 nl/min into the RSC
1436 using the stereotactic coordinates: -1.95 and −2.65 mm posterior to bregma, 0.5 mm lateral to the
1437 midline, and −0.8 mm ventral to the skull surface. Following viral injections, mice were allowed to
1438 recover from surgeries for 3 weeks before being handled (3 days) and habituated (3 days) for a
1439 modified two-day memory linking experiment. To ensure that the same RSC neurons are recruited
1440 for encoding these different contexts, we transiently increased the intrinsic excitability of a small
1441 subset of RSC neurons by administering a clozapine N-oxide (CNO, 0.5mg/kg) injection 45 mins
1442 before each context exploration [12]. The control mice only received the CNO injection before the
1443 second context exploration. Following this, the mice underwent the memory linking paradigm
1444 described below.

1445 ***Memory linking studies.*** Linking of context memories was carried out as previously
1446 described [12]. Briefly, mice were handled for 3 days (2–5 min/day) and then habituated to
1447 transportation and experimental room/s for 3-5 days (2-5 mins/ day). In the memory linking task,
1448 mice explored 2 distinct contexts (A and then B, for 10 mins each) separated by 5h (Figure 2d
1449 and S14) for linking under control conditions or 2 days (Figures 2e, 6f, S8 and S9) to ensure a
1450 robust lack of linking under control conditions[48]. The actual contexts presented were
1451 counterbalanced to minimize any effect of context similarity. For Figure 2d: The context exposure
1452 in chamber B also included a 2s, 0.75mA footshock that was delivered 58 seconds before the end
1453 of context exposure. This was done to shorten the window of time between the encoding of the
1454 first contextual memory (for activity-dependent tagging), subsequent linking, and optogenetic
1455 manipulation to 24 hours post-tagging. All optogenetic manipulations were performed 24 hours
1456 post-tagging to ensure sufficient expression of the tagged opsin (Figure S18).

1457 Manipulation to link normally independent memories: For experiments where we extended
1458 the time window for memory linking by manipulating neuronal (Figure 2e) or dendritic overlap
1459 (Figure 6f), the two context exposures were separated by 2 days. We did this for two reasons.
1460 First, two contexts explored 5 hours apart are linked but when contexts are explored 2 days apart,
1461 they are not linked[12,48]. Second, Channelrhodopsin expression under the TetTag system peaks
1462 at 24 hours [43]. This allowed us to extend the window of memory linking (to 2 days) by using the
1463 transient expression of Channelrhodopsin on a day after the first context exposure.

1464 Immediate shock: For Figures 2e and 6f: Two days following the last context exposure (in
1465 B), mice were placed in context B again for an immediate foot shock (10 second baseline, 2
1466 second shock, 0.7-0.75mA, 28-58 second post-shock period). For Figure S14: To compensate
1467 for the lower freezing seen in C57Bl/6N Jackson mice (the genetic background of the Thy1-YFP
1468 mice), the immediate shock protocol was modified to a 10 second baseline, two shocks for 2
1469 seconds each, 0.75mA, 15 seconds apart.

1470 Testing: During the testing phase, mice were tested in the designated contexts (5 minutes
1471 each) on three separate days to minimize any effects of testing animals in one context on
1472 subsequent tests in another context. The order of testing was also chosen to control for any
1473 gradual increase or decrease in freezing. The actual contexts were counterbalanced. Freezing
1474 was assessed via an automated scoring system (Med Associates) with 30 frames per second
1475 sampling rate; the mice needed to freeze continuously for at least one second before freezing
1476 could be counted.

1477 ***Tagging of RSC ensemble:*** Mice were allowed to recover from surgeries for 3-5 weeks
1478 before being handled (3 days) and habituated (3-5 days) for behavioral exposure as well as
1479 optogenetic manipulation. The day after the last day of habituation, mice were taken off
1480 doxycycline chow (40 mg $kg^{-1)}$ and placed on regular chow and tTA expression was allowed for 3
1481 days before behavioral tagging for the memory linking experiments. The activity-dependent tag
1482 was shut off by administration of high dox chow (200 mg kg^{-1}) 90 minutes after behavioral tagging.
1483 For experiment in Figures 2d and S7 a subset of animals was also administered doxycycline
1484 intraperitoneally (i.p, 50 ug/ gram of body weight; 2 hour post tagging episode) to ensure that the
1485 tagging window is closed even in the absence of immediate feeding. The dose and timing were
1486 chosen because of its effectiveness in initiating tagging with the Tet-On system [104]. Doxycycline
1487 is also detectable at near peak levels 2 hours post injection in the brain tissue [105]. Our behavioral
1488 results remain the same with and without doxycycline administration i.p. and hence we have
1489 combined data from these two sets of experiments in Figure 2d. Set 1 (without i.p. doxycycline):
1490 Animals were placed back on high dox chow 90 mins post context A exposure. Control, n = 4;
1491 TTA-ChR2, n = 6; Two-way RM ANOVA, $F_{Interaction}$ (1, 8) = 5.4, $p < 0.05$; Sidak's multiple
1492 comparisons test, $p < 0.005$). Set 2 (with i.p. doxycycline): Animals were placed back on high dox
1493 chow and injected with doxycycline i.p. 2 hours post context A exposure. Control, n = 12; TTA-
1494 ChR2, n = 8; Two-way RM ANOVA, $F_{Interaction}$ (1, 18) = 5.4, $p < 0.05$; Sidak's multiple comparisons

1495 test, $p < 0.005$). Combined: Control, n = 16; TTA-ChR2, n = 14; Two-way RM ANOVA, $F_{Interaction}$
1496 (1, 28) = 12.8, $p < 0.005$; Sidak's multiple comparisons test, $p < 0.0001$).

1497 ***Optogenetic Manipulations:*** All optogenetic manipulations were performed 24 hours
1498 following the tagging event to ensure sufficient expression of the opsins.

1499 *Reactivation of tagged ensembles in home cage:* For Figures 2e and 6f, ensembles
1500 tagged during the first context exposure were reactivated in the home cage using a 473nm laser
1501 (5 ms pulses, 5 Hz) for 10 minutes. *Testing:* For Figure 2c-d, mice were placed in an open field
1502 and freezing behavior was recorded using a digital camera. Following a 3-minute baseline period,
1503 the tagged RSC ensemble was reactivated using a 473nm laser (5 ms pulses, 5 Hz) for one
1504 minute followed by a one-minute interval with no stimulation. This pattern of stimulation was
1505 repeated three times, and the time spent freezing during the three epochs was averaged.

1506 ***Immunostaining***

1507 Mice were transcardially perfused with 0.1 M phosphate buffer followed by 4% PFA (4%
1508 paraformaldehyde in 0.1 M phosphate buffer) and after perfusion, brains were kept in the fixation
1509 solution overnight at 4 °C, then transferred to 30% sucrose solution for 48 h, sectioned (40 μm
1510 thickness) on a cryostat and stained while free-floating. For staining synaptic proteins, tissue was
1511 sectioned at 15 μm thickness.

1512 The sections were blocked for 1 h at room temperature in 0.3% Triton-X in PBS (PBST)
1513 and 10% normal goat serum (Vector Laboratories, S-1000) solution. Primary and secondary
1514 antibodies were diluted in the same blocking solution. The primary antibody (guinea pig anti-RFP:
1515 SySy 390004, chicken anti-RFP: SySy 409006, anti-PSD95: SySy 124308, anti-phospho-Cofilin;
1516 Millipore C8992) incubation was overnight (~18 h) at 4 °C, and the secondary antibody (Alexa
1517 Fluor 488, 568, 647: Invitrogen) incubation was 2 h at room temperature, both with constant
1518 shaking. Brain slices were incubated with 4',6-diaminodino-2-phenylindole (DAPI, Invitrogen,
1519 1:1000) for 10 min, washed with PBST two times and PBS once before mounting onto slides.
1520 Immunostaining images were acquired with a Nikon A1 Laser Scanning Confocal Microscope

1521 (LSCM) and analyzed with automatic spot-detection algorithm (Imaris 9.2, Bitplane AG) and
1522 manually verified.

1523 **In situ hybridization**

1524 Control mice were WT C57BL/6N mice that were injected with a cocktail of CamKII-Cre
1525 (Addgene 105558-AAV1, diluted 1:10^3) and DIO-GFP viruses to label a sparse and random
1526 subset of RSC neurons. DTE group comprised of cFos-tTa mice injected with TRE-Opsin-GFP-
1527 DTE (10^{11} gc/ml) to sparsely label dendrites in an activity-dependent manner. Mice brains were
1528 dissected and fast-frozen in optimal cutting temperature compound (OCT) using dry ice without
1529 paraformaldehyde (PFA) fixation. Frozen sections were sliced (15μm). In situ hybridization was
1530 performed using the RNAscope™ Multiplex Fluorescent Reagent Kit v2 (ACD, 323100) according
1531 to the manufacturer's instructions. Probe-GFP (ACD, 409011) and Probe-Mm-Arc (316921) were
1532 used for mRNA labeling.

1533 The images were acquired using NIS-Elements AR (Nikon, v.4.40.00) with a Nikon A1
1534 Laser Scanning Confocal Microscope (LSCM). Analysis of the confocal images was conducted
1535 using NIS-Elements AR Analysis software (Nikon, v.4.40.00). To perform the analysis, regions of
1536 interest (ROI) were manually delineated to specifically isolate the GFP signal within dendrites
1537 (excluding the soma). The GFP and Arc signals within these ROIs were automatically segmented
1538 using thresholding techniques. A 1-5 fold dilation of the GFP signal was applied, and the volume
1539 of overlap between the dilated GFP signal and the Arc signal was quantified to determine the
1540 extent of their colocalization as follows**:**

1541 **Chance level = (GFP volume / ROI total volume) * (Arc Volume / ROI total volume)**

1542 **Arc overlap possibility = (GFP and Arc overlap volume / ROI total volume) / Chance level**

1543 ***Structural 2p imaging.*** *Methods.* Adult (3-8 months old) male and female Thy1-YFP-H
1544 mice were used for structural imaging experiments. Mice underwent window implantation
1545 surgeries as previously described [19]. Briefly, a square region of the skull 2-3 mm in width was
1546 marked using stereotactic coordinates (RSC: center at bregma -2.3 mm AP). The skull was

1547 thinned using a dental drill and removed. After cleaning the surgical site with saline, a custom cut
1548 sterilized coverslip (square, 2x2mm unilateral or 3x3mm bilateral) was placed on the dural surface
1549 and fastened with adhesive and dental acrylics to expose a square window of approximately 2
1550 mm. Next, an aluminum bar with a threaded hole was attached to stabilize the mice during imaging
1551 sessions. Mice were allowed to recover for two or more weeks before the first imaging session.
1552 Following recovery from surgery, mice were handled and habituated as per the memory linking
1553 paradigm. In addition, mice were also habituated for transportation to the imaging room as well
1554 as anesthesia. After handling/habituation (1-2 days later), mice underwent the first home cage
1555 baseline imaging session. Two days later mice underwent the second baseline imaging session.
1556 Two days following the last baseline imaging session, a subset of mice was exposed to a novel
1557 context 'A' for 10 minutes while another subgroup remained in the home cage (control group).
1558 After 7 days, mice were exposed to a novel context (B, 10 minutes) which was followed by a third
1559 novel context exposure (C, 10 minutes) five hours later. Mice were imaged 2 hours after each
1560 context exposure.

1561 Two-Photon imaging measuring spine dynamics. A custom-built two-photon laser
1562 scanning microscope was paired with a Spectra-Physics two-photon laser tuned to 920nm. A 40x
1563 1.0 NA water immersion objective (Zeiss) was used to acquire images 2 hours after each
1564 behavioral session. Mice were lightly anesthetized with isoflurane and attached to the head mount
1565 using a small screw. During the first imaging session, segments of apical dendrites from layer V
1566 pyramidal cells were imaged. These segments were acquired within 200 μm from the cortical
1567 surface, likely representing dendrites located in layers I and II/III. Imaged segments were
1568 generally oriented in the x,y plane of imaging with minimal z-projection. 512x512 pixel images
1569 were acquired at 0.5 μm intervals to fully capture the segment of dendrite, and image stacks
1570 generally consisting of 30-40 slices. If a segment of dendrite was larger than could be acquired
1571 in one 512x512 pixel stack, additional image stacks were sequentially acquired through the x,y,z

1572 plane of the dendrite in question so that its full extent could be visualized. The same segments
1573 were repeatedly imaged across experimental days by locating their position via a coordinate
1574 system established during the first imaging session.

1575 *Image and Data Analysis.* Dendritic spines were analyzed and counted by established
1576 criteria. Specifically, the Spine Analysis software included in ScanImage was used to open all
1577 imaging days for a given segment of dendrite. A segment was classified as the entire visible length
1578 of a piece of a dendrite, and segments were often followed across several images. The presence,
1579 gain, and loss of spines was quantified across days for each segment, and all segments were
1580 examined for a given animal. Importantly, all images were coded following the completion of the
1581 experiment so that the experimenter was blind to the training status of all mice while analyzing
1582 and counting spines. Dependence between new spines added to a dendritic segment following
1583 various imaging sessions was calculated using Spearman's correlation and mutual information.
1584 Spearman's rho (ρ) was used as the spine addition/loss data did not follow a normal distribution.
1585 Bonferroni method was used to correct for multiple comparisons. For mutual information analysis,
1586 statistical significance was calculated by comparing the observed value to the z-score of the
1587 chance distribution. A distribution of chance values was calculated by randomly permuting the
1588 number of spines added during the second imaging session (10,000x).

1589 Clustering ratios were calculated as the number of clustered spines divided by the total
1590 number of new spines gained between two time points. Clustered spines were defined as a new
1591 spine that was less than 5 μm from another new spine. For the resampling analysis of clustering,
1592 the number of new spines added per segment of dendrite was used to pick an equivalent number
1593 of random positions along the same segment (regardless of whether a spine was recorded on
1594 that spot on a previous imaging sessions) and assess whether these positions were within 5 μm
1595 of each other. When this was completed for all dendrites for a given animal, the percent of
1596 clustered spines was calculated as the number of randomly selected new spine positions within
1597 5 μm of each other divided by the total number of stably added new spines for that animal. In turn,

1598 each animal's resampled clustering percentage was calculated, and then these values were
1599 averaged together. This completed one resampling event, and this process was then repeated
1600 for a total of 1000 resampling events, which then yielded the full distribution of random sampling
1601 (Figure S15).

1602 *Cross Clustering across exposures.* The number of clustered spines added following a
1603 context exposure were randomly distributed on the dendritic segments from that mouse (10,000x).
1604 The percentage of clustered spines added to a dendritic segment following the first context
1605 exposure, that were added to a segment that also gained clustered spines following the
1606 subsequent context exposure, were measured and compared to the shuffled distribution obtained
1607 from the above analysis. Distance between two newly formed spines following each imaging
1608 session was calculated for spine pairs that were the nearest neighbors. If no new spine was added
1609 or the no newly formed spines persisted during the final imaging session (reference session),
1610 these dendrites were not considered during the analysis. Our results remain the same when
1611 dendrites with non-persistent or no newly added spines are included in the analysis (5h: 32.1%,
1612 average distance between nearest neighbors = 18.1 ± 2.2μm; 7d: 11.1%, average distance
1613 between nearest neighbors = 30.9 ± 2.3μm; $p < 0.0001$). In this case, the length of the dendritic
1614 segment was considered the average distance between nearest neighbors.

1615 Resampling Analysis (Figure 5 e-g): Dendritic branches (n = 40) from each condition
1616 were subsampled (10,000X) to obtain cumulative frequency distribution for Spearman
1617 Correlations, Mutual Information, and spine clustering probability for each condition. Insets
1618 demonstrate the difference between observed measurements for each variable from context
1619 exposure and HC groups imaged at the 5h interval. P values were calculated as: (Number of
1620 measurements where the difference between experimental vs control group < 0/10,000).

1621 ***Functional two-photon Imaging***. Mice underwent bilateral injection of diluted GCaMP6f
1622 (final concentration ~10^{11} vg/mL) in the RSC to achieve semi-sparse infection of layer V RSC

1623 neurons [106] using the stereotactic coordinates: −2.3 mm posterior to bregma, 0.5 mm lateral to the
1624 midline, and −0.8 mm ventral to the skull surface. All dendritic imaging experiments were
1625 completed within 25 days of virus injection to prevent viral overexpression. A square 3mm x 3mm
1626 craniotomy spanning the midline and hence revealing both RSCs was then made over the
1627 injection. After cleaning the surgical site with saline, the coverslip was placed on the dural surface
1628 and fastened with adhesive and dental acrylics to expose a square window. Next, an aluminum
1629 bar with a threaded hole was attached to stabilize the mice during imaging sessions. Two to three
1630 weeks following the surgery, mice underwent handling (3 days) and habituation (3 days) to
1631 acclimate to the treadmill and head-fixation. Neuronal and dendritic calcium activity was imaged
1632 in head-fixed mice that were free to run on a head-fixed setup.

1633 We recorded dendritic signals during context exposure as well as those evoked
1634 spontaneously using a resonant-scanning two-photon microscope (Neurolabware) controlled by
1635 Scanbox acquisition software. Distinct contexts were created by immobilizing the mice either on
1636 a running wheel, a treadmill, or a horizontal disc (Figure S10), in addition to distinct auditory,
1637 olfactory and visual cues associated with each context. Visual stimuli were presented on a large
1638 LCD monitor directly in front of the animal and 18 cm from the eye. Visual stimuli consisted of
1639 non-repeating natural movies with intermittent gray screens (9s on, 14s off). Spontaneous
1640 response data was collected with a blank gray screen in the absence of auditory and olfactory
1641 cues. A Coherent Discovery laser (Coherent Inc.) was used for GCaMP excitation, fixed at a
1642 wavelength of 920 nm. The objective used was a 16x water-immersion lens (Nikon, 0.8NA, 3 mm
1643 working distance). Image sequences were captured at 15.5 Hz at a depth of 30-50 μm below the
1644 brain surface for apical tuft dendrites and 320-450 μm for layer V RSC neurons in separate
1645 animals.

1646 Collected data were processed using the Suite2P analysis pipeline [107]. Recorded frames
1647 were aligned using a non-rigid motion correction algorithm. Following alignment, any frames with
1648 significant motion in the z-axis were dropped from the original video and the data were reanalyzed.

1649 Regions of interest (representing dendritic segments) were segmented in a semi-automated
1650 manner using a Suite 2p based classifier. Dendritic segments were matched across imaging
1651 sessions using an open-source algorithm (https://github.com/ransona/ROIMatchPub, matching
1652 criteria: correlation: 0.4). The percentage of reactivated dendrites was defined as the number of
1653 matched segments normalized to the average number of dendritic segments detected in each
1654 imaging session.

1655 **Hierarchical clustering of dendritic ROIs:** To account for global dendritic calcium events
1656 and/ or back-propagating action potentials that invade more than one dendritic ROI from the same
1657 neuron, we merged any dendritic ROI with highly correlated calcium transients into a single
1658 dendritic segment. We adapted a hierarchical clustering method [108] previously used to assign
1659 axonal boutons to the same source with some variations. Briefly, we generated a sparse activity
1660 matrix by thresholding calcium transients from each ROI such that only frames with activity three
1661 standard deviations above the mean activity were retained. The time course of calcium transients
1662 for each ROI was then cross-correlated with all other ROIs during the same session to generate
1663 a matrix of Pearson correlation coefficients between all ROI pairs. This matrix was thresholded in
1664 two ways to obtain a sparse matrix. Only those correlation coefficients that were either larger than
1665 0.7 or exceeded 2.5 x standard deviations above the mean value of all the coefficients between
1666 this ROI and all others were used. If neither of these conditions were met for a given ROI pair,
1667 the associated correlation coefficient was set to 0. The cosine similarity between every ROI pair
1668 was then computed from the thresholded matrix of Pearson correlation coefficients.

1669 Next, we classified ROIs with similar activities into clusters using agglomerative
1670 hierarchical clustering based on the pairwise distance, computed as '1 – cosine similarity' and the
1671 weighted-pair group method with arithmetic means (WPGMA) algorithm. To choose a distance
1672 cutoff at which ROIs were considered in the same cluster (i.e., same dendritic segment), we
1673 generated a correlation matrix using a shuffled distribution for each animal. The time course of
1674 calcium activity from each ROI from each mouse was circularly shuffled by a random amount.

1675 This procedure essentially ensures uncorrelated activity in all ROIs and the cutoff value that
1676 yielded at least one inaccurate cluster in less than 5 percent of the trails (500 trails) was used as
1677 the cutoff for that animal (mean cutoff value = 0.13 ± 0.01). To ensure that clustering criteria were
1678 not lenient, we also used singular cutoff values - 0.15 or 0.3 – to cluster less correlated ROIs.
1679 These criteria when used for all animals resulted in similar results ($p < 0.001$). The clustering
1680 method yielded ROI clusters with highly correlated within-cluster activity across sessions
1681 (reference and comparison sessions for reactivated ROIs; Figure S12c).

1682 Analysis of correlated dendritic activity: Dendritic activity/events were estimated via non-
1683 negative temporal deconvolution of the Suite-2p extracted signal using Vanilla algorithm [106,109].
1684 Event probabilities were then binarized to reflect active frames and number of active frames were
1685 used to calculate an event rate. To account for variations in the number of reactivated ROIs in
1686 imaging sessions 5 hours and 7 days apart, we randomly subsampled 30 reactivated ROI pairs
1687 for each comparison (500x) to generate a probability distribution (compared using a ks test).

1688 **Slice Preparation**

1689 Adult cFos-tTa mice were injected with 500 nl of AAV1-TRE-hChR2-mCherry or AAV1-
1690 TRE-hChR2-mCherry-DTE. After three or more weeks, mice were taken off doxycycline for three
1691 days, allowed to explore a novel context for 10 min and 24 hours later were deeply anaesthetized
1692 with isoflurane and decapitated. The brain was rapidly dissected out and transferred to
1693 oxygenated (95% O_2 / 5% CO_2), ice-cold cutting solution containing (in mM): 92 choline, 2.5 KCl,
1694 1.2 NaH_2PO_4, 30 $NaHCO_3$, 20 HEPES, 25 glucose, 2 Thiourea, 5 Na-ascorbate, 3 Na-pyruvate,
1695 5 N-acetyl-L-cysteine, 0.5 $CaCl_2$ and 10 $MgSO_4$. Coronal slices (300 µm thick) containing the
1696 retrosplenial cortex were cut using a Leica VT1200 vibrating blade microtome, transferred to a
1697 submerged holding chamber containing oxygenated cutting solution and allowed to recover for
1698 15 min at 34˚C. Following recovery, the slices were transferred to an oxygenated solution
1699 containing (in mM): 92 HEPES, 2.5 KCl, 1.2 NaH_2PO_4, 30 $NaHCO_3$, 20 HEPES, 25 glucose, 2
1700 Thiourea, 5 Na-ascorbate, 3 Na-pyruvate, 5 N-acetyl-L-cysteine, 2 $CaCl_2$ and 2 $MgCl_2$ and allowed

1701 to recover further for 1hr. Following incubation, slices were transferred to a superfused recording
1702 chamber and constantly perfused with oxygenated aCSF containing (in mM): 115 NaCl, 10
1703 glucose, 25.5 $NaHCO_3$, 1.05 NaH_2PO_4, 3.3 KCl, 2 $CaCl_2$ and 1 $MgCl_2$ and maintained at 28°C.
1704 For two mice (TTA-ChR2 and TTA-ChR2-DTE, n = 1 each), brains were sliced in recording
1705 solution.

1706 **Whole-cell patch recordings**

1707 Whole cell current-clamp recordings were performed on pyramidal neurons in the RSC
1708 using pipettes (3-5MΩ resistance) pulled from thin-walled Borosilicate glass using a Sutter P97
1709 Flaming/Brown micropipette puller and filled with an internal solution containing (in mM) 110 K-
1710 Gluconate, 20 KCl, 2 $MgCl_2$, 10 HEPES, 10 Na_2-ATP and 0.3 Na_2-GTP and 10 Na-
1711 phosphocreatine. All recordings were obtained using a MultiClamp 700B amplifier controlled by
1712 the pClamp 10 software and digitized using the Digidata 1440A system. Signals were filtered at
1713 10kHz and digitized at 20kHz. Neurons were included in the study only if the initial resting
1714 membrane potential (Vm) $\leq$ -55 mV, access resistance (Ra) was <25MΩ and were rejected if the
1715 Ra changed by >20% of its initial value. For all recordings, neurons were held at -60 mV. The
1716 stable resting membrane potential of neurons were measured and averaged over a 60s duration
1717 with 0mA current injection immediately after breaking in. Input resistance was measured as the
1718 slope of the steady-state voltage response to increasing current injections (-50pA to 50pA,
1719 Δ=10pA). To investigate the response of the neurons following optogenetic stimulation, 473nm
1720 LED (5 ms pulses, 5 Hz) was delivered through Cool LED pE-300 and neuronal response was
1721 calculated. Only neurons with a visible response to optogenetic stimulation were included in
1722 analysis (n = 12 from > 50 RSC neurons). All mCherry-positive RSC neurons from TTA-ChR2
1723 mice resulted in APs following stimulation. The recordings were analyzed using Clampfit and
1724 Matlab.

1725 **Computational modeling.** We adapted a previously published model network of memory
1726 allocation [51]. The model network consists of populations of excitatory and inhibitory neurons,

which are modeled as 2-level integrators to account for dendrites. Increases in dendritic and somatic excitability are assumed to follow the time course of CREB activation. CREB activation, in turn, is assumed to be triggered when calcium accumulation exceeds a threshold.

Neurons consist of a somatic spiking unit connected to multiple independent dendritic subunits. Dendrites and soma are modeled using simplified integrate-and-fire model dynamics, where the somatic unit includes adaptation current, and dendrites and soma are coupled to it via axial resistance. Inhibitory neurons provide feedback inhibition and are separated into 2 equal sub-populations, soma-targeting and dendrite-targeting. The voltage of each dendritic subunit is as follows:

$$C\frac{dV_d}{dt} = -g_L(V_d - E_L) + a_{exc}g_E u_E(t)(E_E - V_d) - g_I u_I(t)(E_I - V_d) \qquad (1)$$

where V_d is the dendritic membrane potential, C is the membrane capacitance, E_E is the reversal potential for excitatory receptors, E_I is the reversal potential for inhibitory receptors, E_L is the resting potential (0mV), a_{exc} is the dendritic excitability level parameter, g_L is the leak conductance, g_E, g_I are the maximal excitatory and inhibitory synaptic conductances. $u_I(t)$ *and* $u_E(t)$ are the instantaneous activations of excitatory and inhibitory synapses on the dendrite respectively:

$$u_{E/I}(t) = \sum_j w_j\, \delta\big(t - t_j\big) \qquad (2)$$

where w_j is the weight of synapse j and t_j are the timings of incoming spikes.

Somatic voltage is modeled as an Integrate-and-Fire model with adaptation as follows:

$$C\frac{dV}{dt} = -g_L(V - E_L) + I_{noise}(t) + I_{ax}(t) - I_{inh}(t) - I_{adapt}(t) \qquad (3)$$

$$\tau_{adapt}\frac{dI_{adapt}}{dt} = \alpha_{adapt}(V - E_L) + \beta_{adapt}\delta\,(t - t_{spike}) - I_{adapt} \qquad (4)$$

$$I_{ax} = \sum_i g_{ax}\,(V_{d,i} - V)_+ \qquad (5)$$

$$\tau_{inh}\frac{dI_{inh}}{dt} = \sum_i g_{inh}\delta(t - t_i) - I_{inh} \qquad (6)$$

where V is the somatic voltage, I_{noise} is uniform noise current (max amplitude 500 pA), I_{ax} is the excitatory axial current, I_{inh} is the filtered inhibitory current from somatically-targeting interneurons,

1751 I_{adapt} is the adaptation current, τ_{adapt} is the adaptation time constant, α_{adapt} the adaptation coupling
1752 parameter, β_{adapt} is the amount by which adaptation current increases every time the neuron
1753 spikes, g_{ax} is the axial resistance, τ_{inh} is the time constant of inhibitory current and g_{inh} the inhibitory
1754 current scaling constant. Somatic spiking occurs when the somatic voltage reaches the spike
1755 threshold θ_{soma}. On an incoming spike, synaptic and dendritic branch calcium is increased by an
1756 amount $\Delta Ca(V_d)$ that depends on the instantaneous depolarization V_d of the dendritic branch to
1757 account for the Magnesium blocking of NMDA receptor:

1758 $$\Delta Ca(V_d) = \frac{1}{1+\frac{e^{-0.07(V_d - 70)}}{9}} \quad (7)$$

1759 Synaptic inputs representing memories to be encoded are initially allocated randomly to the
1760 dendritic subunits of excitatory neurons with initial weight ranging uniformly randomly between
1761 0.16 and 0.36. In addition, feedback synapses between excitatory and inhibitory populations are
1762 allocated at random, with separate distributions for soma-targeting and dendrite-targeting
1763 interneurons (see Supplementary Table 2). In the case of dendritic separation between memories
1764 (Figure 7g) the memories were allocated at random dendrites but were not allowed to overlap in
1765 the same dendrite.
1766 The total calcium influx during memory encoding determines synaptic plasticity, changes in
1767 excitability and the levels of plasticity-related proteins (PRPs) after encoding. In order to replicate
1768 the experimental observation that the number of new synapses correlates positively with the
1769 existing potentiated synapses within the same dendrite, we introduce stochasticity in synaptic
1770 tagging as described below. Synapses that receive calcium influx above zero during stimulation
1771 are selected for potentiation or depression. If the synapse resides on a neuron that is highly
1772 activated (spiking with frequency > 10 Hz during stimulus presentation) then the synapse is
1773 tagged for potentiation with probability $p_{LTP} = 0.29 + X_{dend} * N_s/2$, otherwise the synapse is tagged
1774 for depression. N_s is the number of preexisting potentiated synapses in the same dendrite and
1775 X_{dend} is the excitability of the dendrite (see below). Synaptic tags decay exponentially with time

constant of 1 hour.

When the somatic calcium level of a neuron exceeds Θ_{PRP} at time T, the level of plasticity-related proteins of the neuron is elevated according to the following function:

$$PRP(T) = \begin{cases} \frac{T-20}{30}\, e^{-\frac{T+10}{30}}, & T > 20 \\ 0, & T \leq 20 \end{cases} \qquad (8)$$

where T is the time since the stimulus in minutes. When synaptic tags and PRPs have values above 0.1, the weights w of synapses are updated by $\Delta w = 0.15*PRP(t)*(synaptic\ tag)$, where t is time in seconds. Synaptic weights are bounded in the interval [0, 1]. We note that, because the delay between memories in all simulations is 5 hours or more, the PRP protein levels are always sufficient for full synaptic tag consolidation, and thus there was no competition for PRPs that could affect the linking of memories.

Excitability within the Linking model: Dendritic and somatic excitability are assumed to be mediated via the dynamics of CREB activation after learning. The increased excitability after learning is triggered when calcium accumulation exceeds a threshold. The time course of increased excitability is modeled as a sum of two sigmoids and exceeds 24 hours [110] as shown below

When the total dendritic and somatic calcium are above thresholds Θ_{dend} and Θ_{soma} respectively, the excitability level X of the dendrite/soma is increased by the amount given by:

$$X_{dend,soma}(T) = \frac{1}{1+e^{-3(T-1)}} - \frac{1}{1+e^{-(T-26)}} \qquad (9)$$

where T is the time in hours since the stimulus. The excitability level parameter a_{exc} is increased by 10% when $X_{dend} > 0.1$, while the adaptation reset parameter β_{adapt} is increased by 28% when $X_{soma} > 0.1$. For the simulations of the Linking model without dendritic mechanisms, the dendritic excitability was set at $X_{dend} = 0$ and the probability p_{LTP} was kept constant at 0.32.

Synaptic weights are additionally subject to a homeostatic synaptic scaling rule, which adjusts synaptic weights w_j to normalize the total synaptic input to each neuron with time constant τ_H:

$$\frac{dw_j}{dt} = \frac{1}{\tau_H}\left(1 - \frac{\sum_j w_j}{w_{init}\, N_{syn}}\right) \quad (10)$$

where w_{init} is 0.3 and N_{syn} is the total number of incoming synapses to the neuron.

Stimulation protocol: For every memory being encoded, the synaptic inputs which represent the memory are stimulated for 4 seconds with firing rate 35Hz in order to drive the initially weak synapses. After the first memory encoding, a delay period is simulated for 5 hours, 2 days or 7 days, and then the second memory is encoded. Memories are recalled by being stimulated again after 2 days.

For the clustering statistics, a branch was considered to contain overlapping clusters if it contained at least 3 potentiated synapses from each memory. The parameters used in the model are listed in Supplementary Table 2. The model was written in C++ and data analysis was done with Python/numpy. The source code for the simulation, data analysis and scripts to reproduce the data and figures are available at https://dendrites.gr/wp-content/uploads/2022/08/rsc_model2.zip. Chance levels for neuronal overlap was calculated as previously described [12]: Chance Overlap = [(Neuronal ensemble encoding A x Neuronal ensemble encoding B)/100]. Percent above chance overlap = (Observed Overlap – Chance Overlap)/Chance Overlap.

Quantification and Statistical Analyses. The investigator who collected and analyzed the data including behavior, imaging and staining was blinded to the mouse genotypes and treatment conditions. Error bars in the figures indicate the SEM. All statistical analyses were performed using GraphPad Prism 9 or Matlab. For behavior and imaging experiments, n designates the number of mice unless otherwise mentioned. Statistical significance for behavioral manipulations was assessed using parametric tests (Student's t test, or one- or two-way ANOVA) followed by the indicated post-hoc tests (GraphPad Prism 9 recommended post-hoc tests) as data followed a Gaussian distribution. The level of significance was set at $p < 0.05$ unless Bonferroni's correction for multiple comparisons was used.

1824 ***Acknowledgements.*** We thank P. Riazi, J. Lin, E. Rubin, G. Padda, Y. Cai, M. Zhou, D.
1825 J. Cai, D. Aharoni, C.E. Yaeger, A. F. de Sousa, A. Chowdhury and Y. Shen for advice and
1826 technical support. We thank Dean Buonomono, Mayank R. Mehta, Peyman Golshani and James
1827 M. Otis for helpful discussions. This work was supported by grants from the NIMH (R01
1828 MH113071), NIA (R01 AG013622), and from the Dr. Miriam and Sheldon G. Adelson Medical
1829 Research Foundation to AJS. The computational modeling work was supported by the European
1830 Commission (H2020-FETOPEN-2018-2019-2020-01, FET-Open Challenging Current Thinking,
1831 GA-863245), the NIH (R01MH124867-01) and the Einstein Foundation Berlin. We acknowledge
1832 resources from the Campus Microscopy and Imaging Facility (CMIF) and the OSU
1833 Comprehensive Cancer Center (OSUCCC) Microscopy Shared Resource (MSR), The Ohio State
1834 University (RRID:SCR_025078). This facility is supported in part by grant P30 CA016058,
1835 National Cancer Institute, Bethesda, MD.

1836 ***Author contribution.*** MS and AJS did experimental design, data acquisition and
1837 analyses, drafting and revising the article; JT helped with experimental design for two-photon
1838 calcium imaging experiments. SM, IDM, AP helped with behavioral data acquisition; SK, JL, WDH
1839 made the TRE-dependent constructs; DAF helped with Miniscope data analysis and
1840 interpretation; AL and SH helped with two-photon data analyses and interpretation; GK and PP
1841 designed, implemented, and analyzed the computational modeling experiments. All authors read
1842 and edited the manuscript.

1843 ***Competing interests.*** The authors declare no competing interests.

1844

1. Poirazi, P., Brannon, T. & Mel, B. W. Pyramidal Neuron as Two-Layer Neural Network. *Neuron* **37**, 989–999 (2003).
2. Poirazi, P. & Mel, B. W. Impact of active dendrites and structural plasticity on the memory capacity of neural tissue. *Neuron* **29**, 779–796 (2001).
3. Spruston, N. Pyramidal neurons: dendritic structure and synaptic integration. *Nat. Rev. Neurosci.* **9**, 206–221 (2008).
4. Frick, A., Magee, J. & Johnston, D. LTP is accompanied by an enhanced local excitability of pyramidal neuron dendrites. *Nat. Neurosci.* **7**, 126–135 (2004).
5. Govindarajan, A., Kelleher, R. J. & Tonegawa, S. A clustered plasticity model of long-term memory engrams. *Nat. Rev. Neurosci.* **7**, 575–583 (2006).
6. Govindarajan, A., Israely, I., Huang, S.-Y. & Tonegawa, S. The dendritic branch is the preferred integrative unit for protein synthesis-dependent LTP. *Neuron* **69**, 132–146 (2011).
7. Harvey, C. D., Yasuda, R., Zhong, H. & Svoboda, K. The Spread of Ras Activity Triggered by Activation of a Single Dendritic Spine. *Science* **321**, 136–140 (2008).
8. Losonczy, A., Makara, J. K. & Magee, J. C. Compartmentalized dendritic plasticity and input feature storage in neurons. *Nature* **452**, 436–441 (2008).
9. Rogerson, T. *et al.* Synaptic tagging during memory allocation. *Nat. Rev. Neurosci.* **15**, 157–169 (2014).
10. Sehgal, M. *et al.* Memory allocation mechanisms underlie memory linking across time. *Neurobiol. Learn. Mem.* **153**, 21–25 (2018).
11. de Sousa, A. F., Chowdhury, A. & Silva, A. J. Dimensions and mechanisms of memory organization. *Neuron* S0896-6273(21)00455–4 (2021) doi:10.1016/j.neuron.2021.06.014.

1867 12. Cai, D. J. *et al.* A shared neural ensemble links distinct contextual memories encoded close
1868 in time. *Nature* **534**, 115–118 (2016).
1869 13. Yokose, J. *et al.* Overlapping memory trace indispensable for linking, but not recalling,
1870 individual memories. *Science* **355**, 398–403 (2017).
1871 14. Rashid, A. J. *et al.* Competition between engrams influences fear memory formation and
1872 recall. *Science* **353**, 383–387 (2016).
1873 15. Schlichting, M. L. & Preston, A. R. Memory integration: neural mechanisms and
1874 implications for behavior. *Curr. Opin. Behav. Sci.* **1**, 1–8 (2015).
1875 16. Zeithamova, D., Dominick, A. L. & Preston, A. R. Hippocampal and ventral medial
1876 prefrontal activation during retrieval-mediated learning supports novel inference. *Neuron*
1877 **75**, 168–179 (2012).
1878 17. Ryan, T. J., Roy, D. S., Pignatelli, M., Arons, A. & Tonegawa, S. Engram Cells Retain
1879 Memory Under Retrograde Amnesia. *Science* **348**, 1007–1013 (2015).
1880 18. Hayashi-Takagi, A. *et al.* Labelling and optical erasure of synaptic memory traces in the
1881 motor cortex. *Nature* **525**, 333–338 (2015).
1882 19. Frank, A. C. *et al.* Hotspots of dendritic spine turnover facilitate clustered spine addition and
1883 learning and memory. *Nat. Commun.* **9**, 422 (2018).
1884 20. Lai, C. S. W., Adler, A. & Gan, W.-B. Fear extinction reverses dendritic spine formation
1885 induced by fear conditioning in the mouse auditory cortex. *Proc. Natl. Acad. Sci.* **115**,
1886 9306–9311 (2018).
1887 21. Rumpel, S., LeDoux, J., Zador, A. & Malinow, R. Postsynaptic Receptor Trafficking
1888 Underlying a Form of Associative Learning. *Science* **308**, 83–88 (2005).

1889 22. Sah, P. & Bekkers, J. M. Apical Dendritic Location of Slow Afterhyperpolarization Current
1890 in Hippocampal Pyramidal Neurons: Implications for the Integration of Long-Term
1891 Potentiation. *J. Neurosci.* **16**, 4537–4542 (1996).
1892 23. Harvey, C. D. & Svoboda, K. Locally dynamic synaptic learning rules in pyramidal neuron
1893 dendrites. *Nature* **450**, 1195–1200 (2007).
1894 24. Cowansage, K. K. *et al.* Direct reactivation of a coherent neocortical memory of context.
1895 *Neuron* **84**, 432–441 (2014).
1896 25. Miller, A. M. P., Serrichio, A. C. & Smith, D. M. Dual-Factor Representation of the
1897 Environmental Context in the Retrosplenial Cortex. *Cereb. Cortex* **31**, 2720–2728 (2021).
1898 26. DeNardo, L. A. *et al.* Temporal evolution of cortical ensembles promoting remote memory
1899 retrieval. *Nat. Neurosci.* **22**, 460–469 (2019).
1900 27. Driscoll, L. N., Pettit, N. L., Minderer, M., Chettih, S. N. & Harvey, C. D. Dynamic
1901 Reorganization of Neuronal Activity Patterns in Parietal Cortex. *Cell* **170**, 986-999.e16
1902 (2017).
1903 28. Kentros, C. G., Agnihotri, N. T., Streater, S., Hawkins, R. D. & Kandel, E. R. Increased
1904 attention to spatial context increases both place field stability and spatial memory. *Neuron*
1905 **42**, 283–295 (2004).
1906 29. Lee, J. S., Briguglio, J. J., Cohen, J. D., Romani, S. & Lee, A. K. The Statistical Structure of
1907 the Hippocampal Code for Space as a Function of Time, Context, and Value. *Cell* **183**, 620-
1908 635.e22 (2020).
1909 30. Mankin, E. A. *et al.* Neuronal code for extended time in the hippocampus. *Proc. Natl. Acad.*
1910 *Sci.* **109**, 19462–19467 (2012).

31. Rokni, U., Richardson, A. G., Bizzi, E. & Seung, H. S. Motor learning with unstable neural representations. *Neuron* **54**, 653–666 (2007).

32. Rubin, A., Geva, N., Sheintuch, L. & Ziv, Y. Hippocampal ensemble dynamics timestamp events in long-term memory. *eLife* **4**, e12247 (2015).

33. Schoonover, C. E., Ohashi, S. N., Axel, R. & Fink, A. J. P. Representational drift in primary olfactory cortex. *Nature* **594**, 541–546 (2021).

34. Buzsáki, G. Neural syntax: cell assemblies, synapsembles and readers. *Neuron* **68**, 362–385 (2010).

35. Harris, K. D., Csicsvari, J., Hirase, H., Dragoi, G. & Buzsáki, G. Organization of cell assemblies in the hippocampus. *Nature* **424**, 552–556 (2003).

36. Dejean, C. *et al.* Prefrontal neuronal assemblies temporally control fear behaviour. *Nature* **535**, 420–424 (2016).

37. Girardeau, G., Benchenane, K., Wiener, S. I., Buzsáki, G. & Zugaro, M. B. Selective suppression of hippocampal ripples impairs spatial memory. *Nat. Neurosci.* **12**, 1222–1223 (2009).

38. El-Gaby, M. *et al.* An emergent neural coactivity code for dynamic memory. *Nat. Neurosci.* **24**, 694–704 (2021).

39. Hebb, D. O. The organization of behavior: A neuropsychological theory. New York: John Wiley and Sons, Inc., 1949. 335 p. $4.00. *Sci. Educ.* **34**, 336–337 (1950).

40. Gava, G. P. *et al.* Integrating new memories into the hippocampal network activity space. *Nat. Neurosci.* **24**, 326–330 (2021).

41. Chang, H. *et al.* Coordinated activities of retrosplenial ensembles during resting-state encode spatial landmarks. *Philos. Trans. R. Soc. B Biol. Sci.* **375**, 20190228 (2020).

42. Reijmers, L. G., Perkins, B. L., Matsuo, N. & Mayford, M. Localization of a stable neural correlate of associative memory. *Science* **317**, 1230–1233 (2007).

43. Tanaka, K. Z. *et al.* The hippocampal engram maps experience but not place. *Science* **361**, 392–397 (2018).

44. Liu, X. *et al.* Optogenetic stimulation of a hippocampal engram activates fear memory recall. *Nature* **484**, 381–385 (2012).

45. Yamawaki, N. *et al.* Long-range inhibitory intersection of a retrosplenial thalamocortical circuit by apical tuft-targeting CA1 neurons. *Nat. Neurosci.* **22**, 618–626 (2019).

46. Yamawaki, N., Corcoran, K. A., Guedea, A. L., Shepherd, G. M. G. & Radulovic, J. Differential Contributions of Glutamatergic Hippocampal→Retrosplenial Cortical Projections to the Formation and Persistence of Context Memories. *Cereb. Cortex* **29**, 2728–2736 (2019).

47. Roy, D. S. *et al.* Anterior thalamic dysfunction underlies cognitive deficits in a subset of neuropsychiatric disease models. *Neuron* **109**, 2590-2603.e13 (2021).

48. Shen, Y. *et al.* CCR5 closes the temporal window for memory linking. *Nature* **606**, 146–152 (2022).

49. Yiu, A. P. *et al.* Neurons Are Recruited to a Memory Trace Based on Relative Neuronal Excitability Immediately before Training. *Neuron* **83**, 722–735 (2014).

50. Abdou, K. *et al.* Synapse-specific representation of the identity of overlapping memory engrams. *Science* **360**, 1227–1231 (2018).

51. Kastellakis, G., Silva, A. J. & Poirazi, P. Linking Memories across Time via Neuronal and Dendritic Overlaps in Model Neurons with Active Dendrites. *Cell Rep.* **17**, 1491–1504 (2016).

52. d'Aquin, S. *et al.* Compartmentalized dendritic plasticity during associative learning. *Science* **376**, eabf7052 (2022).

53. Francioni, V., Padamsey, Z. & Rochefort, N. L. High and asymmetric somato-dendritic coupling of V1 layer 5 neurons independent of visual stimulation and locomotion. *eLife* **8**, e49145 (2019).

54. O'Hare, J. K. *et al.* Compartment-specific tuning of dendritic feature selectivity by intracellular Ca2+ release. *Science* **375**, eabm1670 (2022).

55. Voigts, J. & Harnett, M. T. Somatic and Dendritic Encoding of Spatial Variables in Retrosplenial Cortex Differs during 2D Navigation. *Neuron* **105**, 237-245.e4 (2020).

56. Wilson, D. E., Whitney, D. E., Scholl, B. & Fitzpatrick, D. Orientation selectivity and the functional clustering of synaptic inputs in primary visual cortex. *Nat. Neurosci.* **19**, 1003–1009 (2016).

57. Lavzin, M., Rapoport, S., Polsky, A., Garion, L. & Schiller, J. Nonlinear dendritic processing determines angular tuning of barrel cortex neurons in vivo. *Nature* **490**, 397–401 (2012).

58. Palmer, L. M. *et al.* NMDA spikes enhance action potential generation during sensory input. *Nat. Neurosci.* **17**, 383–390 (2014).

59. Smith, S. L., Smith, I. T., Branco, T. & Häusser, M. Dendritic spikes enhance stimulus selectivity in cortical neurons in vivo. *Nature* **503**, 115–120 (2013).

60. Ujfalussy, B. B. & Makara, J. K. Impact of functional synapse clusters on neuronal response selectivity. *Nat. Commun.* **11**, 1413 (2020).

61. Scholl, B., Wilson, D. E. & Fitzpatrick, D. Local Order within Global Disorder: Synaptic Architecture of Visual Space. *Neuron* **96**, 1127-1138.e4 (2017).

1979 62. Scholl, B., Thomas, C. I., Ryan, M. A., Kamasawa, N. & Fitzpatrick, D. Cortical response
1980 selectivity derives from strength in numbers of synapses. *Nature* **590**, 111–114 (2021).
1981 63. Andreassi, C. & Riccio, A. To localize or not to localize: mRNA fate is in 3′UTR ends.
1982 *Trends Cell Biol.* **19**, 465–474 (2009).
1983 64. Wang, D. O., Martin, K. C. & Zukin, R. S. Spatially restricting gene expression by local
1984 translation at synapses. *Trends Neurosci.* **33**, 173–182 (2010).
1985 65. Gobbo, F. *et al.* Activity-dependent expression of Channelrhodopsin at neuronal synapses.
1986 *Nat. Commun.* **8**, 1629 (2017).
1987 66. Moda-Sava, R. N. *et al.* Sustained rescue of prefrontal circuit dysfunction by antidepressant-
1988 induced spine formation. *Science* **364**, eaat8078 (2019).
1989 67. Lyford, G. L. *et al.* Arc, a Growth Factor and Activity-Regulated Gene, Encodes a Novel C
1990 oskeleton-Associated Protein That Is Enriched in Neuronal Dendrites.
1991 68. Steward, O. & Worley, P. F. Selective Targeting of Newly Synthesized Arc mRNA to Active
1992 Synapses Requires NMDA Receptor Activation. *Neuron* **30**, 227–240 (2001).
1993 69. Steward, O., Wallace, C. S., Lyford, G. L. & Worley, P. F. Synaptic Activation Causes the
1994 mRNA for the IEG *Arc* to Localize Selectively near Activated Postsynaptic Sites on
1995 Dendrites. *Neuron* **21**, 741–751 (1998).
1996 70. Link, W. *et al.* Somatodendritic expression of an immediate early gene is regulated by
1997 synaptic activity. *Proc. Natl. Acad. Sci. U. S. A.* **92**, 5734–5738 (1995).
1998 71. Chen, L. Y., Rex, C. S., Casale, M. S., Gall, C. M. & Lynch, G. Changes in Synaptic
1999 Morphology Accompany Actin Signaling during LTP. *J. Neurosci.* **27**, 5363–5372 (2007).
2000 72. Bosch, M. *et al.* Structural and Molecular Remodeling of Dendritic Spine Substructures
2001 during Long-Term Potentiation. *Neuron* **82**, 444–459 (2014).

2002 73. Sehgal, M., Ehlers, V. L. & Moyer, J. R. Learning enhances intrinsic excitability in a subset
2003 of lateral amygdala neurons. *Learn. Mem.* **21**, 161–170 (2014).
2004 74. Minoshima, S. *et al.* Metabolic reduction in the posterior cingulate cortex in very early
2005 Alzheimer's disease. *Ann. Neurol.* **42**, 85–94 (1997).
2006 75. Pengas, G., Hodges, J. R., Watson, P. & Nestor, P. J. Focal posterior cingulate atrophy in
2007 incipient Alzheimer's disease. *Neurobiol. Aging* **31**, 25–33 (2010).
2008 76. Trask, S., Pullins, S. E., Ferrara, N. C. & Helmstetter, F. J. The anterior retrosplenial cortex
2009 encodes event-related information and the posterior retrosplenial cortex encodes context-
2010 related information during memory formation. *Neuropsychopharmacology* **46**, 1386–1392
2011 (2021).
2012 77. Vedder, L. C., Miller, A. M. P., Harrison, M. B. & Smith, D. M. Retrosplenial Cortical
2013 Neurons Encode Navigational Cues, Trajectories and Reward Locations During Goal
2014 Directed Navigation. *Cereb. Cortex* **27**, 3713–3723 (2017).
2015 78. Corcoran, K. A. *et al.* NMDA Receptors in Retrosplenial Cortex Are Necessary for Retrieval
2016 of Recent and Remote Context Fear Memory. *J. Neurosci.* **31**, 11655–11659 (2011).
2017 79. Dorst, K. E. *et al.* Hippocampal Engrams Generate Variable Behavioral Responses and
2018 Brain-Wide Network States. *J. Neurosci.* **44**, (2024).
2019 80. Czajkowski, R. *et al.* Encoding and storage of spatial information in the retrosplenial cortex.
2020 *Proc. Natl. Acad. Sci.* **111**, 8661–8666 (2014).
2021 81. Eichenbaum, H. The role of the hippocampus in navigation is memory. *J. Neurophysiol.* **117**,
2022 1785–1796 (2017).
2023 82. Mao, D. *et al.* Hippocampus-dependent emergence of spatial sequence coding in
2024 retrosplenial cortex. *Proc. Natl. Acad. Sci.* **115**, 8015–8018 (2018).

2025 83. Kim, J. J. & Fanselow, M. S. Modality-Specific Retrograde Amnesia of Fear. *Science* **256**,
2026 675–677 (1992).
2027 84. Vann, S. D., Aggleton, J. P. & Maguire, E. A. What does the retrosplenial cortex do? *Nat.*
2028 *Rev. Neurosci.* **10**, 792–802 (2009).
2029 85. Fournier, D. I., Monasch, R. R., Bucci, D. J. & Todd, T. P. Retrosplenial Cortex Damage
2030 Impairs Unimodal Sensory Preconditioning. *Behav. Neurosci.* **134**, 198–207 (2020).
2031 86. Kwapis, J. L., Jarome, T. J., Lee, J. L. & Helmstetter, F. J. The retrosplenial cortex is
2032 involved in the formation of memory for context and trace fear conditioning. *Neurobiol.*
2033 *Learn. Mem.* **123**, 110–116 (2015).
2034 87. Robinson, S., Adelman, J. S., Mogul, A. S., Ihle, P. C. J. & Davino, G. M. Putting fear in
2035 context: Elucidating the role of the retrosplenial cortex in context discrimination in rats.
2036 *Neurobiol. Learn. Mem.* **148**, 50–59 (2018).
2037 88. de Sousa, A. F. *et al.* Optogenetic reactivation of memory ensembles in the retrosplenial
2038 cortex induces systems consolidation. *Proc. Natl. Acad. Sci.* **116**, 8576–8581 (2019).
2039 89. Makino, H. & Malinow, R. Compartmentalized versus Global Synaptic Plasticity on
2040 Dendrites Controlled by Experience. *Neuron* **72**, 1001–1011 (2011).
2041 90. Schuman, E. M. Synapse Specificity and Long-Term Information Storage. *Neuron* **18**, 339–
2042 342 (1997).
2043 91. Yang, G. *et al.* Sleep promotes branch-specific formation of dendritic spines after learning.
2044 *Science* **344**, 1173–1178 (2014).
2045 92. Xu, Z., Geron, E., Pérez-Cuesta, L. M., Bai, Y. & Gan, W.-B. Generalized extinction of fear
2046 memory depends on co-allocation of synaptic plasticity in dendrites. *Nat. Commun.* **14**, 503
2047 (2023).

2048 93. Lafourcade, M. *et al.* Differential dendritic integration of long-range inputs in association
2049 cortex via subcellular changes in synaptic AMPA-to-NMDA receptor ratio. *Neuron* **110**,
2050 1532-1546.e4 (2022).
2051 94. Aly, M. H., Abdou, K., Okubo-Suzuki, R., Nomoto, M. & Inokuchi, K. Selective engram
2052 coreactivation in idling brain inspires implicit learning. *Proc. Natl. Acad. Sci.* **119**,
2053 e2201578119 (2022).
2054 95. Chowdhury, A. & Caroni, P. Time units for learning involving maintenance of system-wide
2055 cFos expression in neuronal assemblies. *Nat. Commun.* **9**, 4122 (2018).
2056 96. Chowdhury, A. *et al.* A locus coeruleus-dorsal CA1 dopaminergic circuit modulates memory
2057 linking. *Neuron* **110**, 3374-3388.e8 (2022).
2058 97. Petreanu, L., Mao, T., Sternson, S. M. & Svoboda, K. The subcellular organization of
2059 neocortical excitatory connections. *Nature* **457**, 1142–1145 (2009).
2060 98. Kasai, H., Ziv, N. E., Okazaki, H., Yagishita, S. & Toyoizumi, T. Spine dynamics in the
2061 brain, mental disorders and artificial neural networks. *Nat. Rev. Neurosci.* **22**, 407–422
2062 (2021).
2063 99. Forrest, M. P., Parnell, E. & Penzes, P. Dendritic structural plasticity and neuropsychiatric
2064 disease. *Nat. Rev. Neurosci.* **19**, 215–234 (2018).
2065 100. Kim, S. *et al.* Dynamic Fas signaling network regulates neural stem cell proliferation and
2066 memory enhancement. *Sci. Adv.* **6**, eaaz9691.
2067 101. Pnevmatikakis, E. A. & Giovannucci, A. NoRMCorre: An online algorithm for piecewise
2068 rigid motion correction of calcium imaging data. *J. Neurosci. Methods* **291**, 83–94 (2017).
2069 102. Zhou, P. *et al.* Efficient and accurate extraction of in vivo calcium signals from
2070 microendoscopic video data. *eLife* **7**, e28728 (2018).

2071 103. Etter, G. MiniscopeAnalysis. (2021).
2072 104. Choi, J.-H. *et al.* Interregional synaptic maps among engram cells underlie memory
2073 formation. *Science* **360**, 430–435 (2018).
2074 105. Lucchetti, J. *et al.* Plasma and brain concentrations of doxycycline after single and repeated
2075 doses in wild-type and APP23 mice. *J. Pharmacol. Exp. Ther.* jpet.118.252064 (2018)
2076 doi:10.1124/jpet.118.252064.
2077 106. Yaeger, C. E., Ringach, D. L. & Trachtenberg, J. T. Neuromodulatory control of localized
2078 dendritic spiking in critical period cortex. *Nature* **567**, 100–104 (2019).
2079 107. Pachitariu, M. *et al. Suite2p: Beyond 10,000 Neurons with Standard Two-Photon*
2080 *Microscopy*. 061507 https://www.biorxiv.org/content/10.1101/061507v1 (2016)
2081 doi:10.1101/061507.
2082 108. Liang, L. *et al.* A Fine-Scale Functional Logic to Convergence from Retina to Thalamus.
2083 *Cell* **173**, 1343-1355.e24 (2018).
2084 109. Berens, P. *et al.* Community-based benchmarking improves spike rate inference from two-
2085 photon calcium imaging data. *PLOS Comput. Biol.* **14**, e1006157 (2018).
2086 110. Schulz, S., Siemer, H., Krug, M. & Höllt, V. Direct Evidence for Biphasic cAMP
2087 Responsive Element-Binding Protein Phosphorylation during Long-Term Potentiation in
2088 the Rat Dentate Gyrus In Vivo. *J. Neurosci.* **19**, 5683–5692 (1999).
2089